COMPUTATION OF THE SCATTERING PROPERTIES OF NONSPHERICAL ICE CRYSTALS

A Thesis

by

ZHIBO ZHANG

Submitted to the Office of Graduate Studies of
Texas A&M University
in partial fulfillment of the requirements for the degree of

MASTER OF SCIENCE

August 2004

Major Subject: Atmospheric Sciences

COMPUTATION OF THE SCATTERING PROPERTIES OF NONSPHERICAL ICE CRYSTALS

A Thesis

by

ZHIBO ZHANG

Submitted to the Office of Graduate Studies of
Texas A&M University
in partial fulfillment of the requirements for the degree of

MASTER OF SCIENCE

Approved as to the style and content by:

Ping Yang (Chair of Committee)	George W. Kattawar (Member)
Thomas Wilheit (Member)	Richard Orville (Head of Department)

August 2004

Major Subject: Atmospheric Sciences

ABSTRACT

Computation of the Scattering Properties of Nonspherical Ice Crystals. (August 2004)

Zhibo Zhang, B.S., Nanjing University (China)

Chair of Advisory Committee: Dr. Ping Yang

This thesis is made up of three parts on the computation of scattering properties of nonspherical particles in the atmosphere. In the first part, a new crystal type—droxtal—is introduced to make a better representation of the shape of small ice crystals in the uppermost portions of midlatitude and tropical cirrus clouds. Scattering properties of droxtal ice crystals are investigated by using the Improved-Geometric Optic (IGO) method. At the visible wavelength, due to the presence of the hexagonal structure, all elements of the phase matrix of droxtal ice crystals share some common features with hexagonal ice crystals, such as 220 and 460 halos. In the second part of this thesis, the possibility of enhancing the performance of current Anomalous Diffraction Theory (ADT) is investigated. In conventional ADT models, integrations are usually carried out in the domain of the particle projection. By transforming the integration domain to the domain of scaled projectile length, the algorithm of conventional ADT models is enhanced. Because the distribution of scaled projectile length is independent of the particle's physical size as long as the shape remains the same, the new algorithm is especially efficient for the calculation of a large number of particles with the same shape but different sizes. Finally, in the third part, the backscattering properties of nonspherical ice crystals at the 94GHz frequency are studied by employing the Finite-Difference Time-Domain (FDTD) method. The most important factor that controls the backscattering cross section is found to be the ratio of the volume-equal radius to the maximum dimension of the ice crystal. Substantial differences in backscattering cross sections are found between horizontal orientated and randomly oriented ice crystals. An analytical formula is derived for the relationship between the ice water (IWC) content and the radar reflectivity (Z_e). It is shown that a change to the concentration of ice crystals without any changes on the size distribution or particle habits leads only to a linear $IWC - Z_e$ relationship. The famous power law $IWC - Z_e$ relationship is the result of the shift of the peak of particle size distribution.

ACKNOWLEDGEMENTS

I would like to thank my advisor, Dr. Ping Yang, for his guidance, instruction, patience, and support throughout my thesis project. Also, I would like to thank the members of my advisory committee, Dr. Thomas Wilheit and Dr. George Kattawar.

I would like to thank Dr. Guang Guo, Mr. Heli Wei, Mr. Yong-Keun Lee, Mr. Kerry Meyer and Mr. Guang Chen for their help with my research and studies.

This study was supported by a research grant (NAG-1-02002) from the NASA Radiation Science Program managed by Dr. Hal Maring (previously by Dr. Donald Anderson), and also by a National Science Foundation (NSF) CAREER Award grant (ATM-0239605) from the NSF Physical Meteorology Program managed by Dr. William A. Cooper.

Last but not least, I would like to thank my mother and father, Xiufen Zhang and Fengjun Zhang, and my girl friend, Caihong Wen, for believing in me and supporting me. To Kent Marshall, thanks for your enormous help with my spoken English and my life.

TABLE OF CONTENTS

Page

CHAPTER Page

LIST OF FIGURES

FIGURE Page

LIST OF TABLES

CHAPTER I
INTRODUCTION

Electromagnetic scattering by particles is a field of active research with high relevance for a great variety of the science and engineering disciplines, such as physics, electrical engineering_astronomy as well as atmospheric science. Various fascinating atmospheric displays such as rainbows, coronae, glories and halos are caused by the scattering of sunlight by cloud particles. By scattering and absorbing the incident solar radiation and the radiation emitted by the earth surface, clouds, aerosols and gas molecules in the atmosphere effectively modulate the climate of our planet. The strong dependence of scattering properties on particle size, shape and composition makes remote sensing measurements an indispensable information source of the characterization of atmospheric particles. Therefore, electromagnetic scattering problems are fundamentally important to the atmospheric optics, atmospheric radiative transfer, satellite, lidar and radar remote sensing and climate modeling.

If the object is a homogeneous spherical particle composed of isotropic materials, the scattering problem can be well served by the conventional Lorenz-Mie theory. However, a large amount of aerosols and ice crystals in the atmosphere are either nonspherical or inhomogeneous.[1,2] As a result, theories and computational models that account for effects of nonsphericity and inhomogeneity on electromagnetic scattering must be adopted. Theoretical work of the electromagnetic scattering by nonspherical particles can be found in classical monographs by van de Hulst[3], Kerker[4] and Bohren and Huffman[5]. As recently reviewed by Mishchenko et al.[6] and Kahnert[7], the advance in the computational power over the passed few decades has led to the boom of numerical models and techniques for the computation of scattering properties of nonspherical particles. Most of these scattering models have found their way into the atmospheric science. The Geometric-Optics Method (GOM) and the Finite-Difference Time-Domain (FDTD) method are heavily used in the computation of single scattering properties of nonspherical ice crystals, which are needed by studies related to the radiative transfer modeling, parameterization of cloud radiative properties and climate modeling[8-11]. Other methods, such as the Discrete Dipole Approximation

---

The journal selected as a model for style and format is Applied Optics.

(DDA) method,[12] the Anomalous Aiffraction Theory[13,14] (ADT), and the T-matrix method,[15,16] are also frequently employed. With the development of high frequency radar, rigorous scattering models such as FDTD and DDA have been introduced to the realm of radar remote sensing, which had been dominated by the Lorenz-Mie and Rayleigh scattering theory for a long time, to account for the backscattering of radar wave by large nonspherical ice crystals in clouds and precipitations.[17-19] The increasing enthusiasm for the climatic impact of atmospheric aerosols, which are usually small, nonspherical and highly inhomogeneous, has given rise to wide applications of the GOM, FDTD and T-matrix for aerosol and climate modeling research.[20-22]

Theoretically, we are now at the stage that the applicability range of current scattering models can cover all sizes and shapes of nonspherical aerosols and ice crystals that commonly occur in the atmosphere.[23] However, in reality, the electromagnetic scattering problem is far from settled. This is primarily because the limitations of the current scattering models. Based on *in situ* observations,[2, 24] the size of nonspherical ice crystals and atmospheric aerosols covers a range of several microns to several millimeters. Their shapes can be extremely complicated and they are usually randomly orientated in the space. Consequently, calculations of scattering properties of these particles for practical applications require that the scattering model to be efficient in terms of CPU time and elastic in terms of applicability. None of current models seem adequate to this dual requirement. Some rigorous scattering models such as the FDTD method and the Finite Element Method (FEM) can be easily applied to inhomogeneous, anisotropic and arbitrarily shaped particles, but they suffer greatly by being computationally intensive.[25,26] The other disadvantage is that the computations need to be repeated for each orientation of the particle, which further aggravates the burden of computations and makes these methods only applicable to particles with small size parameters. The DDA method shares many of the advantages with the FDTD and FEM methods as well as their limitations in terms of the computational complexity, size parameter range and the need to repeat all computations with changing orientation. Moreover, the numerical accuracy of DDA is relatively low, especially for the scattering matrix, and improves only slowly with increasing numbers of dipoles.[24,27] The T-matrix method surpasses aforementioned methods in terms of efficiency and size parameter range and is the only method that can be used to theoretically average particle scattering properties over random orientations.[28,29] However, the current T-matrix method is restricted to homogenous, rotationally symmetric

particles, such as spheres, spheroids, circular cylinders and Chebyshev particles.[29] This limitation makes the T-matrix serve as the benchmark to validate other models more often than a practically used model, especially when particles with complicated shapes are involved in the computation. Scattering models based on approximate theories such as GOM and ADT are designed for particles with sizes much larger than the incident wavelength, but their accuracy is low in comparison with exact methods.[10,30] Besides, due to the great sensitivity to the particle shape and refractive index, the GOM and ADT methods do not lend themselves easily to the modeling of inhomogeneous particles and particles with complicated shape. In fact, current GOM and ADT models are only available to a handful of shapes, although some progresses to extend these models to more complicated geometries have been made. As a result of the incapability of current scattering models facing the calculation demand alone, the combination of more than one scattering models are usually used in the real practice. For example, in order to obtain the database of single scattering properties of ice crystals over the whole size spectra, the FDTD and the GOM are respectively used for calculations of particles with small and large size parameters. Unfortunately, duo to the inherent difference in the theoretical base, the combination usually leads to the discontinuity of the scattering properties in the overlap region and interpolations must be applied artificially to obtain the continuity.[31]

Our limited knowledge of the physical properties of aerosols and ice crystals has also contributed the difficulty. Research efforts related to the composition, shape and refractive index of the atmospheric aerosols are still on the initial stage. No geometry models are available yet to represent the shapes of atmospheric aerosols in terms of the morphology, although a couple of the attempts have been made.[20] As a result, constructing geometry models for atmospheric aerosols that can be used in numerical scattering models is still a great challenge. Thanks to the simple composition as well as a great amount of previous research efforts, our current knowledge of cloud ice crystals is much better than that of atmospheric aerosols. The relationship between the shape and type of natural cloud ice crystals and the temperature at which they have grown has been established in several classical papers.[1,2,23] Unfortunately, most of the crystal types proposed in these paper are too complicated to be described by simple mathematical functions, which makes the diameter-thickness relationship only available for few crystal types such as the hexagonal plates, hexagonal columns, bullet rosettes, hollow columns and aggregates. Consequently, the types of ice crystals in almost all research works are restricted to these few geometry models, until the

recent introduction of several new crystals types to obtain more realistic cloud structure.[32,33] The other limitation of ice crystal models in current research is the lack of the inhomogeneous nature that results from the heterogeneous nucleation process. Although it has considerable impact on the scattering properties of ice crystals, it is still difficulty to be considered in practical scattering models because of the lack of quantitative data.

Ambitions to overcome difficulties in the computation of scattering properties of nonspherical ice crystals and aerosols have led current research efforts along two paths. The first is aimed at developing new scattering models by adopting up-to-date theories and numerical techniques, as well as enhancing the performance of existing models and extending their applicability range. For example, some hybrid models such as the Ray-By-Ray Integration (RBRI) model, a hybrid of the GOM and Volume Integration Models (VIM), have been or are being developed.[34] The FDTD code with 4th order truncation errors are being tested and will be used in the practice in the near feature (personal communication with Pengwang Zhai). More and more missing physical processes in the approximate methods such as the ADT and GOM are struggling their way back into the models.[35,36] On the other hand, researchers are trying to reveal the physical properties of nonspherical particles in the atmosphere, which in turn will make it clear whether a nonspherical scattering model is necessary and which one is suitable.

This thesis is a collection of three independent topics related to the computation of scattering properties of nonspherical ice crystals. In the next chapter, the GOM solution to light scattering by droxtal ice crystals will be discussed to provide a more realistic representation of small ice crystals in the uppermost portions of midlatitude and tropical cirrus clouds. In chapter III, the algorithm of current ADT will be enhanced. In chapter IV, the effects of the geometric shape, size, orientation and aspect ratio on the backscattering of the 94GHz radar wave by nonspherical ice crystals will be studied in the third part by employing the FDTD model. Finally, some potential problems and future works are discussed in chapter VI.

CHAPTER II

GEOMETRIC OPTICS SOLUTION TO LIGHT SCATTERING BY DROXTAL ICE CRYSTALS

Cirrus clouds, which regularly cover about 20% of the globe, play an important role in the energy balance of the earth-atmosphere system.[38] Radiative transfer modeling efforts have been hampered by the nonspherical nature of observed ice crystals in the atmosphere. Over the past several decades, substantial research efforts[39-47] have focused on deriving the single scattering properties of nonspherical ice crystals, which are fundamentally important to the interpretation of the remote sensing measurements of cirrus clouds and the parameterization of the bulk radiative properties of these clouds in climate models.[48,49]

In situ measurements of cirrus indicate that both the habit and size distribution of ice crystals tend to vary with height within the clouds.[1,50] Small ice crystals with aspect ratios approaching unity (i.e., the ratio of particle length to its width), often referred to as "quasi-spherical" particles, are predominant in the uppermost portions of midlatitude and tropical cirrus clouds[51]. Previous research indicates that the bidirectional reflectance of cirrus clouds is highly sensitive to the geometry of the small ice crystals in the uppermost region of cirrus clouds.[52] Most recently, McFarquhar et al.[53] showed the importance of small ice crystals in parameterizing the bulk radiative properties of cirrus clouds. The small ice crystals were treated as Chebyshev particles and the T-matrix method[54] was used to derive their scattering properties. Reichardt et al.[55] showed the lidar-based retrieval of polar stratospherical clouds is quite sensitive to the shape of small ice crystals. Liu and Mishchenko[56] treated small ice crystals as spheroids in the study of polar stratospheric clouds on the basis of lidar returns. Yang et al.[32] speculated that small ice particles observed in Alaskan ice fogs[57,58] may be similar to the shape of nonspherical small ice crystals in cirrus clouds. As we will discuss in the next section, droxtal-like crystals have also been observed in wave clouds, and may be associated with the freezing of supercooled water droplets and subsequent growth by water vapor deposition. In this situation, the rapid transition from supercooled water droplets to ice crystals through the homogeneous ice nucleation process, coupled with small amounts of available water vapor, may inhibit the development of more pristine particles such as hexagonal columns and plates.

The single scattering properties of ice droxtals have been investigated for the case of small size

parameters by using the FDTD method.[32] Substantial differences were noted between the single scattering properties for ice spheres and those for droxtals, especially at visible wavelengths. Because of computational limitations, the largest size parameter for which application of the FDTD method is practical is approximately 20, although it has been applied to size parameters up to 40 when no attempt is made to average the scattering properties over particle orientation.[59] For a droxtal with a size parameter of 20 defined with respect to the corresponding circumscribing sphere, the effective diameter is only 4.2 μm for a wavelength of 0.66 μm. Observations show that these small particles with aspect ratios on the order of unity are present at sizes greater than 30 μm. Obtaining scattering properties for crystal sizes larger than those allowed by the FDTD method requires the development and application of various approximate approaches such as the geometric optics (GO) method. Many exact and approximate scattering methods have been recently reviewed by Mishchenko et al.[6] and Kahnert.[7] The GO method is applicable when the size of equivalent volume sphere for the particle is much larger than the wavelength of the incident beam. The applicability of the GO method has been investigated via its comparison with the T-matrix method[61] and the FDTD method.[62,63] In this study we employ the Improved Geometric Optics (IGO) method developed Yang et al.[32] to compute the single scattering properties of droxtals. Because of the approximate nature of the IGO method, the present scattering computations are limited to size parameters in the geometric optics regime.

Droxtal Geometry and Coordinate Frame

Figure 1 shows images of droxtals collected in an orographic wave cloud that was penetrated by a balloon-borne ice crystal replicator in Colorado at a temperature near –40C (A. Heymsfield, National Center for Atmospheric Research, Boulder, Colorado, unpublished data). The wave cloud extended to a temperature of about –56C , and throughout the layer particles were present in high concentrations (~1cm^{-3}) and were uniform in size. The lines shown in the right panel of Fig. 1 indicate the size scale where the distance between two adjacent lines is 10 μm. Thus, the droxtals shown here are of the order of 30 μm diameter. Close scrutiny of these and other particle images indicates that these particles are not spherical. More detailed images of droxtals are provided by Ohtake[58] who also speculated on the three-dimensional (3D) structure of droxtals. Situations that are particularly amenable to droxtal production occur when the

homogeneous ice nucleation process is active, at temperatures below –35C , and include orographic wave clouds[65], vigorous convection,[66] and ice fog.[57]

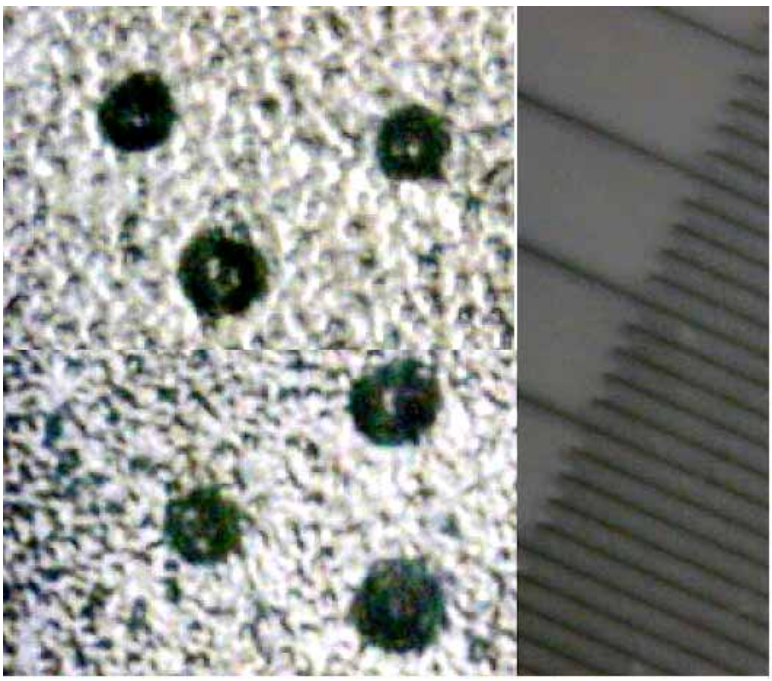

Fig. 1 Replicator images of small ice particles(dark objects in left image) observed for a wave cloud. (Heymsfield, unpublished data) The distance between two adjacent lines shown in the right panel is 10 μm. The particle sizes are approximately 30 μm.

To specify the geometry of a general convex particle such as the droxtal, we define a coordinate frame that is fixed to the particle (hereafter, referred to as the particle frame), as is shown in Fig. 2a. The origin of this frame coincides with the center of the mass of crystal. The z-axis of the frame passes through the center of the top face, whereas the corresponding x-axis points through the midpoint of the line $F'U$. Compared with a pristine hexagonal ice crystal, the geometry of a droxtal is much more complicated because of the

presence of 12 isosceles trapezoid faces (e.g., $ABB'A'$ in Fig. 2a), six rectangular faces in the center of the crystal, and a top and bottom hexagonal face, for a total of 20 faces. The geometric properties of droxtals

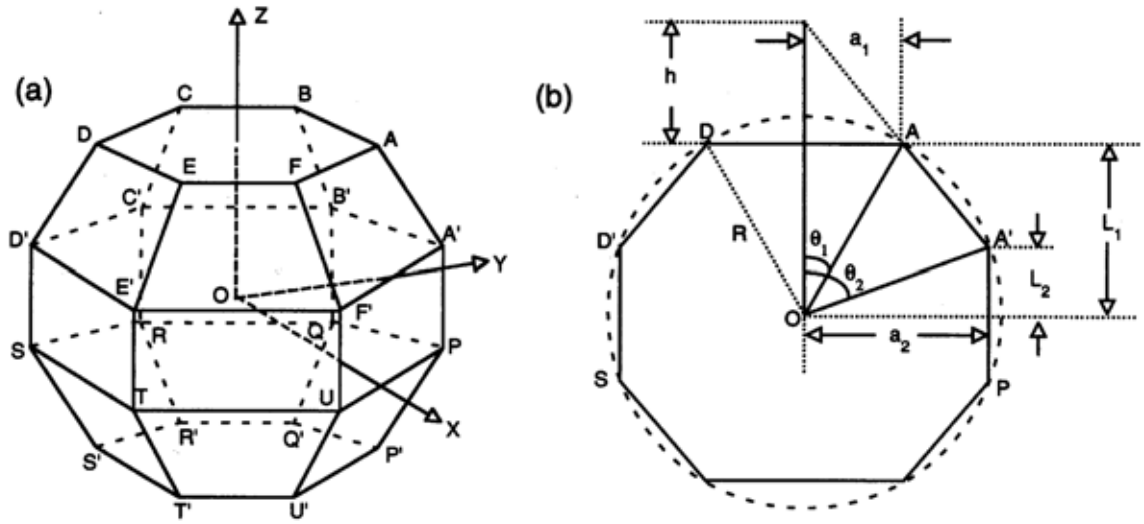

Fig. 2 (a) Geometric representation of a droxtal (b) Cross section of a droxtal (side view).

having maximum sphericity have been discussed by Yang et al.[32] When a particle has maximum sphericity, all the crystal vertices touch a circumscribing sphere. With maximum sphericity, the geometric properties of a droxtal can be fully specified in terms of three parameters, i.e., the radius of the circumscribing sphere R, and two angles θ_1 and θ_2 denoted in Fig. 2b. From the geometric configuration shown in Fig. 2b, we can obtain the following relationships:

$$a_1 = R\sin\theta_1,\ a_2 = R\sin\theta_2, \tag{2.1}$$

$$L_1 = R\cos\theta_1,\ L_2 = R\cos\theta_2, \tag{2.2}$$

$$h = a_1(L_1 - L_2)/(a_2 - a_1). \tag{2.3}$$

The quantities in Eqs.(2.1)-(2.3) are indicated in Fig. 2b. The other geometric properties of the droxtal,

such as the position vectors of the vertices and the unit vectors normal to the individual faces, can also be specified in terms of R, θ_1 and θ_2. For example, the unit normal vectors $\hat{n}_i = (n_{ix}, n_{iy}, n_{iz})$ associated with the six upper trapezoidal faces of the droxtal can be given as follows:

$$n_{i,x} = \sin\alpha \cos[\pi/2 + (i-1)\pi/3], \tag{2.4}$$

$$n_{i,y} = \sin\alpha \cos[(i-1)\pi/3], \tag{2.5}$$

$$n_{i,z} = \cos\alpha, \tag{2.6}$$

where i=1-6 in which i=1 denotes the case for face $ABB'A'$. The parameter α in Eq.(2.4) is the angle between the normal vector of an upper trapezoidal face (e.g., $ABB'A'$) and the z-axis, given by $\alpha = \cos^{-1}\{2(h + L_1 - L_2)/[3a_2^2 + 4(h + L_1 - L_2)^2]^{1/2}\}$. Given the normal vector of each face, the angle between any two different faces of a droxtal can be specified as follows:

$$\phi_{i,j} = \pi - \cos^{-1}(\hat{n}_i \cdot \hat{n}_j), \tag{2.7}$$

where $\hat{n}_i$ and $\hat{n}_j$ are the normal vectors of surfaces i and j, respectively.

The hexagonal geometry is a special case of the droxtal geometry. For example, as angle θ_1 approaches θ_2, the trapezoidal faces of the droxtal vanish and the particle becomes hexagonal. With appropriate specifications of the three parameters, one can specify hexagonal columns and plates with various aspect ratios and sizes. Similarly, the bottom and top faces can be minimized by properly specifying θ_1 and θ_2, leading to a double-pyramid shape. Note that some rarely-observed halos with angular radii different from 22 and 46 may be attributed to the refraction of rays associated with double-pyramid ice crystals, as articulated by Greenler[67] and references cited therein.

Initialize Ray-Tracing Calculation for Droxtal

The propagating direction of an incident ray with respect to the particle frame (e.g., the coordinate system *oxyz*) can be specified in terms of a unit vector $\hat{r}_i = (\sin\theta_p \cos\beta, \sin\theta_p \sin\beta, \cos\theta_p)$, in which θ_p is the zenith angle measured from the positive z-axis to $\hat{r}_i$, and β is the azimuth angle measured from the positive x-axis to the projection of $\hat{r}_i$ on the x-y plane. To initialize the ray tracing calculation for a given localized ray, one must specify the point where the incident ray first hits the particle. The initialization of the ray-tracing calculation in terms of the specification of incident rays and the points where they intersect

the crystal surface is straightforward in concept, but is quite complex in its numerical implementation, especially when the particle geometry is complicated. Here we present an efficient method for specifying the incident rays and the initial impinging points on the surface of a general convex particle.

To initialize the ray tracing calculation associated with a general convex particle, we envision a circular disk that is located at a certain distance from the particle. Let the disk be centered at $-L\hat{r}_i$ where L is a constant and $\hat{r}_i$ is the unit vector pointing along the incident direction. Furthermore, we assume that the radius of this disk is equal to that of the circumscribing sphere of the particle. Any incident ray beginning from a point outside the disk and propagating in the $\hat{r}_i$ direction will pass by the particle without intersecting it. Thus, we need to consider only the rays that pass through the region encompassed by the disk. In practice, we randomly select a point within this disk as the starting point for a ray. To cover the disk uniformly with incoming rays, the coordinate values for the points should be expressed as follows:

$$x_0 = R\sqrt{\xi_3}\cos(2\pi\xi_4)\cos\theta_p\cos\beta - R\sqrt{\xi_3}\sin(2\pi\xi_4)\sin\beta - L\sin\theta_p\cos\beta, \tag{2.8}$$

$$y_0 = R\sqrt{\xi_3}\cos(2\pi\xi_4)\cos\theta_p\sin\beta + R\sqrt{\xi_3}\sin(2\pi\xi_4)\cos\beta - L\sin\theta_p\sin\beta, \tag{2.9}$$

$$z_0 = -R\sqrt{\xi_3}\cos(2\pi\xi_4)\sin\theta_p - L\cos\theta_p, \tag{2.10}$$

where R is the radius of the circumscribing sphere of the particle, and ξ_3 and ξ_4 are two random numbers uniformly distributed between 0 and 1. If an incident ray starting at (x_0, y_0, z_0) and propagating in the direction of $\hat{r}_i$ can impinge on the droxtal, the ray tracing calculation is carried out; otherwise, a new incident ray is sampled.

To illustrate the present method for determining whether an arbitrary incident ray can intersect with a convex scattering particle, we consider a simplified two-dimensional (2D) scattering problem for which the scattering particle is assumed to be a rectangle. As illustrated in the left panel of Fig. 3a,, an incident ray starting at point O_1 intersects the rectangle. For a given incident direction, the condition for the illumination of a side of the rectangle is that its outward-pointing normal vector must face towards the incoming ray. Thus, sides 3 and 4 of the rectangle are prospective sides to be illuminated (hereafter, these two sides are referred to as 'possible sides'). Note that sides 1 and 2 can never be illuminated (hereafter, these two sides are referred to as 'impossible sides'). Let the distances from point O_1 to the 'possible sides'

3 and 4 be d_3 and d_4 (hereafter, 'possible distances'), of which d_3 is larger. Furthermore, let the distances between point O_1 to the 'impossible sides' 1 and 2 be D_1 and D_2 (hereafter, 'impossible distances'), of which D_2 is smaller. From the left panel of Fig. 3a, it is evident that $d_3 < D_2$, i.e., the maximum value for the 'possible distances' is smaller than the minimum value of the 'impossible distances'. However, the opposite situation occurs if the incident ray passes the particle without an intersection, as shown in the right panel of Fig.3a. In this case, the maximum value of 'possible distances' is larger than the minimum value of the "impossible distances", i.e., $d_3 > D_2$. This geometric property illustrated in the left and the right panels of the Fig. 3a provides a criterion for determining whether an incident ray can intersect with the particle. Mathematically, the criterion can be expressed as follows:

(1) If $\max(d_i) < \min(D_j)$, an incident ray intersects with the particle, as is the case shown in the left panel of Fig. 3a.

(2) If $\max(d_i) > \min(D_j)$, an incident ray passes by the particle without intersecting it, as is the case shown in the right panel of Fig. 3a.

In the preceding criteria, $\max(d_i)$ indicates the maximum value of d_i in which i=3 and 4, whereas $\min(D_j)$ indicates the minimum value of D_j in which j=1 and 2. Note that the values of d_i and D_j can be negative. The present method is suitable for all two- and three-dimensional convex particles no matter how complex the particle surfaces may be. As an example, Fig. 3b shows the specification of the incident rays and their corresponding impinging points on a droxtal particle by this method. The circular area bounded by the dotted line indicates the region where starting points of the incident rays are sampled on a plane perpendicular to the direction of incidence. The solid lines indicate the projection of the droxtal along the incident direction. The dots indicate the projections of the incident rays that intersect with the particle, and the small crosses that are outside the particle projection indicate those incident rays that pass by the particle without intersecting it.

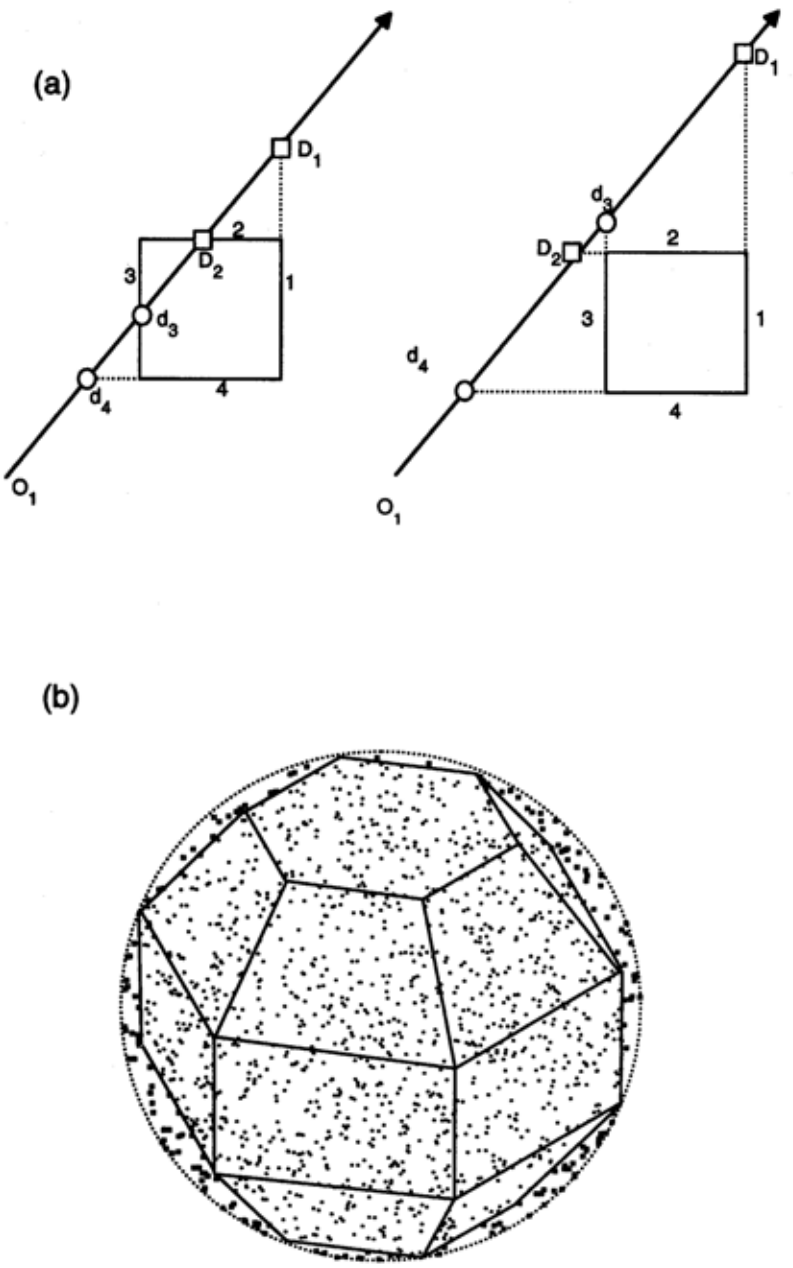

Fig.3 (a) Conceptual diagram to illustrate the method for determining whether an incident ray can intersect with a convex scattering particle in the ray-tracing calculation (left panel: the ray intersects with the particle; right panel: the ray passes the particle). (b) The results where the sampled incident rays impinge on the surface of a droxtal and those that pass the particle without intersecting it.

Diffraction

The contribution of diffraction to the scattering matrix can be expressed as follows[47]

$$S_d = \frac{k^2 D}{4\pi}\begin{bmatrix} \cos\theta + \cos^2\theta & 0 \\ 0 & 1+\cos\theta \end{bmatrix}, \tag{2.11}$$

$$D = \iint_P \exp(ik\hat{r}_s \cdot \vec{\xi}) d^2\xi, \tag{2.12}$$

where the domain of the integration in Eq. (2.12), *P*, is the projected area of the droxtal on a plane perpendicular to the incident direction, k is the wave number, θ is the diffraction angle, $\hat{r}_s$ is a unit vector in the scattering direction, and $\vec{\xi}$ is the position vector of a point in the integration domain. Under different orientation conditions, the projection of a droxtal can vary from a hexagon to a dodecagon, as illustrated in Fig. 4. To perform the integration in Eq.(2.10) for a specific particle orientation, we divide the projection of the particle onto a surface into small triangles that share a vertex at the origin. As an example, let us consider the dodecagonal projection. This projected area can be divided into 12 small triangles. If we denote the twelve apices of the dodecagon in terms of their position vectors i=1-13 (note that $\vec{r}_{13}=\vec{r}_1$, as shown in Fig. 4d), the position vector for an arbitrary point within the *i*th triangle can be decomposed into two vectors as follows:

$$\vec{\xi} = \varepsilon(1-\eta)\vec{r}_i + \eta\varepsilon\vec{r}_{i+1}\ ,\ i = 1-12, \tag{2.13}$$

where $\vec{r}_i$ and $\vec{r}_{i+1}$ constitute the neighboring two sides of the triangle i, $\varepsilon \in [0,1]$ and $\eta \in [0,1]$ are two parameters that determine the position of $\vec{\xi}$ in the triangle. Upon the substitution of Eq.(2.13) into Eq. (2.12), the integration of phase variation over these small triangles can be transformed to the integration over the ε and η space. With some mathematical manipulation, it can be shown that

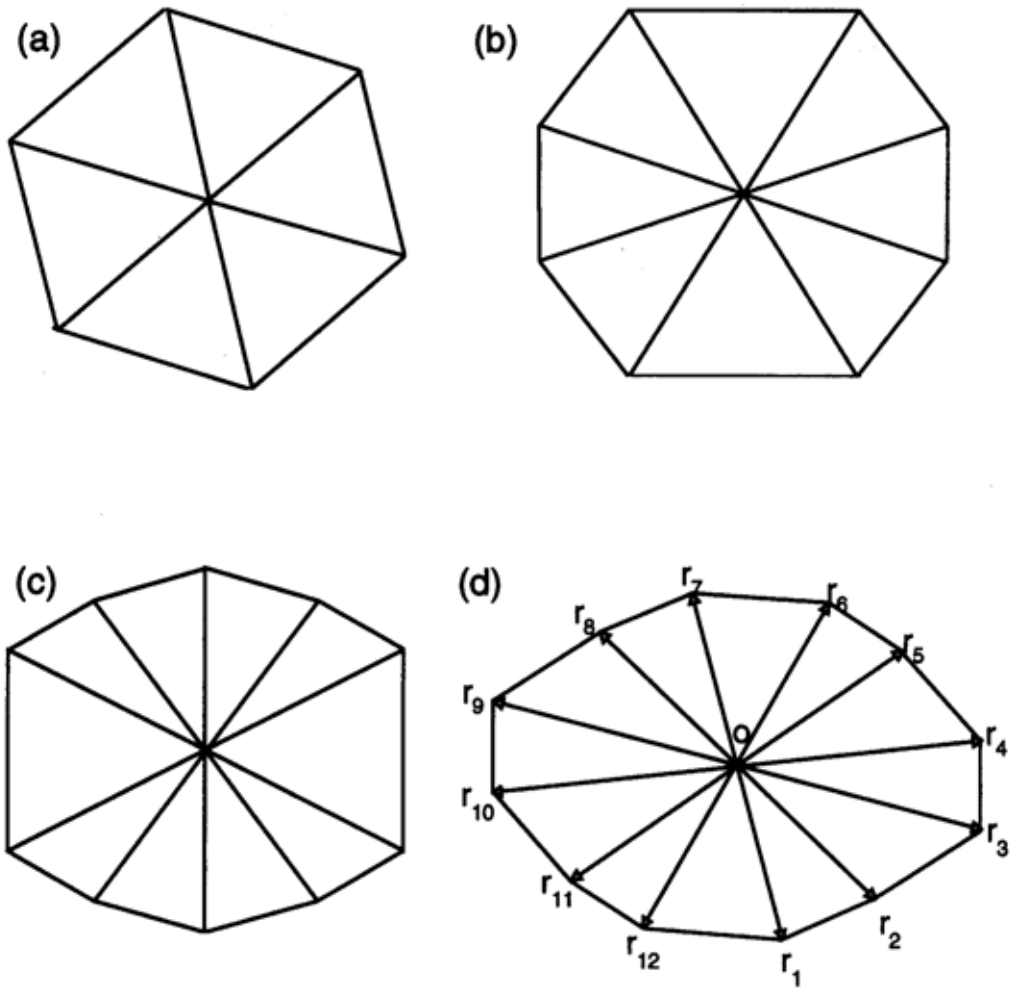

Fig. 4 All possible projections of a droxtal with various orientations relative to the incident direction.

$$D_i = \iint_{triangle_i} \exp(ik\hat{r}_s \cdot \vec{\xi}) d^2\xi = |\vec{r}_i \times \vec{r}_{i+1}| \int_0^1 \int_0^1 \exp\{ik\hat{r}_s \cdot [\varepsilon(1-\eta)\vec{r}_i + \eta\varepsilon\vec{r}_{i+1}]\} \varepsilon d\eta d\varepsilon$$

$$= \frac{|\vec{r}_i \times \vec{r}_{i+1}|}{ik\hat{r}_s \cdot (\vec{r}_{i+1} - \vec{r}_i)} \left\{ \exp(ik\hat{r}_s \cdot \vec{r}_{i+1}/2) \frac{\sin(k\hat{r}_s \cdot \vec{r}_{i+1}/2)}{k\hat{r}_s \cdot \vec{r}_{i+1}/2} - \exp(ik\hat{r}_s \cdot \vec{r}_i/2) \frac{\sin(k\hat{r}_s \cdot \vec{r}_i/2)}{k\hat{r}_s \cdot \vec{r}_i/2} \right\}. \quad (2.14)$$

The quantity D in Eq. (2.12) can be obtained in a straightforward manner by summing over D_i. One can use the symmetric property of the particle projection to simplify the summation process. Noting that $\vec{r}_i$ and $\vec{r}_{i+6}$ (i=1-6) are oppositely directed about the origin, that is,

$$\vec{r}_i = -\vec{r}_{i+6}, i = 1-6. \quad (2.15)$$

This symmetric property of the particle projection will result in the imaginary parts of D_i and D_{i+6} canceling each other in the summation. Thus, one can obtain an analytical expression for D as follows:

$$D = \sum_{i=1}^{6} (D_i + D_{i+6}) = \sum_{i=1}^{5} 2|\vec{r}_i \times \vec{r}_{i+1}| \frac{(\cos q_i - 1)/q_i - (\cos q_{i+1} - 1)/q_{i+1}}{q_{i+1} - q_i}$$

$$-2|\vec{r}_6 \times \vec{r}_1| \frac{(\cos q_6 - 1)/q_6 + (\cos q_1 - 1)/q_1}{q_6 + q_1}, \quad (2.16)$$

where $q_i = k\hat{r}_s \cdot \vec{r}_i$, in which $i = 1-6$. The expression in Eq.(2.16) is similar to that reported by Yang and Liou[46] for the case of hexagonal ice crystals.

Numerical Results and Discussions

The present numerical computation is carried out for two wavelengths at 0.66 and 11μm, for which the refractive indices of ice[68] are $1.3078+1.66\times10^{-8}i$ and $1.0925+2.48\times10^{-1}i$, respectively. Because very small particles in the atmosphere tend not to have preferred orientations, we assume droxtals to be randomly oriented in space. In the numerical computations we average the single-scattering properties of the particles over 200,000 random orientations.

As discussed before, hexagonal columns and plates can be viewed as special cases of droxtals with appropriate configurations of θ_1 and θ_2. To validate the IGO method developed in this study, we first compare the results computed from our IGO method to results by Yang and Liou for hexagons. Figure 5 shows the phase function P_{11} computed from the two models for randomly orientated hexagonal ice columns (L/a=100μm/20μm) and plates (L/a=50μm/100μm) at a wavelength of 0.66 μm, where L denotes the length or the column (or the thickness of the plate) and a is the semi-width of the particle cross section. The droxtal geometry that reduces to the hexagonal column is specified by R=53.85 μm and $\theta_1=\theta_2$=21.8 . For the plate, the corresponding droxtal configuration is R=103.12 μm and $\theta_1=\theta_2$=76.0 . It is evident from Fig.5 that the phase functions computed by the two different computational codes are essentially the same.

Figure 6 shows the six nonzero elements of the phase matrix calculated at the wavelength of 0.66 μm for a randomly-oriented droxtal ice crystal with R=50 μm and θ_1=32.35 and θ_2=71.81 . Note that the size parameter of the droxtal ($2\pi R/\lambda$) is approximately 476 in this case. For a given value of R, a droxtal with these values of θ_1 and θ_2 possesses the maximum possible volume. For the phase function P_{11}, the strong forward scattering is caused by diffraction and also by the refraction through various pairs of parallel crystal faces. A pronounced scattering peak can be seen at a scattering angle of 11 . This peak is also observed for the phase function of an individual bullet-shaped crystal and also bullet rosettes.[69] The minimum deviation angle θ_m associated with ray refraction through

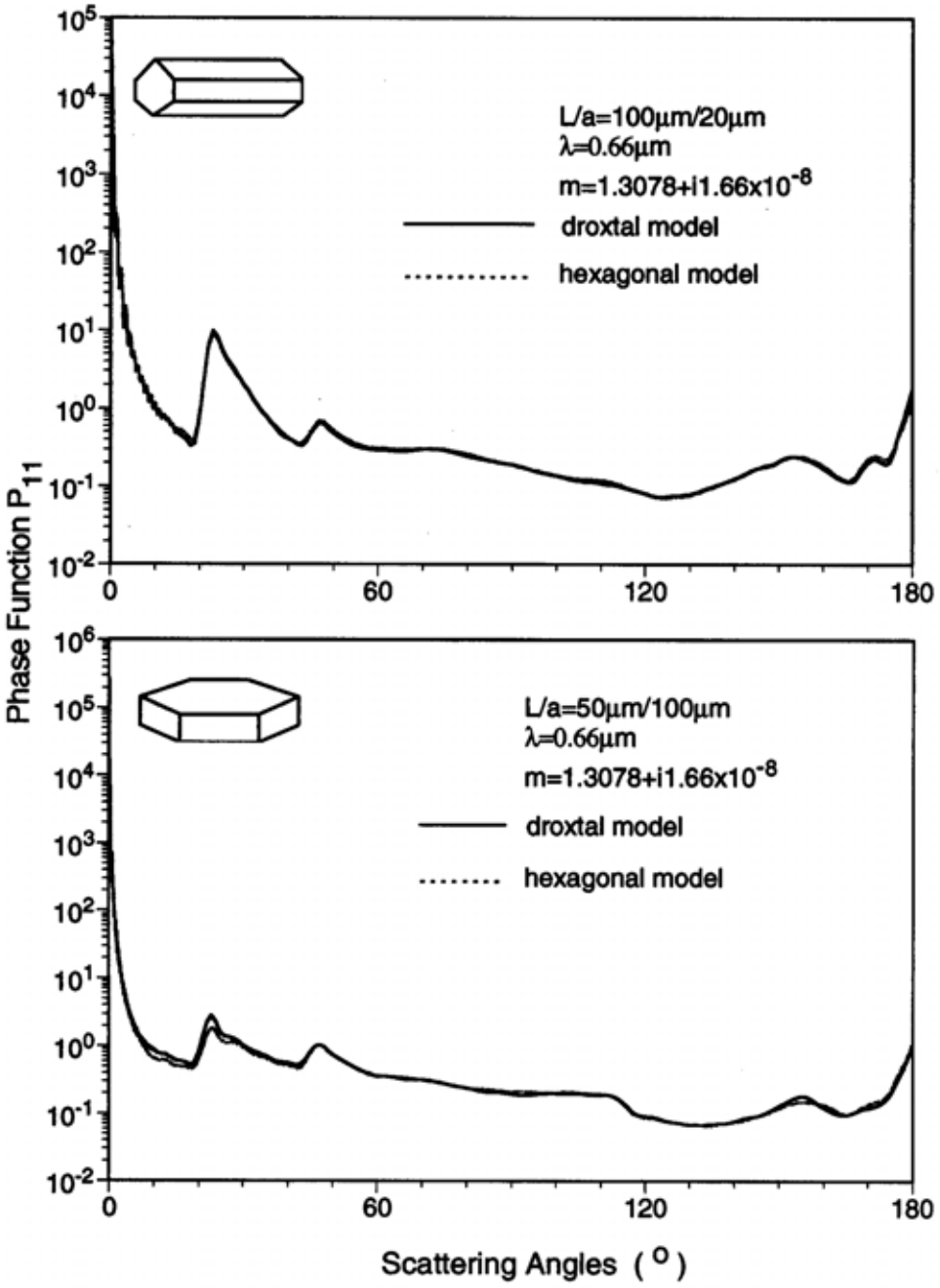

Fig. 5 Phase matrix computed by two models for randomly orientated hexagonal ice columns and plates.

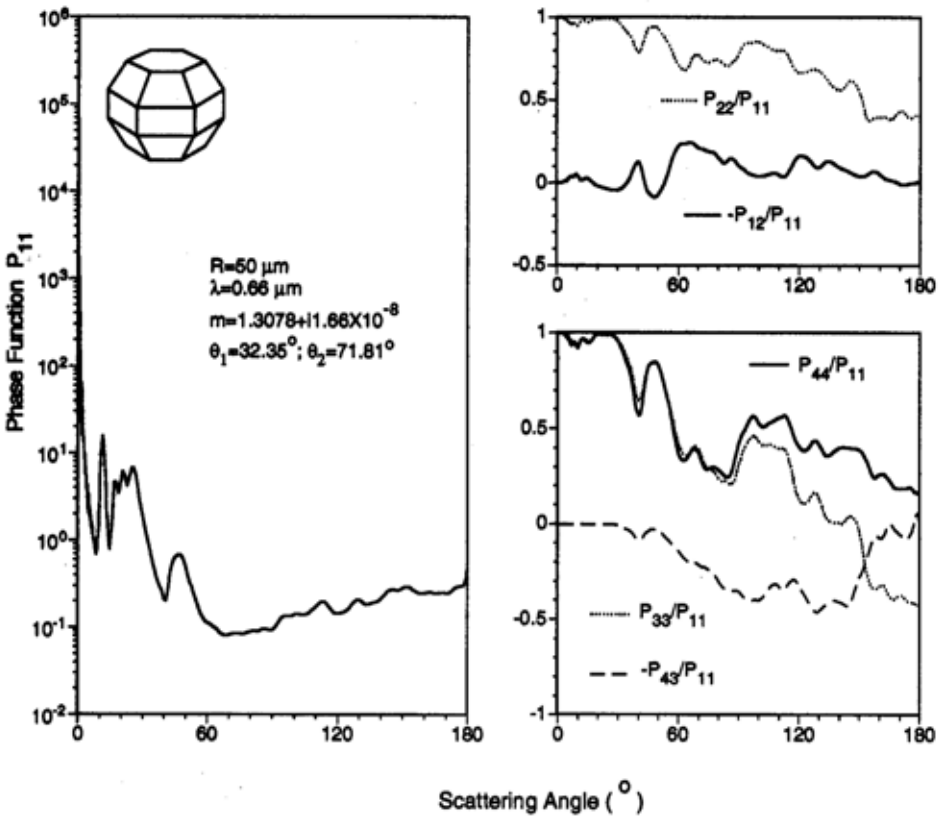

Fig. 6 Non-zero elements of the phase matrix for a droxtal at a wavelength of 0.66μm, with the geometric configuration of R=50μm, θ_1=32.35^0 and θ_2=71.81^0.

two faces inclined at an angle Δ can be calculated via the following equation:[5]

$$\theta_m = 2\sin^{-1}\left(m\sin\frac{\Delta}{2}\right) - \Delta, \tag{2.17}$$

where m is the real part of the refractive index. Based on Eq. (2.17), the peak at 11 can be explained by two sequential refractions through a trapezoidal face such as $ABB'A'$ and a recangular face such as $D'E'TS$ (see Fig. 2a). These two faces are inclined at an angle of 34 , and the corresponding minimum deviation angle for a real refractive index m =1.3078 is 11 . Three small peaks are seen over a broad scattering maximum that ranges from 16 to 26 including the well known 22 halo. The other two scattering maxima at 16 and 26 can be explained by the minimum deviation angles associated with two sequential refractions of rays through a prism angle of 48 and 68 respectively. The angles between any two faces of a droxtal with θ_1=32.35 and θ_2=71.81 are listed in Table 1, which also lists the minimum deviation angles calculated by Eq. (2.17) using the refractive index of ice at 0.66 μm. Evidently, the broad scattering maxima region in the phase function between 16 and 26 is the result of contributions by five possible face combinations. There are three possible combinations that contribute to the scattering maxima around 46 . Because of the presence of twelve trapezoidal faces and the decrease of the portion of rectangular crystal surfaces for droxtals in comparison with hexagons, the scattering maximum at 150 caused by multiple total internal reflections becomes much smaller than that in the case for hexagons. The degree of linear polarization can be represented by $-P_{12}/P_{11}$ when the incident ray is unpolarized. Figure 6 shows that a negative polarization is associated with the 22 and 46 halos and in the vicinity of pure backscatter (180). The element P_{22}/P_{11} is related to the depolarization of scattering light when the incident rays are linearly polarized. This element is also a good indicator of the asphericity of the droxtal Positive values are noted for P_{22}/P_{11} for the entire scattering angular domain. Values for element $-P_{43}/P_{11}$ are essentially negative, except for a small positive peak located in the vicinity of 177 . The values of P_{33}/P_{11} and P_{44}/P_{11} are approximately equal for the scattering angles ranging from 0 to 90 . At scattering angles larger than 90 , P_{33}/P_{11} becomes negative, whereas P_{44}/P_{11}remains positive. Because of the hexagonal structure, the phase matrix elements of droxtals are similar to those of hexagons, as is evident from a comparison of the present results and those shown by Takano and Jayaweera.[41]

Table 1. The minimum deviation angles associated with various combinations of the particle faces

Angle Δ	Face combination	Minimum deviation angle θ_m
0^0	top-bottom *ABB' A' - STT' S* *A' B' QP - D' E' TS*	0^0
34^0	*ABB' A' - D' E' TS*	12^0
49^0	*ABB' A' - RSS' R'*	17^0
56^0	*ABB' A'* -bottom *PQQ' P'* -top	19.8^0
60^0	*A' B' QP - C' D' SR*	21.7^0
65.5^0	*ABB' A' - C' D' SR*	24.6^0
68^0	*ABB' A' - DEE' D'*	26^0
88^0	*ABB' A' - CDD' C'*	42.6^0
90^0	*A' B' QP*-top *A' B' QP*-bottom	46^0
91.8^0	*ABB' A' - QRR' Q'*	48^0
112^0	*ABB' A' - PQQ' P'*	
114.5^0	*ABB' A' - B' C' RQ*	
120^0	*A' B' QP - B' C' RQ*	
124^0	*ABB' A'* -top *PQQ' P'* -bottom	
131^0	*ABB' A' - BCC' B'*	

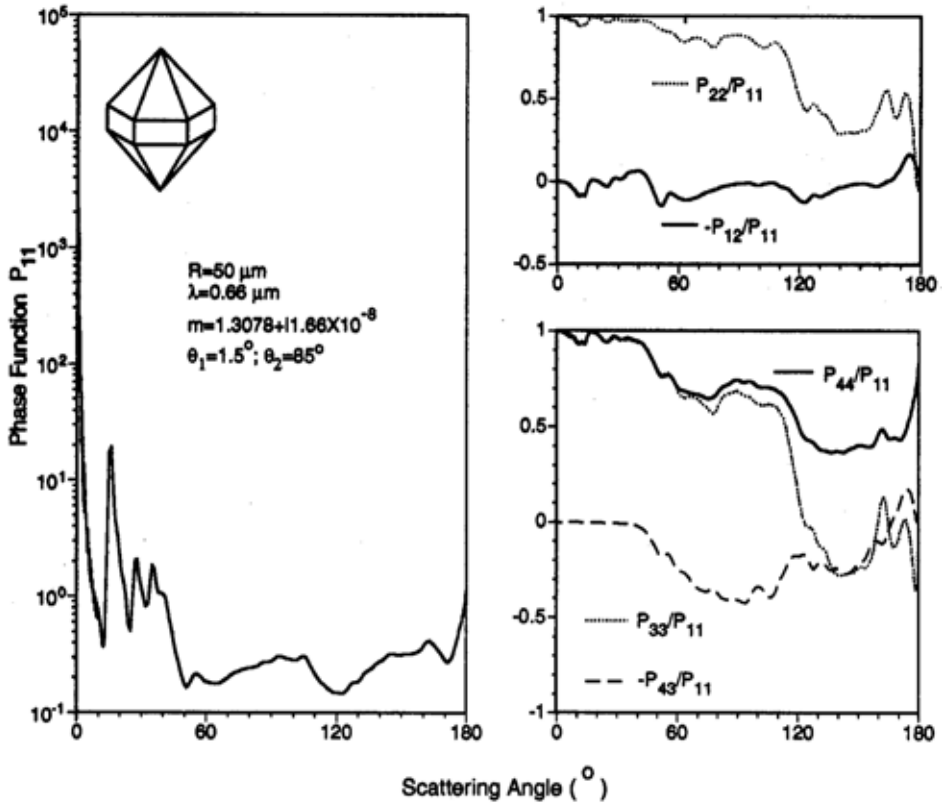

Fig.7 Non-zero elements of the phase matrix for a droxtal at a wavelength of 0.66μm, with the geometric configuration of R=50μm, θ_1=1.5^0 and θ_2=85^0.

Figure 7 shows the scattering phase matrix of a droxtal with R=50 μm, θ_1=1.5 and θ_2=85 at the 0.66 μm wavelength. Because θ_1 is very small, the top and the bottom faces essentially shrink to a point and the surface area of each of the pyramidal faces is substantially increased. Thus there are 18 faces for this configuration compared to the twenty faces for the droxtal discussed previously. Compared with the phase function of the droxtal shown in Fig. 6, the forward scattering maximum for this crystal is slightly larger due to an increase of the diffracted energy. A pronounced scattering peak located at 15 is seen for

P_{11}, whose formation mechanism is very similar to that for the 11 halo in Fig. 6. Because of the absence of the top and bottom faces, the scattering maximum near 46 caused by the refraction through the top or bottom faces and a central face is negligible. The increase in the area of the trapezoidal faces reduces the scattering peak corresponding to the 22 halo. By comparing the phase functions shown in Figs. 6 and 7, one notices significant differences for scattering angles ranging from 140 to 160 . For other phase matrix elements, the overall features shown in Figs. 6 and 7 are similar. However, significant differences are noticed in the backscattering direction for these two cases, particular for P_{44}/P_{11} and P_{22}/P_{11}. This behavior may have implications for spaceborne or ground-based measurements by depolarized lidars.

Figures 8 and 9 show the non-zero elements of the phase matrix for two different droxtal geometries at the infrared (IR) wavelength of 11 μm. Compared with those calculated at a visible wavelength, phase functions in the IR are essentially featureless in side-scattering and backscattering directions. This behavior can be ascribed to substantial absorption within the ice particles at this amount. Because diffracted energy is concentrated in the forward direction, the phase matrix in the side-scattering and backscattering directions are essentially attributed to the external reflection of rays.[70] The oscillation in the phase function P_{11} is associated with the diffraction component of the scattered energy. The present results confirm that in the IR, detailed geometrical information of the particle such as edges and corners becomes less important and the diffraction component of scattering dominates the pattern of the phase function, as has been noted in previous studies (e.g., Lee et al.[71]). As evident from Figs. 8 and 9, the phase matrix elements associated with the polarization configuration of scattered light are insensitive to the detailed particle geometry. Evidently, the feature associated with external reflection is insensitive to the particle geometry under the assumption of random particle orientation.

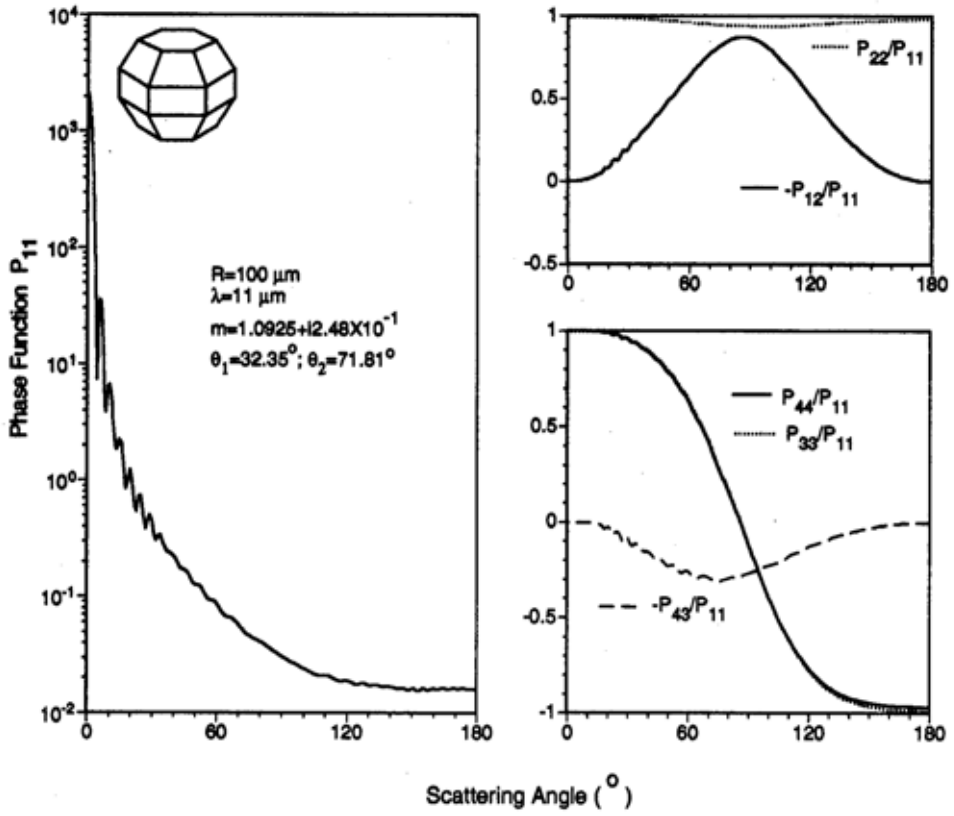

Fig. 8 Non-zero elements of the phase matrix for a droxtal at a wavelength of 11μm, with the geometric configuration of R=100μm, θ_1=32.35^0 and θ_2=71.81^0.

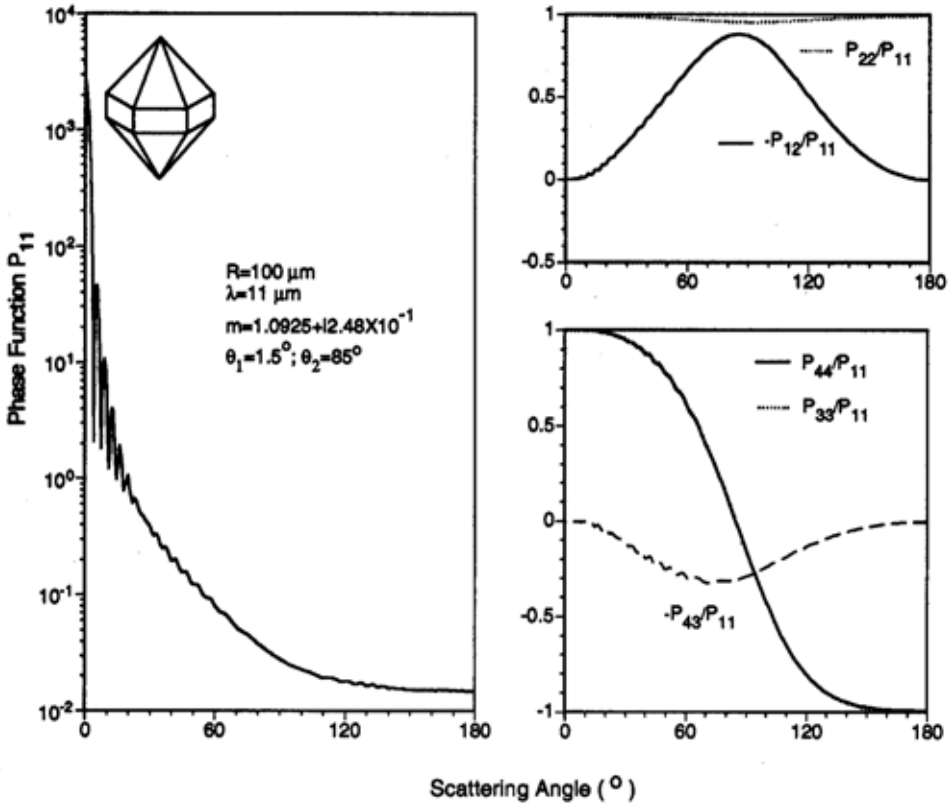

Fig. 9 Non-zero elements of the phase matrix for a droxtal at a wavelength of 11μm, with the geometric configuration of R=100μm, θ_1=1.5^0 and θ_2=85^0.

Figure 10 shows the linear depolarization ratios δH and δV for four types of ice crystals (hexagonal columns, plates, 20-faced droxtal, 18-faced droxtal), where δH and δV are defined respectively, as follows[5]:

$$\delta H = \frac{P_{11} - P_{22}}{P_{11} + 2P_{12} + P_{22}}, \tag{2.18a}$$

$$\delta V = \frac{P_{11} - P_{22}}{P_{11} - 2P_{12} + P_{22}}. \tag{2.18b}$$

For hexagonal columns and plates, there is a notable difference between δV and δH at nearly backward scattering direction (i.e., $\theta \approx 178$), whereas for the droxtal ice crystals the difference is not as pronounced. Because of the hexagonal structures, the value of δV and δH for all crystals display peaks in the angular region $2 < \theta < 20$. This phenomena has been discussed by Takano and Jayaweera[5]. At the backscattering direction θ=180 , linear depolarization ratios for droxtals with θ_1=32.35 and θ_2=71.81 (i.e., the 20-faced droxtal) has the smallest value among these four kinds of ice crystals and the 18-faced droxtal with θ_1=1.5 and θ_2=85 has the largest values.

In reality, the geometry of droxtal ice crystals cannot be confined to a specific combination of θ_1 and θ_2. Figure 11 shows the average of the 0.66-μm phase function P_{11} over different combinations of θ_1 and θ_2. As shown in the diagram, the values of θ_1 and θ_2 are assumed to follow two Gaussian distributions centered at 32.35 and 71.81 ° respectively. These distributions for θ_1 and θ_2 imply that droxtals with the maximum volume configuration (i.e., θ_1=32.35 and θ_2=71.81) are the most prevalent among all possible droxtal configurations in cirrus clouds. Let $W_1(\theta_1)$ and $W_2(\theta_2)$ be the probability weightings specified by the Gaussian distributions. Thus, the average phase function can be obtained as follows:

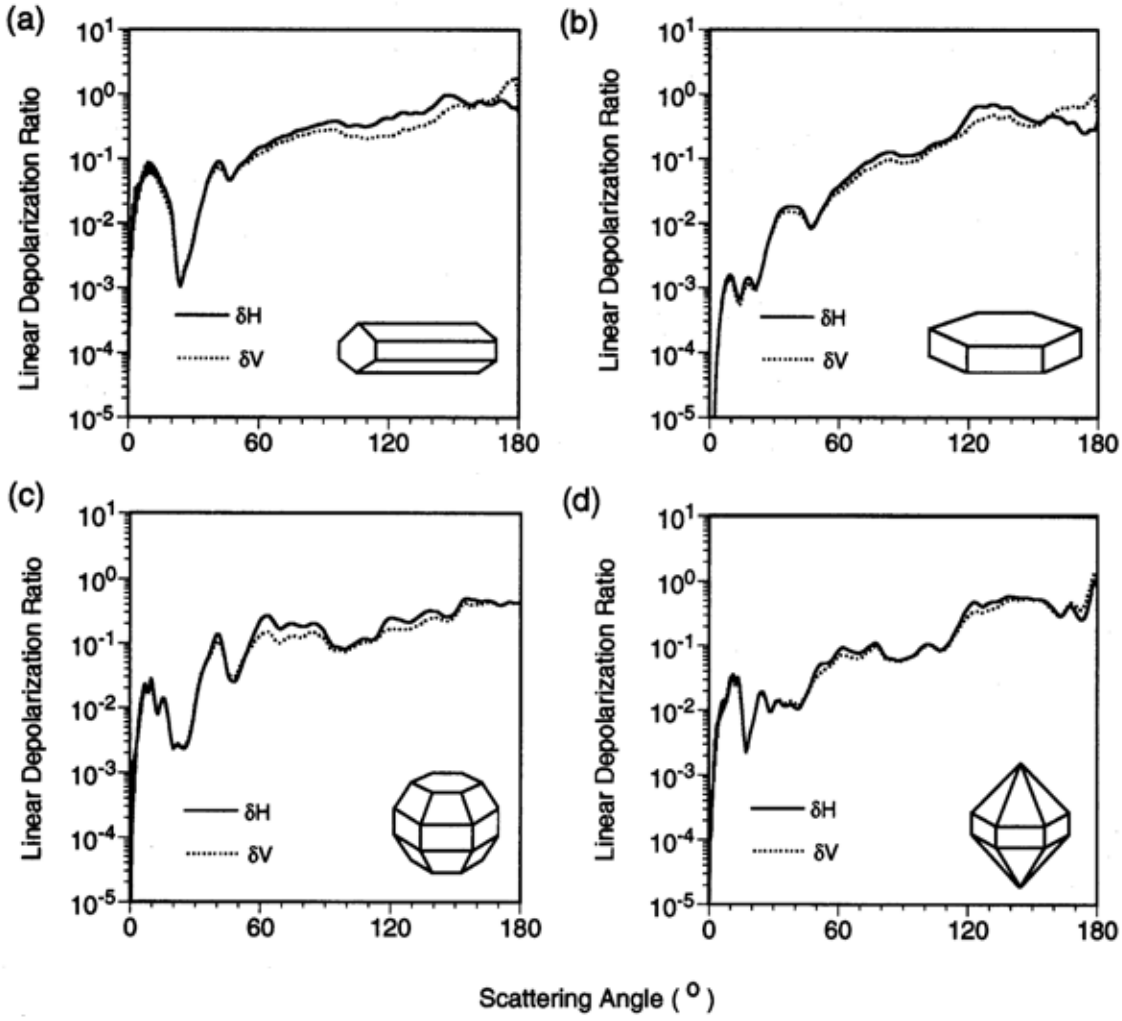

Fig. 10 Linear depolarization ratio for droxtal and hexagonal ice crystals at a wavelength of 0.66μm.

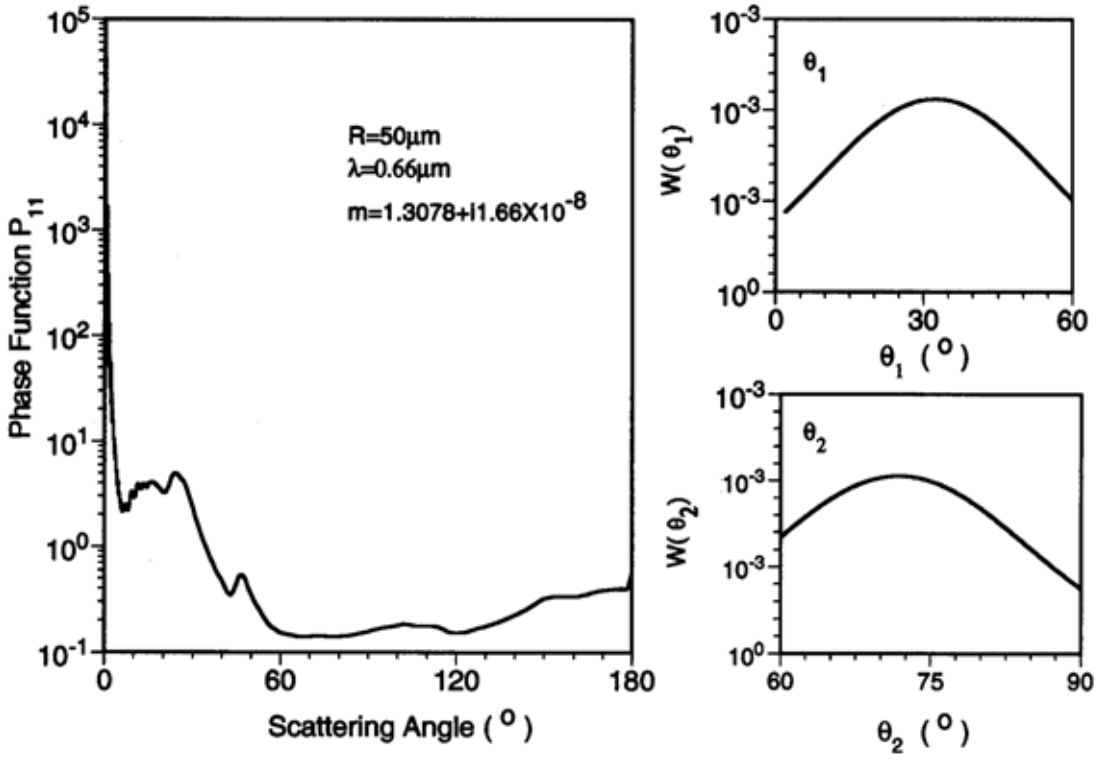

Fig. 11 The phase function of droxtals averaged over various combinations of θ_1 and θ_2.

$$\overline{P}_{11}(\theta_s) = \frac{\int_{\theta_1}\int_{\theta_2} P_{11}(\theta_s;\theta_1,\theta_2)W_1(\theta_1)W_2(\theta_2)\sigma_s(\theta_1,\theta_2)d\theta_1 d\theta_2}{\int_{\theta_1}\int_{\theta_2} W_1(\theta_1)W_2(\theta_2)\sigma_s(\theta_1,\theta_2)d\theta_1 d\theta_2}, \tag{2.19}$$

where σ_s is the single scattering cross section. The 22 and 46 halos become pronounced in the averaged phase function $\overline{P}_{11}$. We also note that the average over different geometric configurations smoothes out the scattering peaks occurring at small angles such as 11 , as well as those small oscillations in side and backscattering directions. Compared with the case for hexagonal ice crystals, the scattering phase function averaged over various droxtal configurations is quite unique, particularly, in the 22 , 150 and backscattering angular regions.

Summary and Conclusions

The phase function of the droxtals at the visible wavelength (0.66 μm) displays maxima at scattering angles smaller than 22 . The maxima may be explained by consideration of multiple scattering within the particle resulting from the pyramidal faces. Because of the hexagonal structure of the crystal facets, all elements of scattering matrix show similarities to the properties that have been observed in those of hexagonal ice crystals. At 11 μm, where absorption of the incident radiation within the particle becomes dominant, the phase functions of the 18-faced and 20-faced droxtals are essentially featureless. A comparison of the linear depolarization between hexagonal ice crystals and droxtal ice crystals suggests that there is a notable difference at the backscattering angles. This difference is also observed between droxtal ice crystals with different geometric configurations. Finally, we note that the average of the phase function over various geometric configurations effectively smoothes out the small oscillations, especially in the backscattering directions.

CHAPTER III

A NEW ALGORITHM FOR THE ANOMALOUS DIFFRACTION THEORY (ADT)

Although a number of rigorous methods (see, Mishchenko et al[6]., Kahnert[7], Wriedt[25], and references cited therein) have been developed for calculating the optical properties of nonspherical particles, the Anomalous Diffraction Theory (ADT) originally developed by van de Hulst[3] is still an effective alternative for the computation of the extinction and absorption cross sections of a particle when it is optically tenuous. The popularity of ADT is demonstrated by the number of recent publications on this subject.[71-81] The merits of ADT are its simplicity in concept and efficiency in numerical computation, although this method suffers some shortcomings, such as missing the above-edge contribution as illustrated by Baran et al.[13] Mitchell[36] has substantially improved the accuracy of ADT in the spherical case by parameterizing the missing physics, specifically, the internal reflection/refraction, photon tunneling, and edge diffraction**.** The edge effect has been previously investigated by Jones[82,83] and Nussenzveig and Wiscombe.[84] Most recently, Zhao and Hu[35] developed a general bridging technique to include the particle edge contribution in the ADT computation.

In the ADT framework, the incident electromagnetic wave can be regarded as a number of small localized waves that propagate towards a scattering particle along the incident direction without divergence. The path of a localized wave, a straight ray-tube with a finite cross section, is referred to as a projectile. The propagating direction and polarization configuration of the internal field inside the particle are assumed to be the same as those of the incident wave. However, the internal field suffers a phase delay due to the presence of the scattering particle. The extinction cross section is associated with the phase interference of the individual projectiles, whereas the corresponding absorption cross section is the summation of the absorption of all the projectiles. For well-defined regular geometries such as spheres,[3] spheroids,[74] circular cylinders,[75-77] cubes[78,79] and hexagons,[80] analytical ADT solutions can be obtained. It is unlikely that an analytical ADT solution can be derived for a general nonspherical geometry. Thus, a numerical method must be used to account for the contributions of

individual projectiles. The accuracy of the numerical computation depends on the dimensions of the cross sections of the projectiles. In practice, the linear dimensions of the projectiles need to be much smaller than the incident wavelength so that one can account accurately for the coherent phase interference of the transmitted wave that penetrates the particle. If the size parameter (i.e., the ratio of particle size to the incident wavelength) is large, however, the number of the projectiles required can be extremely high, leading to a significant computational effort. The computational burden may be further aggravated if the numerical computation needs to be reiterated for various size parameters and spectral wavelengths, particularly when a random orientation condition is assumed for the particles.

The computation of the extinction and absorption cross sections in the ADT framework is independent of the order in which the contributions of individual projectiles are accounted for. For example, the ADT solution to the absorption cross section, given by a discrete summation of the absorption of individual projectiles used in the numerical computations, is irrelevant to the order of the projectiles in the summation. Furthermore, the projected-area distribution (i.e., the percentage of the particle projected area that corresponds to the projectile-length in a specific interval) is independent of the particle's physical size if the shape and aspect ratio of the particle remain the same. These features allow ADT to be formulated in a more computationally efficient manner. Most recently, Xu et al.[85] and Xu[86] introduced the probability distribution function of the geometric paths of rays inside particles and reformulated the conventional ADT solutions for the extinction and absorption cross sections of a particle. In terms of methodology, we notice that the conventional ADT formulation and that developed by Xu et al.[85] are similar to the line-by-line method and the k-distribution method, respectively. The line-by-line and k-distribution methods are developed for calculating the gaseous spectral transmittance over a given wavenumber interval. The details of the line-by-line and k-distribution methods can be found in Goody and Yung,[87] Liou,[88] Chou and Kouvaris,[89] Lacis and Oinas,[90] Fu and Liou,[91] and Kratz.[92] Furthermore, we notice that the new ADT formulation developed by Xu et al.[85] can be further enhanced to increase the computational efficiency.

There are two goals for this second part of this thesis. First, to enhance the algorithm developed

by Xu et al.[85] and Xu,[86] we introduce a dimensionless scaled projectile-length ($\tilde{l}_q$) that is specified in the domain of cumulative projected-area distribution (q). The scaled projectile length quantitatively describes the behaviors of the distribution of projectile-length inside the particle. Using $\tilde{l}_q$, we develop a computationally efficient ADT algorithm. Second, to reduce the errors of ADT for its implementation for moderate refractive indices, we also modify the conventional ADT formulation by applying the ADT assumption for the internal field to two rigorous relationships in classic electrodynamics, which relate the extinction and absorption cross sections to the internal electric field inside the particle.

ADT Algorithm in Cumulative Projected-Area Distribution Domain

The physical rationale associated with ADT for computing the extinction and absorption cross sections (or efficiencies) of optically tenuous large particles has been well explained by van de Hulst[3]. Without recapturing the physical base and the applicability criteria for ADT, we present the conventional ADT formulae for computing the extinction and absorption cross sections of an arbitrarily shaped particle with a specific orientation as follows:

$$C_{ext} = 2\,\mathrm{Re}\left\{\iint_P [1 - e^{ikl(m-1)}]dP\right\},$$

$$= 2\iint_P \left\{1 - e^{-klm_i}\cos\left[kl(m_r - 1)\right]\right\}dP, \tag{3.1}$$

and

$$C_{abs} = \iint_P (1 - e^{-2klm_i})dp, \tag{3.2}$$

where $k = 2\pi/\lambda$ is the wave constant in which λ is the incident wavelength, $m = m_r + im_i$ is the complex refractive index of the particle, m_i is the imaginary part of m, the integral domain in Eqs. (3.1) and (3.2) are the projected area of the particle on a plane perpendicular to the incident direction, and l is the length of the projectile segment within the particle.

As shown in Fig. 12 , the incident wave is along the z-axis. The projectile-length within the scattering particle can be expressed as follows:

$$l = \hat{z}\cdot(\vec{r} - \vec{r}_0) = l(x, y), \tag{3.3}$$

where $\hat{z}$ is a unit vector along the z axis. The projectile-length, $l(x,y)$, depends on the location where the incident projectile intercepts with a plane normal to the incident direction (i.e., the plane P in Fig. 12).

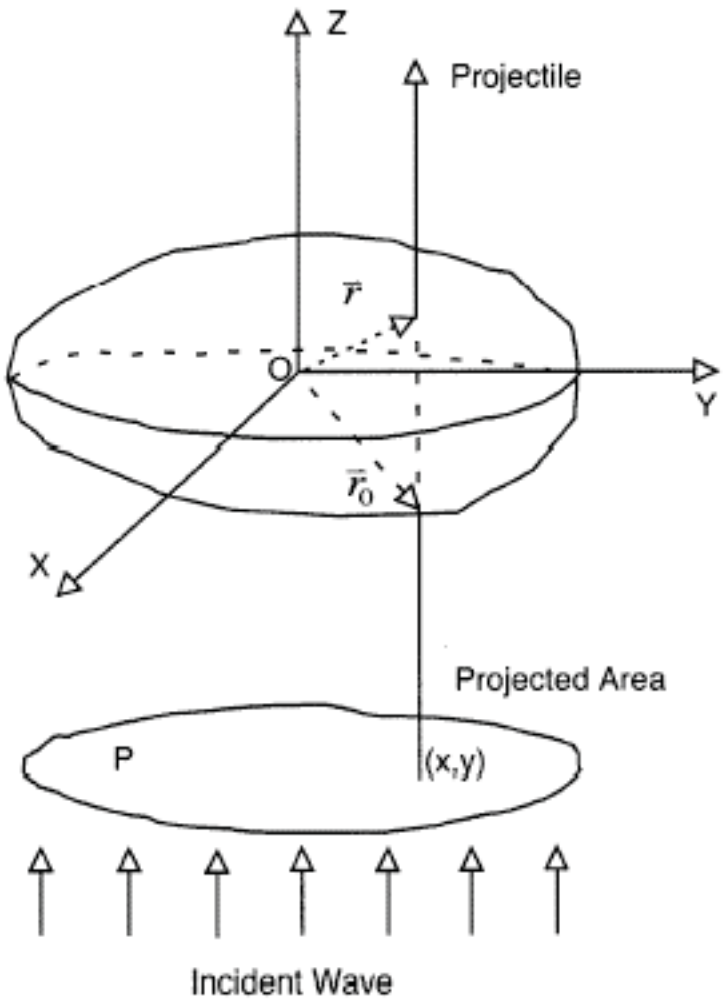

Fig. 12 Geometric configuration illustrating the principle of the anomalous diffraction theory.

Analytical solutions to Eqs. (3.1) and (3.2) can be obtained for a limited set of particle shapes such as spheres, spheroids, circulars, cylinders, cubes and hexagons. For more complicated geometries that are quite often found in nature, such as bullet rosette ice crystals in cirrus clouds,[69,93] it is likely that a numerical method has to be used to evaluate the integrals in Eqs. (3.1) and (3.2). Since the value of the extinction cross section is sensitive to the phase interference of the transmitted wave, a fine resolution grid must be used to resolve the variation of the projectile-length from its initial point (x,y) within the projected area of the particle on a plane normal to the incident direction. Thus, the projected area of the particle needs to be divided into an enormous number of projectiles for the case of a moderate or large size parameter. The integrals in Eqs. (3.1) and (3.2) are computed by discrete summations of the contributions from individual projectiles. This approach is not efficient computationally if multiple particle sizes and wavelengths are involved, particularly when random orientations are assumed for particles with sizes much larger than the incident wavelength. To overcome this issue, we start with the ADT formulation developed by Xu et al.[85] and Xu [86], which is given as follows:

$$C_{ext} = 2\,\mathrm{Re}\left\{P\int[1-e^{ikl(m-1)}f(l)]dl\right\}, \tag{3.4}$$

and

$$C_{abs} = P\int(1-e^{-2klm_i})f(l)dl, \tag{3.5}$$

where P is the projected area of the particle. The quantity $f(l)$ is interpreted by Xu et al.[85] and Xu[86] as the probability distribution function of the geometrical paths of rays inside the particle, since the anomalous diffraction extinction of light is viewed as a statistical process. The quantity $f(l)$ can also be thought of as the fraction of particle projected area when the projectile-length is between $l-dl/2$ and $l+dl/2$, since the extinction and absorption processes associated with Eqs. (3.1) and (3.2) are deterministic processes. It is interesting to note that the transform from Eqs. (3.1) and (3.2) to Eqs. (3.4) and (3.5) is similar to the transform from the line-by-line method to the k-distribution method developed for the computation of the mean gaseous transmittance for a given spectral interval.

The mean transmittance can be computed by integrating the monochromatic transmittance in the wavenumber domain, an approach known as the line-by-line method. Alternatively, it can be computed in the k (absorption coefficient) or cumulative k distribution (g) domain (i.e., the so-called k-distribution method). The absorption coefficient k is usually a rapidly oscillating function in the wavenumber domain whereas the absorption coefficient is a smooth function in the g domain. Thus, it requires much fewer quadrature points to calculate the spectral transmittance in the g domain than in the wavenumber domain. To adopt the methodology of the k-distribution method to improve the efficiency of ADT, Eqs. (3.4) and (3.5) are rewritten as follows:

$$C_{ext} = 2\,\mathrm{Re}\left\{P\int_0^1 \{1 - e^{ikl_{\max}\tilde{l}(m-1)} f(\tilde{l})\}d\tilde{l}\right\}$$

$$= 2P\int_0^1 \{1 - e^{-kl_{\max}\tilde{l}m_i}\cos[kl_{\max}\tilde{l}(m_r - 1)]\} f(\tilde{l})d\tilde{l}\,, \tag{3.6}$$

and

$$C_{abs} = P\int_0^1 (1 - e^{-2kl_{\max}\tilde{l}m_i}) f(\tilde{l})d\tilde{l}\,, \tag{3.7}$$

where $l_{\max}$ is the maximum projectile-length for a particle with a given orientation; $\tilde{l}$, the scaled projectile-length, is a dimensionless quantity, given by $\tilde{l} = l/l_{\max}$. For simplicity in the present formulation without losing generality, we assume that the minimum projectile-length ($l_{\min}$) is zero. In the case when the minimum projectile-length is nonzero, the lower integral-limit in Eqs. (3.6) and (3.7) should be $\tilde{l}_{\min} = l_{\min}/l_{\max}$. The quantity $f(\tilde{l})$ in Eqs. (3.6) and (3.7) is the fraction (percentage) of the projected area (P) when the projectile-length is between $l_{\max}(\tilde{l} - d\tilde{l}/2)$ and $l_{\max}(\tilde{l} + d\tilde{l}/2)$. Note that $f(\tilde{l})$ is normalized, that is, the following normalization condition holds:

$$\int_0^1 f(\tilde{l})d\tilde{l} = 1. \tag{3.8}$$

Furthermore, we define the cumulative fraction q associated with $f(\tilde{l})$ as follows:

$$q(\tilde{l}) = \int_0^{\tilde{l}} f(\tilde{l}\ )d\tilde{l}\quad, \tag{3.9a}$$

or,

$$dq = f(\tilde{l})d\tilde{l}\,. \tag{3.9b}$$

Because $f(\tilde{l})$ is a non-negative quantity, q defined by Eq. (3.9a) is a monotonically increasing function of $\tilde{l}$. Thus, there is a one-to-one mapping between $\tilde{l}$ and q for the range $\tilde{l} \in [0,1]$. By taking the inverse of the cumulative distribution function, we can express $\tilde{l}$ as a function of q, that is

$$\tilde{l}_q = \tilde{l}\,(q)\,, \tag{3.10}$$

where the subscript q indicates that the scaled projectile length is expressed in the q domain. From Eqs. (3.6), (3.9b) and (3.10), the extinction cross section in the ADT frame can thus be given as follows:

$$\begin{aligned} C_{ext} &= 2P\,\mathrm{Re}\left\{\int_0^1 [1 - e^{ikl_{\max}\tilde{l}_q(m-1)}]dq\right\} \\ &= 2P\int_0^1 \{1 - e^{-kl_{\max}\tilde{l}_q m_i}\cos[kl_{\max}\tilde{l}_q(m_r-1)]\}dq\,. \end{aligned} \tag{3.11}$$

Similarly, for the absorption cross section, we have

$$C_{abs} = P\int_0^1 e^{-2kl_{\max}\tilde{l}_q m_i}\,dq\,. \tag{3.12}$$

The extinction and absorption efficiencies corresponding to Eqs. (3.11) and (3.12) are given by

$$Q_{ext} = C_{ext}/P = 2\int_0^1 [1 - e^{-kl_{\max}\tilde{l}_q m_i}\cos kl_{\max}\tilde{l}_q(m_r-1)]dq\,, \tag{3.13}$$

and

$$Q = C_{abs}/P = \int_0^1 e^{-2kl_{\max}\tilde{l}_q m_i}\,dq\,. \tag{3.14}$$

Note that Eqs. (3.11)-(3.14) are general expressions without being limited to a specific geometry. Furthermore, the scaled projectile-length in the q domain is independent of the particle physical size (e.g., $\tilde{l}_q$ is the same for a sphere with a radius of 100 μm as for one with a radius of 5 μm). This feature implies that the computational effort can be reduced substantially if a range of particle sizes is involved. For a given geometry, the key computational effort in the present method is to derive the scaled projectile-length in the q domain, which is defined by Eq.(3.10). As the simplest example, Fig. 13 illustrates how to obtain $\tilde{l}_q$ in the case for a sphere. The maximum projectile-length for a sphere is

$$l_{\max} = 2R, \tag{3.15}$$

where R is the radius of the sphere. From the geometric configuration shown in Fig. 13, we have

$$l = 2R\cos\eta = l_{\max}\cos\eta. \tag{3.16}$$

The corresponding scaled projectile-length is given by

$$\tilde{l} = l / l_{\max} = \cos\eta. \tag{3.17}$$

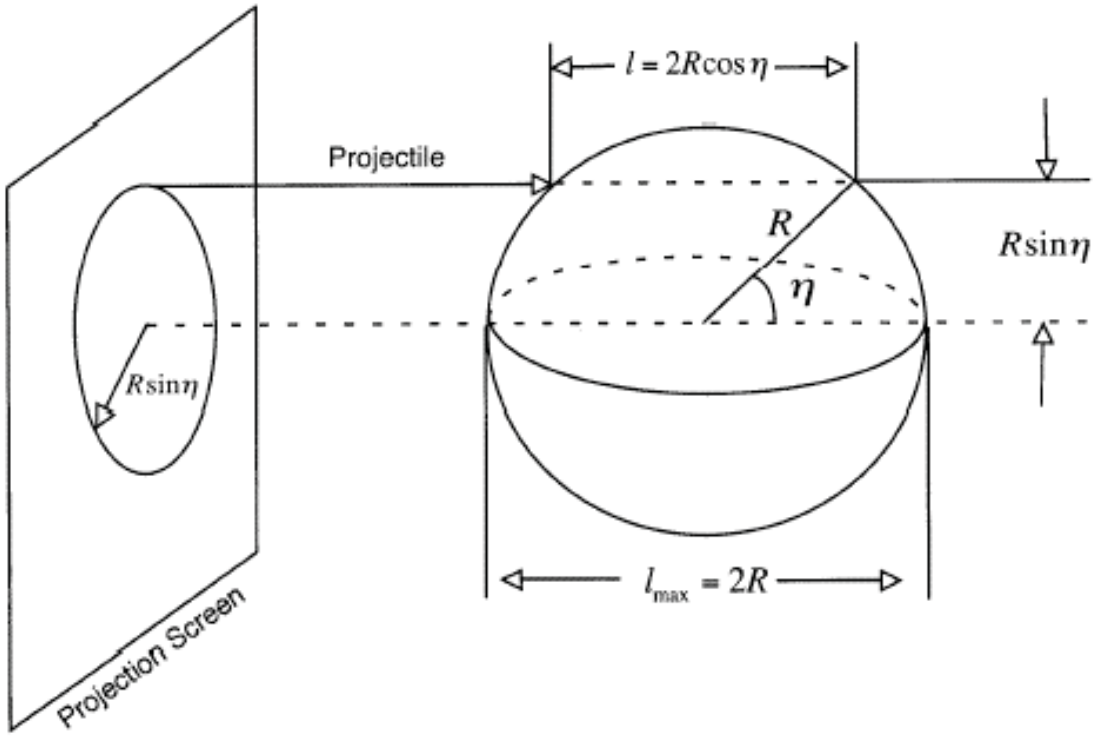

Fig. 13 Geometry for deriving the distribution function of particle projected area as a function of the projectile –length.

The fraction of the projected area, when the projectile-length is between $l_{\max}$ and l, is given by

$$A = \pi R^2 \sin^2 \eta = \pi R^2 (1 - \tilde{l}^2). \tag{3.18}$$

According to the physical meaning of $f(\tilde{l})$, we have

$$f(\tilde{l}) = \left| \frac{1}{\pi R^2} \frac{dA}{d\tilde{l}} \right| = 2\tilde{l}. \tag{3.19}$$

The corresponding cumulative fraction of the projected area, q, is given by

$$q(\tilde{l}) = \int_0^{\tilde{l}} f(\tilde{l}') d\tilde{l}' = \tilde{l}^2. \tag{3.20}$$

From Eqs. (3.17) and (3.20), q is in the range of [0,1] because of $\tilde{l} \in [0,1]$. The projectile-length in the q domain is given by

$$\tilde{l}_q = q^{1/2}. \tag{3.21}$$

It can be seen that the scaled projectile-length $\tilde{l}_q$ is independent of the physical size of a sphere. The ADT solutions to the extinction and absorption cross sections of a sphere in the q domain are given as follows:

$$C_{ext} = 2P \operatorname{Re}\left\{ \int_0^1 \{1 - \exp[ikl_{\max} q^{1/2}(m-1)]\} dq \right\}, \tag{3.22}$$

and

$$C_{abs} = P \int_0^1 [1 - \exp(-2kl_{\max} q^{1/2} m_i)] dq. \tag{3.23}$$

To show the equivalence of the preceding expressions to those given by the conventional ADT, let $q = \sin^2 \xi$ and $w = -ikl_{\max}(m-1)$. The integral in Eq. (3.22) then reduces to the following form

$$\begin{aligned} C_{ext} &= 4P \operatorname{Re}\left\{ \int_0^{\frac{\pi}{2}} \left(1 - e^{-w \sin \xi}\right) \cos \xi \sin \xi d\xi \right\} \\ &= 4P \operatorname{Re}\left(\frac{1}{2} + \frac{e^{-w}}{w} + \frac{e^{-w} - 1}{w^2} \right). \end{aligned} \tag{3.24}$$

The result given by Eq. (3.24) is exactly the same as the form given by van de Hulst[3]. Similarly, the absorption cross section can be expressed as follows:

$$C_{abs} = 2P\int_0^{\frac{\pi}{2}}\left(1-e^{-u\ \sin\xi}\right)\cos\xi\sin\xi d\xi$$

$$= 2P\left(\frac{1}{2}+\frac{e^{-u}}{u}+\frac{e^{-u}\ -1}{u^{\ 2}}\right), \tag{3.25}$$

where $u\ = 2kl_{\max}m_i$. Again, in the computation of the absorption cross section, the present formulation is equivalent to its conventional ADT counterpart.

Figure 14 illustrates the computation of $f(\tilde{l})$ and $\tilde{l}_q$ in a case for a hexagonal geometry that is quite interesting to atmospheric research because pristine ice crystals often possess hexagonal structures. Figures 14a and 14b show the orientation of the particle relative to the incident projectiles. The incident direction is perpendicular to the symmetry-axis of the particle and faces the broad side of the particle's cross section. Thus, the ADT configuration associated with Figs. 14a and 14b actually reduces to a 2-D case. It is evident from Fig. 14b that the maximum projectile-length is $l_{\max} = \sqrt{3}a$ in which a is the semi-width of the particle's cross section. The ratio of the area associated with $l_{\max}$ (i.e., the case when a projectile passes through two faces that are parallel to each other) to the total projected area is 50%. The other half of the projected area corresponds to $\tilde{l} \in [0,1)$, a region that excludes the point $\tilde{l} = 1$. Thus, the exact solution for $f(\tilde{l})$ is given as follows:

$$f(\tilde{l}) = \frac{1}{2}+\frac{1}{2}\delta(\tilde{l}-1), \tag{3.26}$$

where δ is the Dirac delta function. From Eqs. (3.9a), (3.10) and (3.26), the scaled projectile-length in the q domain can be given in the form of

$$\tilde{l}_q = \begin{cases} 2q, & for\ 0 \le q \le 0.5, \\ 1, & for\quad q > 0.5. \end{cases} \tag{3.27}$$

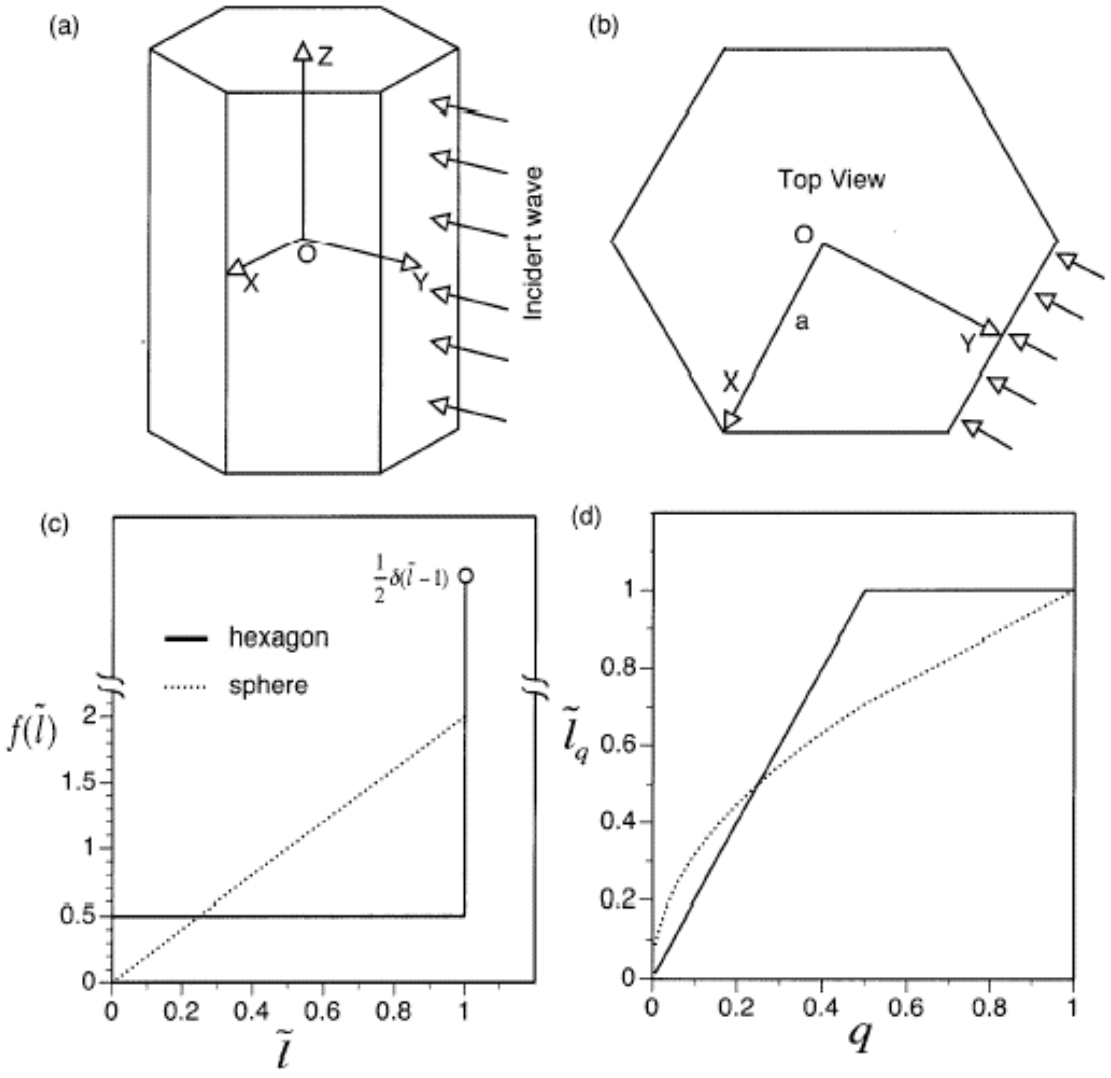

Fig. 14 (a) and (b): the incident configuration for the ADT computation in a case for a specifically oriented hexagon; (c): projected-area distribution function, $f(\tilde{l})$, for a sphere and a hexagon whose orientation is specified in (a) and (b); (d): scaled projectile-length associated with $f(\tilde{l})$ in (c).

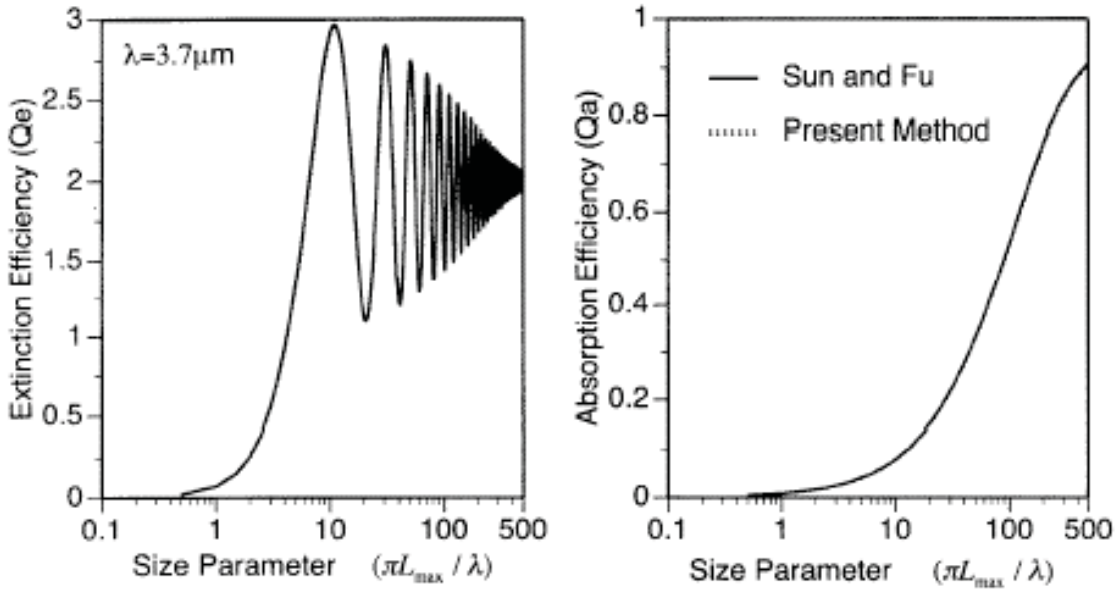

Fig. 15 Comparison of extinction and absorption efficiencies (Q_{ext} and Q_{abs}) computed from the present ADT method in the q domain and from an analytical ADT solution reported by Sun and Fu.

Figure 14c and 14d show $f(\tilde{l})$ and $\tilde{l}_q$ given by Eqs. (3.26) and (3.27), respectively, which are compared with their spherical counterparts. The effect of particle geometry on the distribution of projectile-length is pronounced. As explained in the previous discussion, $f(\tilde{l})$ and $\tilde{l}_q$ are independent of particle physical size. Thus, it is not proper to approximate a nonspherical particle with a specific orientation using a sphere regardless of the definition of "spherical equivalence" (i.e., how a spherical radius is specified for the "equivalence") in the computation of the extinction and absorption cross sections in the ADT frame.

Results from the present ADT algorithm for the case for a nonspherical particle, specifically for a hexagonal ice crystal with the incident configuration shown in Fig.14, can be compared to the analytical ADT solution derived by Sun and Fu.[80] The results are shown in Fig. 15 for the extinction and absorption cross sections computed at a wavelength of 3.7 μm. The refractive index of ice[68] at

this wavelength is $m = 1.4 + 0.0072i$. The two results are exactly the same, as is evident from Fig. 15 in which the solid and dotted lines are overlapped.

For an arbitrary nonspherical geometry, it is unlikely to obtain an analytical expression for $f(\tilde{l})$ or $\tilde{l}_q$. In this case, a numerical approach has to be used. Specially, a rectangular area that bounds the projectile projection on a plane normal to the incident direction is divided into a number of small area elements (uniform square area elements in practice). Then it is determined whether the projectiles associated with the small area elements interact with the particle. A projectile is disregarded in the numerical computation if it does not strike the scattering particle; that is, only those projectiles impinging on the particle are accounted for. We divide the range $[0,1]$ into n uniform intervals for $\tilde{l}$; that is, the width of the interval is given by $\Delta\tilde{l} = 1/n$. The projectile-lengths of all the projectiles that impinge on the particle are calculated sequentially. Let the number of the projectiles whose lengths within the particle are between $(j-1)\Delta\tilde{l}$ and $j\Delta\tilde{l}$ be N_j. Thus, we have

$$f[(j-1/2)\Delta\tilde{l}] = \frac{N_j}{\Delta\tilde{l}\sum_{i=1}^{n} N_i}. \tag{3.28}$$

The corresponding cumulative projected area distribution function q is given by

$$q_j = q[j\Delta\tilde{l}] = \sum_{k=1}^{j} \Delta\tilde{l} f[(k-1/2)\Delta\tilde{l}] = \frac{\sum_{k=1}^{j} N_k}{\sum_{i=1}^{n} N_i}. \tag{3.29}$$

From Eq. (3.29), the numerical pairs of $(\tilde{l}_j, q_j)$ with $\tilde{l}_j = j\Delta\tilde{l}$ are obtained; i.e., the dimensionless scaled projectile-length in the q domain is obtained, as $\tilde{l}_j$ can be regarded as a discrete value of the function $\tilde{l}(q)$ at $q = q_j$.

Consider an ensemble of nonspherical particles that are randomly oriented in space. As shown in Fig.16, the orientation of a nonspherical particle relative to the laboratory coordinate system, *oxyz*, can be

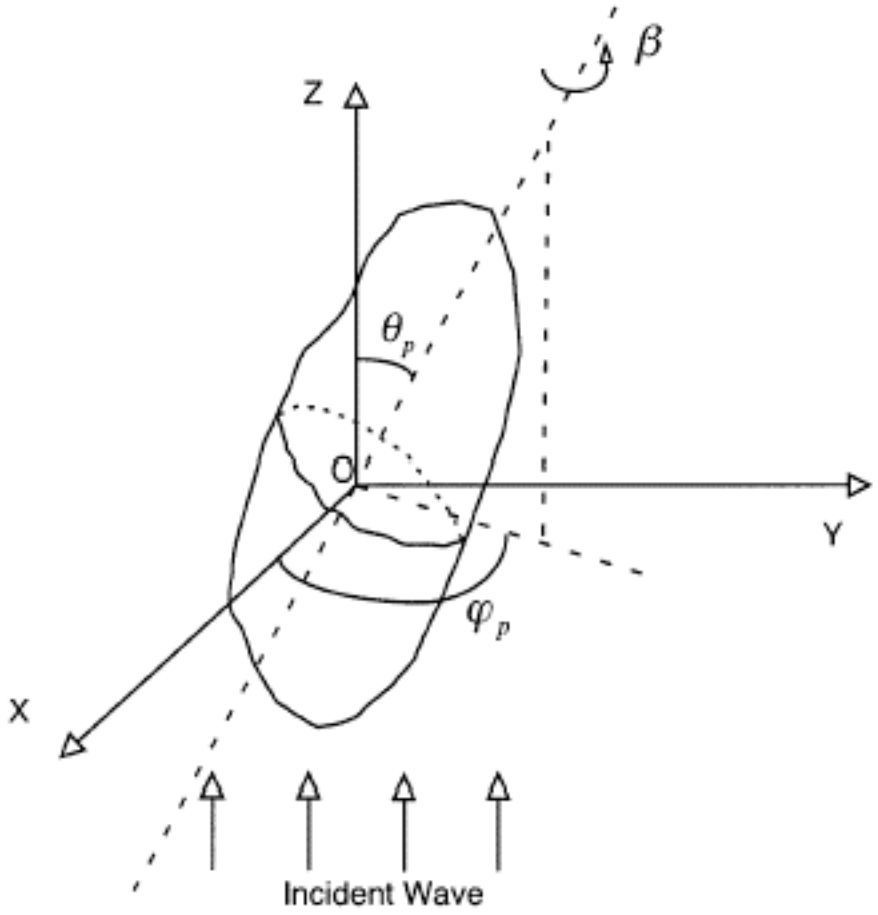

Fig. 16 Conceptual diagram showing the orientation of a nonspherical particle with respect to the incident direction.

specified in terms of three angles: θ_p, φ_p and β. The extinction and absorption cross sections in the ADT frame for a specific orientation of the particle depend on angles θ_p and β (note that in a rigorous scattering theory the extinction and absorption cross sections also depend on the polarization configuration of the incident wave, i.e., the φ_p-dependence is involved). In the conventional ADT algorithm, the ensemble-averaged (or orientation-averaged) extinction cross section is given as follows:

$$< C_{ext} >= 2(4\pi)^{-1}\,\mathrm{Re}\left\{\int_0^{2\pi}\int_0^{\pi}\iint_P [1-e^{ikl(m-1)}]dx_p dy_p \sin\theta_p d\theta_p d\beta\right\}, \tag{3.30}$$

where the integration over $dx_p dy_p$ is carried out over the particle projected area. The preceding expression is inefficient computationally since a 4-order integral is involved. Moreover, integration has to be repeated if various particle sizes are considered for multiple spectral wavelengths. With the approach based on the distribution of projectile-length, the extinction cross section given by Eq. (3.30) can be rewritten as follows:

$$< C_{ext} >= 2(4\pi)^{-1}\,\mathrm{Re}\left\{\int_0^{2\pi}\int_0^{\pi} P(\theta_P,\beta)\int_0^1 [1-e^{ikl_{\max}(\theta_p,\beta)\tilde{l}(m-1)}]f(\tilde{l})d\tilde{l}\sin\theta_p d\theta_p d\beta\right\}, \tag{3.31}$$

where $l_{\max}(\theta_p,\beta)$ is the maximum projectile-length for a specific particle orientation associated with angles θ_p and β (see Fig. 16).

In the case for randomly orientated particles, we define the maximum projectile-length for an ensemble of the particles as follows:

$$L_{\max} = \max[l_{\max}(\theta_p,\beta)] \text{ for } \theta_p \in [0,\pi] \text{ and } \beta \in [0,2\pi]. \tag{3.32}$$

The dimensionless scaled projectile-length for the ensemble is:

$$\tilde{L} = l_{\max}(\theta_p,\beta)\tilde{l}\,/L_{\max}. \tag{3.33}$$

The projectile-length distribution, $f(\tilde{l})$, averaged over particle orientations, is given by

$$\overline{f}(\tilde{L}) = (4\pi\overline{P})^{-1}\int_0^{2\pi}\int_0^{\pi} P(\theta_p,\beta)f(\tilde{L})\varsigma[l_{\max}(\theta_p,\beta)/L_{\max}-\tilde{L}]\sin\theta_p d\theta_p d\beta, \tag{3.34}$$

where $\overline{P}$ is the ensemble-averaged projected area, given by

$$\overline{P} = (4\pi)^{-1}\int_0^{2\pi}\int_0^{\pi} P(\theta_p,\beta)\sin\theta_p d\theta_p d\beta. \tag{3.35}$$

For a convex geometry, $\overline{P}$ is, $S/4$ in which S is the surface area of the geometry[94]. The function ς in Eq. (3.34) is a step function, given by

$$\varsigma(x) = \begin{cases} 0, & for\ x < 0, \\ 1, & for\ x \geq 0. \end{cases} \tag{3.36}$$

Given $\overline{f}(\tilde{l})$, Eq. (3.31) can now be rewritten as follows:

$$< C_{ext} >= 2\overline{P}\,\mathrm{Re}\left\{\int_0^1 [1-e^{ikL_{\max}\tilde{L}(m-1)}]\overline{f}(\tilde{L})d\tilde{L}\right\}$$

$$= 2\overline{P}\int_0^1 \{1 - e^{-kL_{\max}\tilde{L}m_i}\cos[kL_{\max}\tilde{L}(m_r - 1)]\}\overline{f}(\tilde{L})d\tilde{L}. \quad (3.37)$$

Eq. (3.37) is quite similar to Eq. (3.6) except that the latter is for the extinction cross section of a particle with a specific orientation. From Eq. (3.37), we can define the cumulative percentage $\overline{q}$ for the ensemble of the randomly orientated particles as follows:

$$\overline{q}(\tilde{L}) = \int_0^{\tilde{L}} \overline{f}(\tilde{L}\ )d\tilde{L}\ . \quad (3.38)$$

The cumulative percentage $\overline{q}$ is a monotonic function of $\tilde{L}$. Thus, we can express the scaled projectile-length in the $\overline{q}$ domain as follows:

$$\tilde{L}_{\overline{q}} = \tilde{L}(\overline{q}). \quad (3.39)$$

Note that $\tilde{L}_{\overline{q}}$ is independent of the physical sizes of the particles in the ensemble as long as the relative size ratio (i.e., the ratio of the size of one particle to another) and morphological shape of the particles remains the same. Based on Eqs. (3.38) and (3.39), the extinction and absorption cross sections, after averaging over the ensemble of the particles, are given by:

$$< C_{ext} >= 2\,\mathrm{Re}\left\{\overline{P}\int_0^1 [1 - e^{ikL_{\max}\tilde{L}_{\overline{q}}(m-1)}]d\overline{q}\right\}$$

$$= 2\overline{P}\int_0^1 \{1 - e^{-kL_{\max}\tilde{L}_{\overline{q}}m_i}\cos[kL_{\max}\tilde{L}_{\overline{q}}(m_r - 1)]\}d\overline{q}, \quad (3.40)$$

and

$$< C_{abs} >= \overline{P}\int_0^1 [1 - e^{-2kL_{\max}\tilde{L}_{\overline{q}}m_i}]d\overline{q}. \quad (3.41)$$

The particle orientation information is required only in the computation of $\tilde{L}_{\overline{q}}$. The size independent property of $\tilde{L}_{\overline{q}}$ largely improves the ADT efficiency if various particle sizes are involved.

Figure 17a shows the scaled projectile-length, $\tilde{L}_{\overline{q}}$, of hexagonal particles with various values of aspect ratio (aspect ratio is defined as $H/2a$ in which H is the length of the particle symmetry

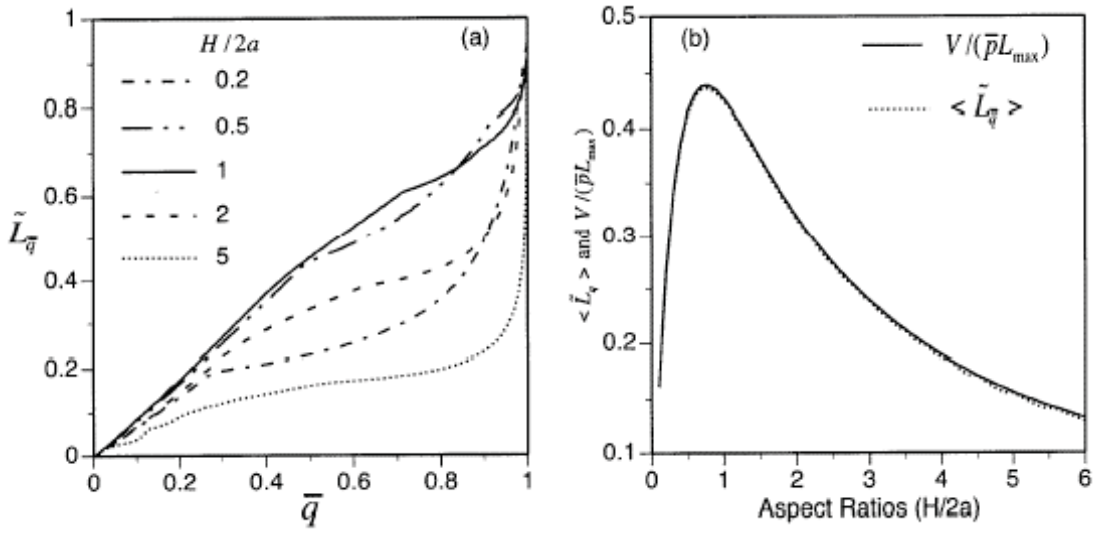

Fig. 17 (a) dimensionless scaled projectile-length $\tilde{L}_{\bar{q}}$ for hexagons with various values of aspect ratios ($H/2a$); (b): the mean value of $\tilde{L}_{\bar{q}}$ and $V/(\bar{P}L_{\max})$.

axis and a is the semi-width of a particle cross section). It is evident from Fig. 17a that $\tilde{L}_{\bar{q}}$ is quite sensitive to the particle aspect ratio. For a given $\tilde{L}_{\bar{q}}$, the mean scaled projectile-length is given by

$$< \tilde{L}_{\bar{q}} >= \int_0^1 \tilde{L}_{\bar{q}} d\bar{q}. \tag{3.42}$$

Figure 17b shows the mean scaled projectile-length corresponding to the results shown in Fig.17a where the ratio $V/(\bar{P}L_{\max})$ is also shown. An interesting point to note is that $< \tilde{L}_{\bar{q}} >= V/(\bar{P}L_{\max})$. For example, the mean value of the scaled projectile-length of the hexagonal column with an aspect ratio 2.0, calculated from Eq.(3.42), is 0.32, which is exactly the value of $V/(\bar{P}L_{\max})$. This feature can be understood via the following relationship:

$$< \tilde{L}_{\bar{q}} >= \int_0^1 \tilde{L}_{\bar{q}} d\bar{q} = \int_0^1 \tilde{L} f(\tilde{L}) d\tilde{L} = \frac{\iint_P L dp}{\bar{P}L_{\max}} = \frac{V}{\bar{P}L_{\max}}. \tag{3.43}$$

Another interesting feature shown in Fig. 17(b) is that $< \widetilde{L}_{\bar{q}} >$ as a function of the aspect ratio reaches its maximum when $H/2a$ (i.e., compact hexagonal particles). Bryant and Latimer[95] developed a simplified version of ADT for randomly orientated particles. They suggested that, in the ADT framework, a randomly orientated particle with a volume V and a projected area $\overline{P}$ can be converted to a cylinder with a thickness of $d_e = V/\overline{P}$ with an incidence normal to the cross section of the cylinder. From the present $\overline{q}$ domain ADT formulation, the projectile-length distribution can be approximated by the following equation:

$$\overline{f}(\tilde{L}) = \delta(\tilde{L} - V/\overline{P}/L_{\max}), \tag{3.44}$$

where δ is the Dirac delta function. Thus, we have

$$\begin{aligned} < C_{ext} >= 2\overline{P}\,\mathrm{Re}\left\{\int_0^1 [1 - e^{ikL_{\max}\tilde{L}(m-1)}]\overline{f}(\tilde{L})d\tilde{L}\right\} \\ = 2\overline{P}\,\mathrm{Re}\left\{\int_0^1 [1 - e^{ikL_{\max}\tilde{L}(m-1)}]\delta(\tilde{L} - V/\overline{P}/L_{\max})d\tilde{L}\right\} \\ = 2\overline{P}\{1 - e^{-kd_e m_i}\cos[kd_e(m_r - 1)]\}, \end{aligned} \tag{3.45}$$

where d_e is often referred to as the effective size, given by $d_e = V/\overline{P}$. Sun and Fu[81] have shown that the simplified ADT may introduce substantial errors for hexagonal ice crystals.

Figure 18 shows the extinction and absorption efficiencies of the hexagonal ice crystals with various aspect ratios at a wavelength of $\lambda = 3.7\mu m$ as the functions of size parameter $\pi L_{\max}/\lambda$. Here $L_{\max} = (H^2 + 4a^2)^{1/2}$, where H is the length of the symmetry axis of the particle and a is the semi-width of the particle cross section. Because $\overline{f}(\tilde{l})$ is sensitive to the particle aspect ratio, Q_{ext} and Q_{abs} are quite different for the different values of $H/2a$. The left panel of Fig.18 shows the efficiencies of hexagonal ice crystals with various aspect ratios. For a given size parameter ($\pi L_{\max}/\lambda$), the absorption efficiency of compact hexagonal ice crystals (i.e., $H/2a = 1$) is maximum, as is evident from the right panel of Fig.18. This occurs because $< \tilde{L}_{\bar{q}} >$ reaches its maximum values when $H/2a = 1$, as shown in Fig. 17b.

As an example of applying the present ADT formulation to complex particle geometries, Fig.19 shows the extinction and absorption efficiencies of the bullet rosette ice crystals with various branches at a wavelength of $\lambda = 3.7\mu m$ as a function of size parameter $2\pi r / \lambda$ in which r is the diameter of the volume-equivalent sphere. The sensitivity of Q_{ext} and Q_{abs} to the number of bullets is evident. In particular, the absorption efficiency decreases with the increase of branch number although the size parameters in Fig. 19 are defined on the basis of volume-equivalence.

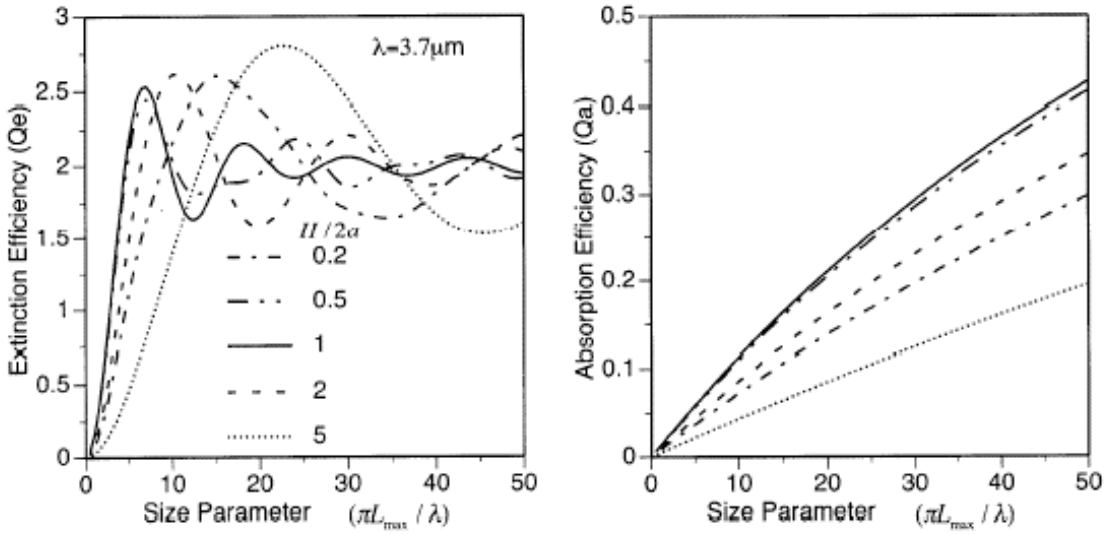

Fig. 18 (a) Extinction efficiencies of hexagons with various aspect ratios; (b): absorption efficiencies corresponding to Q_{ext} showed in (a).

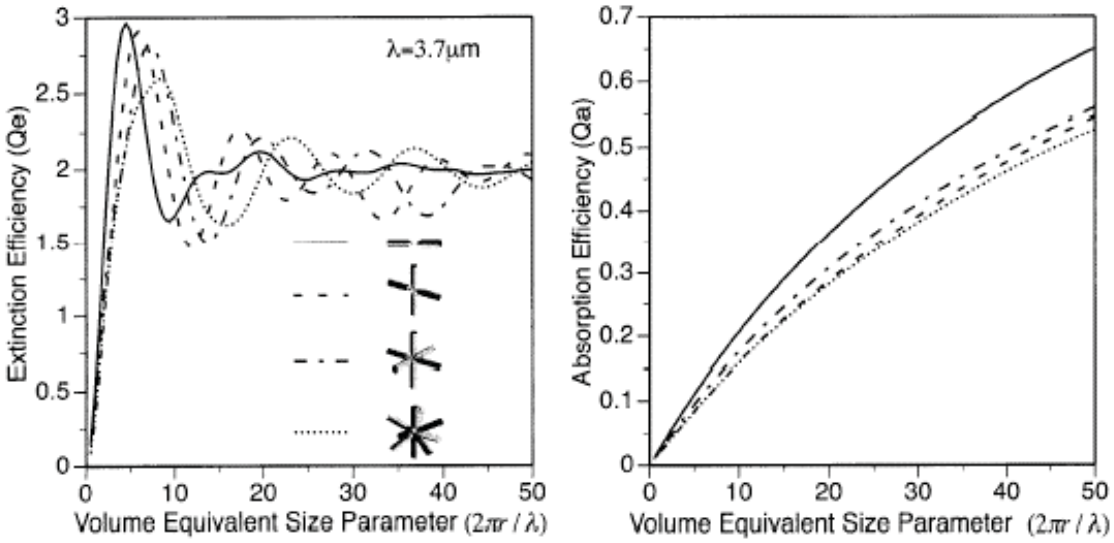

Fig. 19 Extinction and absorption efficiencies of bullet rosettes with various branches.

Modified ADT Formulation

The essence of ADT is that the amplitude and polarization of the electromagnetic waves inside an optically tenuous scattering particle is the same as those of the incident wave. Given the geometry shown in Fig. 12, the internal electric field can be expressed as follows:

$$\vec{E}(\vec{r}) = \vec{E}_o \exp(ik\hat{z}\cdot\vec{r}_o)\exp[ikm\hat{z}\cdot(\vec{r}-\vec{r}_o)]. \tag{3.46}$$

where $\vec{E}_o$ is the amplitude of the incident electric field, and $\vec{r}_o$ is the position vector of the incident point. From the basic physical principles associated with classic electromagnetic scattering (e.g., Mishchenko et al.[96], Bohren and Huffman[5] and references cited therein), the extinction and absorption cross sections can be expressed exactly as follows:

$$C_{ext} = \mathrm{Im}\left[\frac{k}{E_o E_o^*}(m^2-1)\iiint_v \vec{E}(\vec{r}')\cdot\vec{E}_o^*(\vec{r}')d^3r'\right], \tag{3.47}$$

and

$$C_{abs} = \frac{k}{E_o E_o^*}2m_r m_i \iiint_v \vec{E}(\vec{r}')\cdot\vec{E}_o^*(\vec{r}')d^3r', \tag{3.48}$$

where the asterisk denotes the complex conjugate. Using Eq.(3.46) and integrating the field along projectiles, Eqs.(3.47) and (3.48) reduce to

$$C_{ext} = \mathrm{Re}\left\{(m+1)\iint_P [1-e^{ikl(m-1)}]dp\right\}, \tag{3.49}$$

and

$$C_{abs} = m_r \iint_P (1-e^{-2klm_i})dp. \tag{3.50}$$

The preceding expressions for the extinction and absorption cross sections are quite similar to the conventional ADT solutions. In fact, when the refractive index of the particle is close to 1 (i.e., $(m+1)\to 2$ and $m_r \to 1$), the conventional ADT solutions and those given by Eqs. (3.49) and (3.50) are essentially the same. However, we note that the extinction efficiently corresponding to Eq. (3.49) approaches an asymptotic value of $(m+1)$ when the scattering particle is large and strongly absorptive. This is in conflict with the physically correct solution (i.e., an asymptotic solution of 2). The fundamental mechanism for this inaccuracy is that the assumption given by Eq. (3.46) introduces greater errors for large particles than for

small particles. For a small particle, the induced field due to the existence of the particle is weak in comparison with the incident field and Eq. (3.46) is a good approximation in this case. To overcome this shortcoming in the modified ADT, we rewrite Eqs.(3.49) and (3.50) as follows:

$$C_{ext} = \mathrm{Re}\left\{2\iint_p [1-e^{-ikl(m-1)}]dP + (m-1)\iint_p [1-e^{-ikl(m-1)}]dP\right\}. \tag{3.51}$$

and

$$C_{abs} = \iint_p (1-e^{-2klm_i})dP + (m_r-1)\iint_p (1-e^{-2klm_i})dP. \tag{3.52}$$

The first terms on the right-hand sides of Eqs. (3.51) and (3.52) correspond to the standard ADT solutions, whereas the second terms are associated with errors caused by the approximation for the internal field by Eq.(3.46) as applied to Eqs. (3.49) and (3.50). To ensure that the solutions given by Eqs. (3.51) and (3.52) approach their physically correct asymptotic values, we need to add artificial diffusion terms in Eqs. (3.51) and (3.52) in the form of:

$$C_{ext} = \mathrm{Re}\left\{2\iint_p [1-e^{-ikl(m-1)}]dP + e^{-\varepsilon_1 V/\overline{P}}(m-1)\iint_p [1-e^{-ikl(m-1)}]dP\right\}, \tag{3.53}$$

and

$$C_{abs} = \iint_p (1-e^{-2klm_i})dP + e^{-\varepsilon_2 V/\overline{P}}(m_r-1)\iint_p (1-e^{-2klm_i})dP, \tag{3.54}$$

where V and $\overline{P}$ are the particle volume and the oriented averaged projected-area, respectively. The constants ε_1 and ε_2 in Eqs. (3.53) and (3.54) are two tuning factors, which can be determined from a comparison of Eqs. (3.53) and (3.54) with the corresponding Lorenz-Mie solutions. The values of ε_1 and ε_2 determined in the spherical case can be used as surrogates for nonspherical particles.

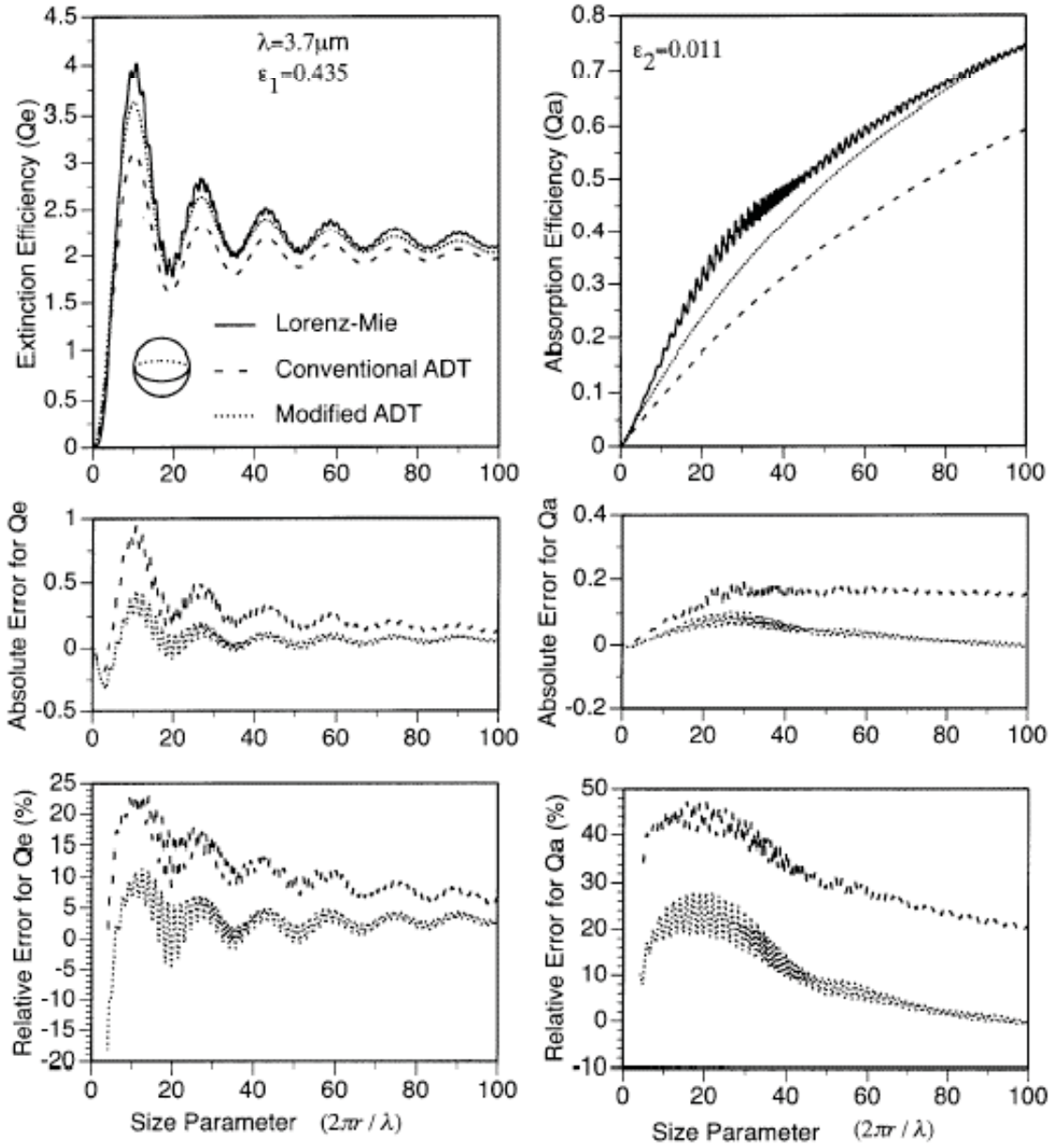

Fig. 20 Extinction and absorption efficiencies of spheres computed for the Lorenz-Mie theory, the conventional ADT, and the modified ADT at a wavelength of 3.7 μm.

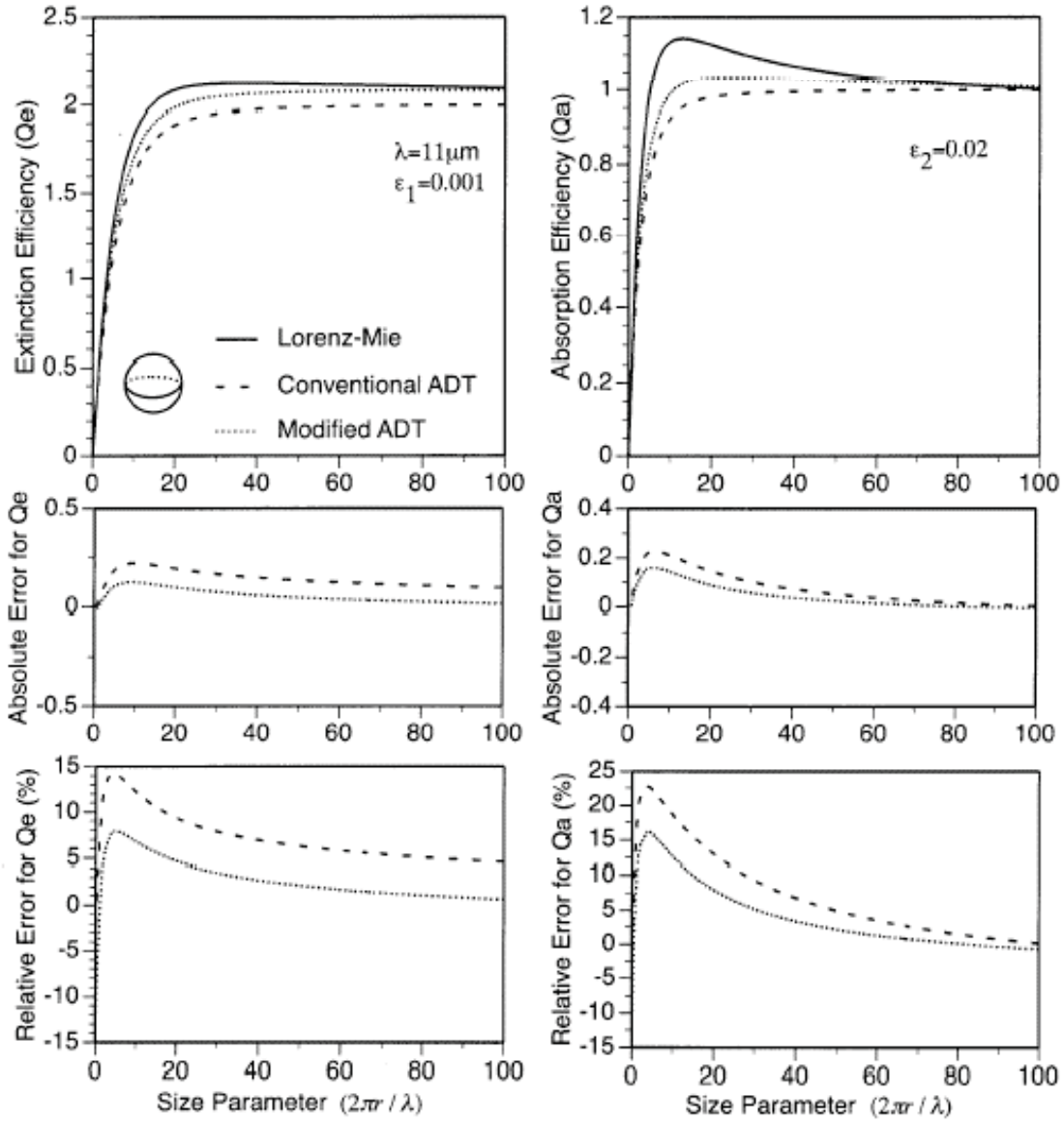

Fig. 21 Same as Fig. 20 except for a wavelength of 11 μm and different tuning factors.

Figure 20 shows the comparison of the values of Q_{ext} and Q_{abs} computed from the Lorenz-Mie theory, the conventional ADT, and the modified ADT. The best fitting values for ε_1 and ε_2 are 0.0435 and 0.011. The absolute and relative error between the ADT method and the exact solutions are defined as follows:

$$Error_{absolute} = \frac{Q_{exact} - Q_{ADT}}{Q_{exact}}, \tag{3.55}$$

and

$$Error_{relative} = \frac{Q_{exact} - Q_{ADT}}{Q_{exact}} \times 100\%, \tag{3.56}$$

where Q_{exact} represents the Lorenz-Mie solution for the extinction (or absorption) efficiency, and Q_{ADT} represents the corresponding solution from the conventional ADT method or the present modified ADT method. It is evident from Fig. 20 that both absolute and relative errors computed from the present method are much smaller than their conventional counterparts. Note that the absolute error of the modified ADT for Q_{exact} can be slightly larger than that for the conventional ADT when the size parameter is less than 5.

Figure 21 is similar to Fig. 20 except for a wavelength of 11 μm. The refractive index for the ice at this wavelength is $1.0925 + 0.248i$. Again, it is evident that the modified ADT solution is much more accurate than the conventional ADT results, if the two tuning factors ε_1 and ε_2 are properly selected.

For general nonspherical particles, the tuning factors cannot be known. However, we can use the tuning factors determined for spheres as surrogates for nonspherical particles. To validate this approach, we apply the tuning factors determined for spheres to the case for circular cylinders. Figures 22 and 23 show the comparisons of the T-matrix solutions[39], the modified ADT solutions, and the conventional ADT results. The improvement associated with the modified ADT method is evident from both Figs. 22 and 23.

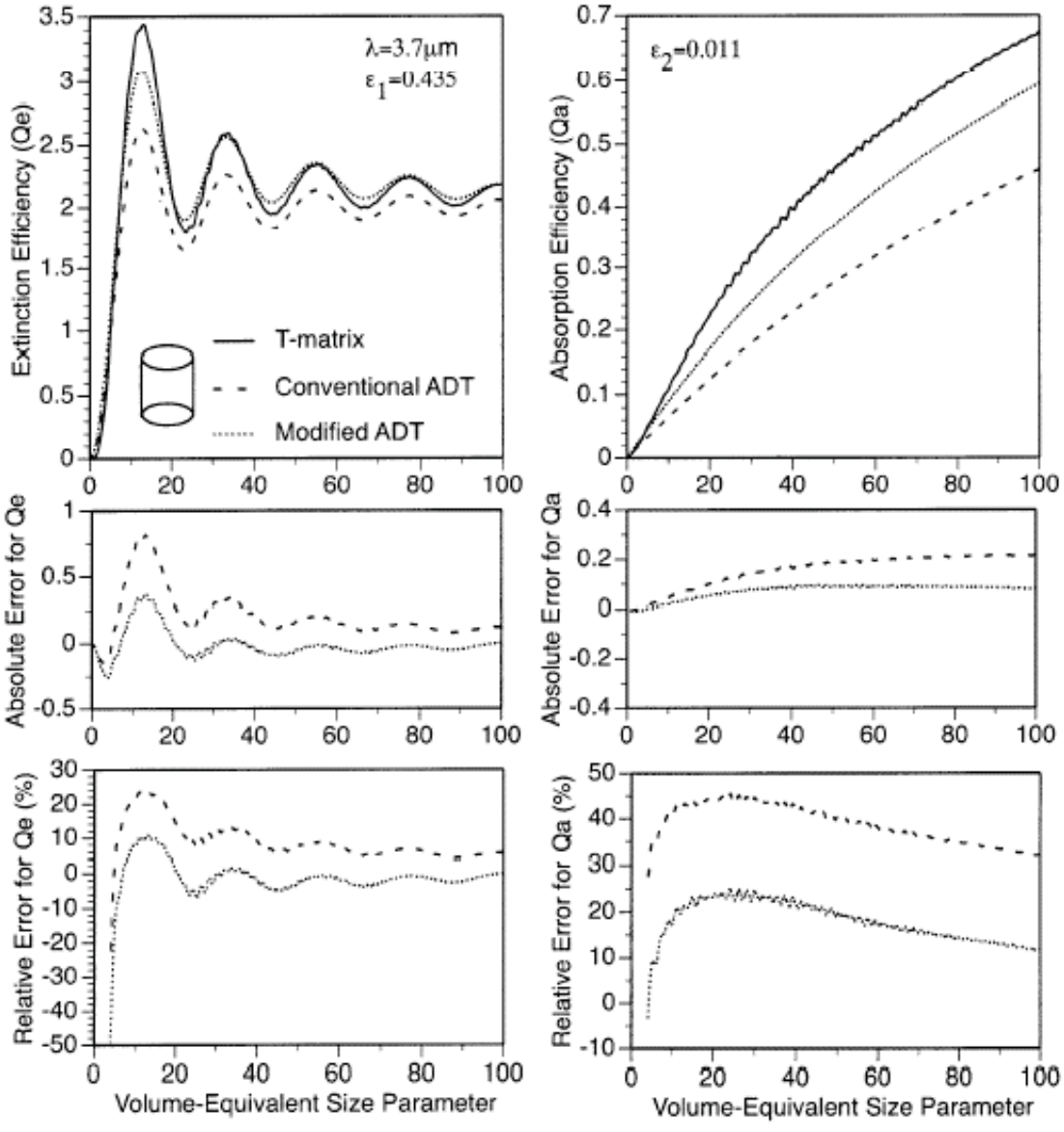

Fig. 22 Extinction and absorption efficiencies computed from the T-matrix method and the conventional ADT, and the modified ADT at a wavelength of 3.7 μm. Note that in the modified ADT the tuning factors are same as those shown in Fig. 20 for spheres.

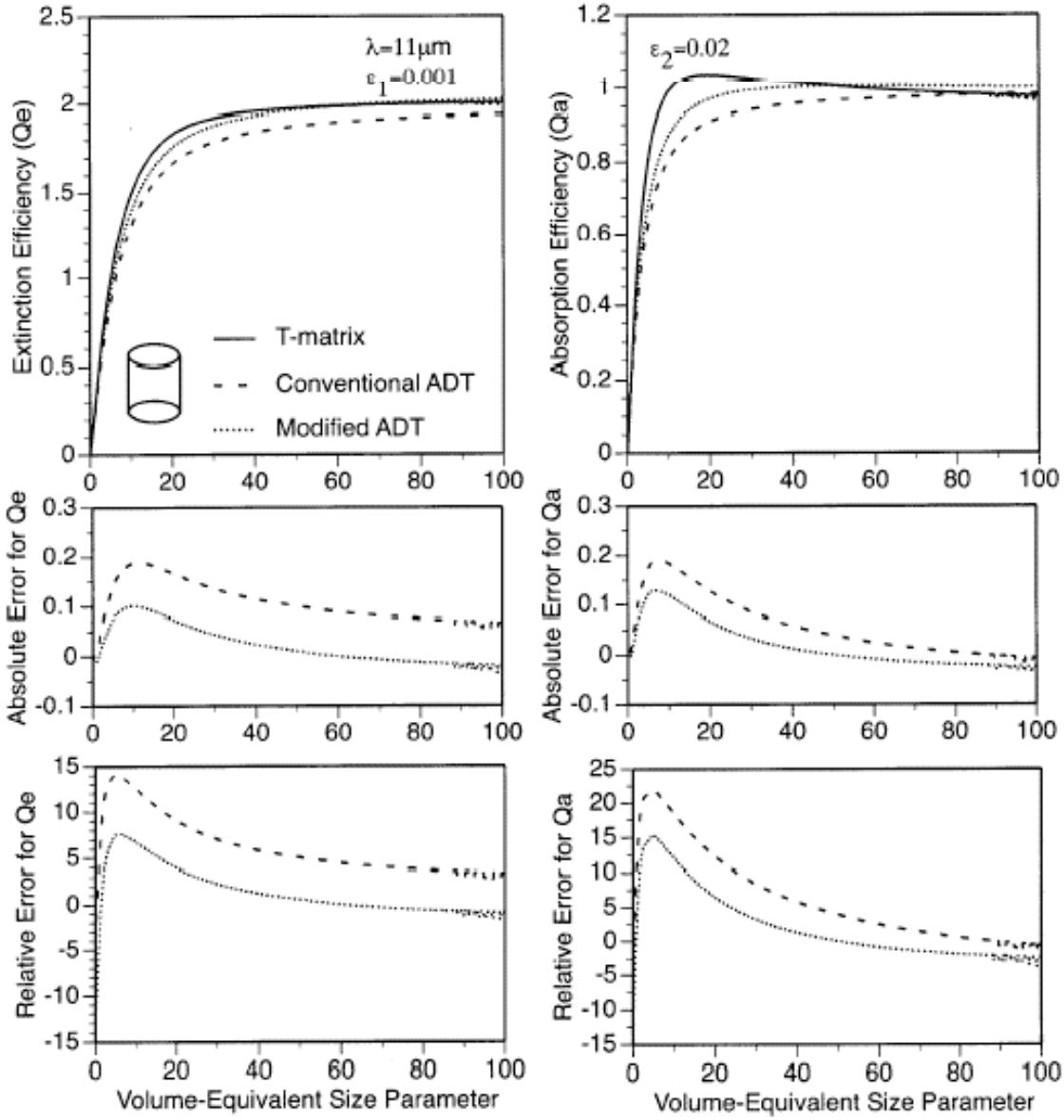

Fig. 23 Same as Fig. 22 except for a wavelength of 11 μm and tuning factors shown in Fig 21.

Summary and Conclusions

Recently, Xu et al.[85] and Xu[86] reformulated the conventional ADT by introducing the probability distribution function of the geometric paths of rays inside a scattering particle. In this study, we further enhance their formulae. A scaled projectile length is introduced in the q domain, which is independent of particle physical size as long as the particle shape remains the same The ADT solutions to the extinction and absorption cross sections can be formulated as integrations with respect to the cumulative projectile-length distribution. In this ADT formulation, the information on particle shape is essentially contained in the dimensionless scaled projectile-length specified in the q domain. We show that the present ADT algorithm is the same as the conventional ADT algorithm for spheres and nonspherical particles under specific and randomly orientation conditions. Furthermore, by assuming that the internal field inside a particle is the same as that in the conventional ADT frame, we develop a modified version of ADT that introduces two tuning factors. These tuning factors can be determined in a spherical case by the best fitting of the ADT solution to the Lorenz-Mie results. For nonspherical particles, the tuning factors obtained in a spherical case can be used as surrogates. This approach is validated in the case for circular cylinders whose optical properties can be obtained by the exact T-matrix method.

CHAPTER IV

BACKSCATTERING PROPERTIES OF NONSPHERICAL ICE CRYSTALS AT THE 94GHZ RADAR FREQUENCY

The role that clouds play in the climate system has long been recognized as an important one because of their strong feedback processes.[37] To improve our understanding of their role, global observation of cloud properties is needed. These observations can be obtained with the use of remote-sensing instruments such as radiometers, lidars and radars. The benefits of the observing clouds with 94GHz millimeter wavelength radar have been demonstrated by several literatures.[97,98] The launch of the cloudSAT, an experiment satellite with 94GHz cloud radar, has been planned to measure the vertical structure of clouds and cloud properties.[99] All these processes make the interpretation and evaluation of the cloud radar signals at 94GHz a timely demand.

Radar signals mainly depend on the backscattering properties of cloud particles and their size distributions. When the wavelength of the radar wave is much larger than cloud particles, as in the case of centimeter radars, it is reasonable to treat the scattering of cloud particles as Rayleigh scattering. For 94GHz radar, the wavelength (3.2mm) is comparable to the dimension of large ice crystals often observed in clouds. As a result, some more realistic scattering models must be employed and the effects of nonsphericity must be taken into account in modeling the scattering of the 94 GHz radar wave by cloud ice crystals. Evans and Vivekanandan[100] used the DDA method to study the backscattering properties of ice columns, needles and plates. Schneider and Stephens[101] argued that spheroids are reasonable models of cirrus cloud particles at the wavelength of 3mm and 8mm. Assuming a modified gamma function for the particle size distribution, they also found the median diameter of the volume distribution to be the most critical parameter in the ensemble average of backscattering properties. Aydin and Tang[17] used the FDTD method to study the back scattering properties of hexagonal plates and columns at millimeter radar waves. Due to the adoption of a single aspect ratio model in these previous works, the effects of the particle habit and aspect ratio on the backscattering still remain unclear. Most recently, the accuracy of the DDA method in modeling the backscattering signatures of hexagonal columns and plates with various aspect ratios were

investigated by Okamoto[12]. However, because of the aim of his work, no comparisons were made between different habits. The main purpose of the work is to calculate the backscattering properties of nonspherical ice crystals at 94GHz radar frequency and explore the sensitivity of these properties to the size, shape, aspect ratio, orientation of the ice crystal, as well as the particle size distribution (PSD).

Scattering Parameters and the FDTD Model

All scattering properties of a particle can be derived from the 2×2 amplitude matrix **S** that relates the incident and scattered electric filed as follows[5]:

$$\begin{bmatrix} E_V^{sca} \\ E_H^{sca} \end{bmatrix} = \frac{e^{-ikr}}{ikr} \begin{bmatrix} S_{VV} & S_{VH} \\ S_{HV} & S_{HH} \end{bmatrix} \cdot \begin{bmatrix} E_V^{inc} \\ E_H^{inc} \end{bmatrix}, \tag{4.1}$$

where $k = 2\pi / \lambda$ is the wavenumber of the incidence. Subscript V and H indicate the polarization direction parallel and perpendicular to the scattering plane, respectively The first and the second subscripts of the elements of **S** indicate scattered and incident wave polarization, respectively. The backscattering cross sections of the particle can be express in terms of the amplitude matrix elements as:

$$\sigma_{i,j} = \frac{4\pi}{k^2} \left| S_{i,j} \right|^2, \; i, j = V, H. \tag{4.2}$$

The unit used in this work for the cross sections is mm^2. The effective radar reflectivity factors [10] at V and H polarizations are defined as the ensemble average of the backscattering cross sections:

$$Z_V = \frac{\lambda^4}{(\pi^5 |K|^2)} n_0 \langle \sigma_{VV} \rangle, \tag{4.3a}$$

$$Z_H = \frac{\lambda^4}{(\pi^5 |K|^2)} n_0 \langle \sigma_{HH} \rangle, \tag{4.3b}$$

where $K = (m^2 - 1)/(m^2 + 2)$, and m is the complex refractive index for ice at 94GHz. n_0 is the total number of the particles per cubic meter. Brackets $\langle \cdot \rangle$ indicate the ensemble averaging over the various sizes, shapes and orientations. The unit for the radar reflectivity factors used in this work is $mm^6 m^{-3}$. They are also expressed as $10 \log(Z)$ in dB units. Finally, the relationships between the cross-polarized and co-polarized cross sections are described by the linear depolarization ratios:

$$LDR_v = \frac{\langle \sigma_{HV} \rangle}{\langle \sigma_{VV} \rangle}, \tag{4.4a}$$

$$LDR_H = \frac{\langle \sigma_{VH} \rangle}{\langle \sigma_{HH} \rangle}. \tag{4.4b}$$

For this study, computations of these scattering parameters are carried out using the FDTD method. The theoretical base of the FDTD can be found in many literatures[103-105] and will not be repeated here. In FDTD computations through out this work, the problem space is set up with restriction to two criteria, (i) the ratio of the wavelength to grid size is no smaller than 60, (ii) there

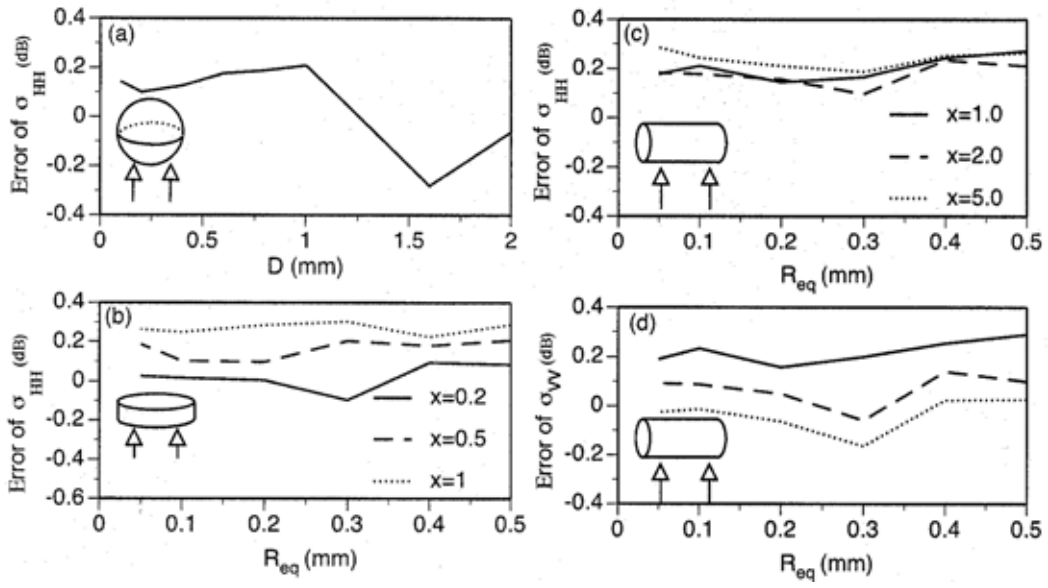

Fig. 24 (a) Errors of the FDTD model for $\langle \sigma \rangle$ of ice spheres. (b) Errors of the FDTD model for $\langle \sigma \rangle$ of plannar ice cylinders. (c) Errors of the FDTD model for $\langle \sigma_{HH} \rangle$ of columnar ice cylinders. (d) Errors of the FDTD model for $\langle \sigma_{VV} \rangle$ of columnar ice cylinders.

must be no less than 20 grid layers along the minimum dimension of the particle. The first criterion insures the accuracy for the computations of large particles, and the second one is for small particles and particles with very small (large) aspect ratios. The FDTD method is first compared with the Lorenz-Mie model to

evaluate its accuracy in modeling the backscattering by ice spheres. As shown in the Fig. 24a, the relative error of the FDTD model for backscattering cross sections of ice spheres is within $\pm 0.3\,\mathrm{dB}\,(\pm 6\%)$ over the size range of 0.03~2 mm. Furthermore, FDTD method is compared with the T-matrix model for the circular cylinder to evaluate its ability to model nonspherical particles. All circular cylinders are assumed to be orientated in a horizontal plane and that the incident wave is vertical. Figure 24b shows the error for the FDTD computation of backscattering cross sections of planar cylinders with various aspect ratios. It can be seen that the error remains within $\pm 0.4\,\mathrm{dB}$. Unlike planar cylinders whose $\langle \sigma_{HH} \rangle$ is equal to $\langle \sigma_{VV} \rangle$ because of the symmetry, the columnar cylinders have different backscattering cross sections at different polarization directions. Therefore, the error for the FDTD computation of $\langle \sigma_{HH} \rangle$ and $\langle \sigma_{VV} \rangle$ of columnar cylinders is plotted in Fig. 24c and Fig. 24d, respectively. The error remains within $\pm 0.4\,\mathrm{dB}$ for both $\langle \sigma_{HH} \rangle$ and $\langle \sigma_{VV} \rangle$. Based on these error evaluations, it is evident that the error introduced by the FDTD model with an appropriate problem space setup can be neglected. It should be marked that the error of the FDTD is defined as $10 \log\left(\frac{\langle \sigma \rangle_{FDTD}}{\langle \sigma \rangle_{theory}}\right)$, where the subscript "theory" refers to the Lorenz-Mie model for the spheres and T-matrix model for the cylinders.

Ice Crystal Models

The nonspherical ice crystals considered in this study are hexagonal plates, hexagonal columns and bullet rosettes. Hexagonal plates and columns are the most often encountered shapes of ice crystals in clouds. They are also the building blocks for many complicated particles such as bullet rosette and aggregates. According to the most recent observations[106], bullet rosettes and their aggregates may be the dominant shape of ice crystals in the cirrus uncinus generating cells, especially for the size range above 100μm.

In order to explore the effect of aspect ratio on backscattering properties later, three aspect ratio models are used to set up geometries of hexagonal plates and columns. The first one is based on the

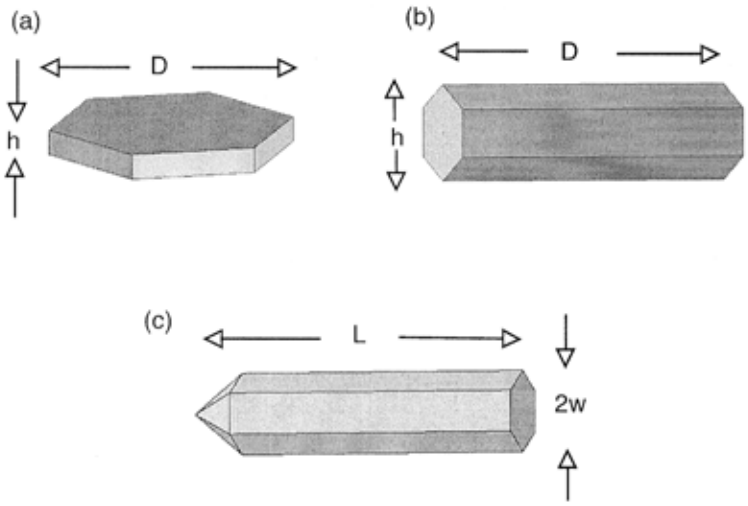

Fig.25 (a) Geometry definition of the hexagonal plate. (b) Geometry definition of the hexagonal column. (c) Geometry definition of the bullet which is used to construct bullet rosettes.

empirical formula for the "diameter-thickness" relationship presented by Auer and Veal:[2]

$$\text{plate} \quad h = 0.0449D^{0449}, \tag{4.5a}$$

$$\text{column} \quad h = 0.1973D^{0.414} \quad D > 0.2mm, \tag{4.5b}$$

$$h = 0.5D \qquad D \le 0.2mm, \tag{4.5c}$$

where D and h are the maximum and minimum dimension of the particle. The definitions of D and h for hexagonal plates and columns are illustrated, respectively, in the Fig. 25a and Fig. 25b. From the Eq. (4.5) the aspect ratio of hexagonal plates and columns can be derived:

$$\text{plate} \quad x = h/D = 0.0449D^{-0.551}, \tag{4.6a}$$

$$\text{column} \quad x = D/h = 5.068D^{0.586} \quad D > 0.2mm, \tag{4.6b}$$

$$x = D/h = 2.0 \qquad D \le 0.2mm, \tag{4.6c}$$

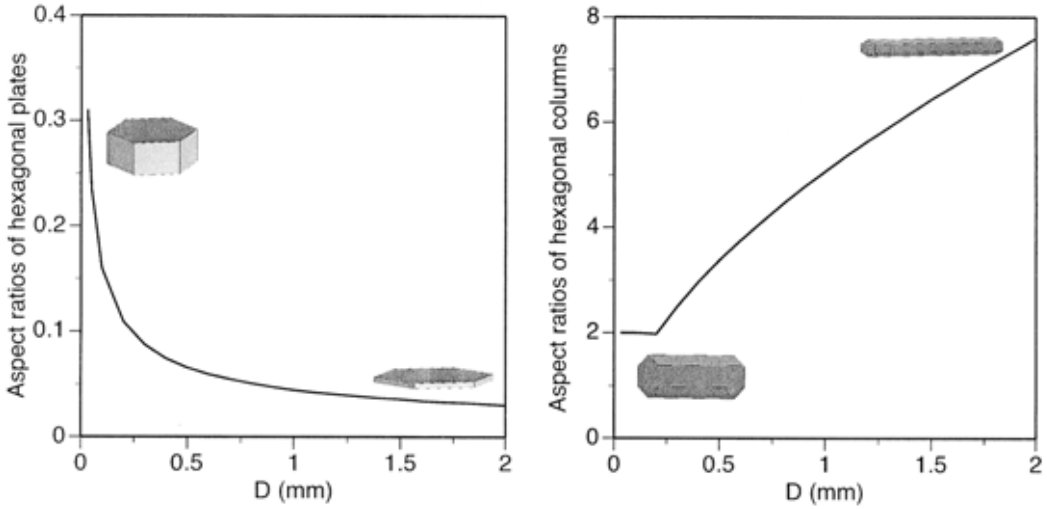

Fig. 26 Aspect ratios of hexagonal plates and columns as the function of maximum dimension.

where x is the aspect ratio of the particle. Obviously, the aspect ratio model defined in Eq. (4.6) is dependent on the maximum dimension of the particles. As shown in the Fig 26, the columns defined in Eqs. (4.6a) and (4.6b) become spindlier and the plates defined in Eq. (4.6c) become flater, which means the nonsphericity increases with the particle size. Hereafter, aspect ratios defined in Eq. (4.6) will be referred to as "real aspect ratios", as they are based on real observations. The other two aspect ratio models are constant, which are 0.1 and 0.25 for hexagonal plates; 2.0 and 10.0 for hexagonal columns.

For the shape of bullet rosette, the number of bullet branches is chosen to be 5, the average number of the in situ observation observed by Heymsfield and Miloshevich[106]. Each bullet branch is assumed to be a hexagonal column with a pyramidal tip. The relationship between semi-width w and length L of the bullet follows the result presented by Heymsfield:[1]

$$w = 0.185L^{0.532} \qquad L > 0.3mm. \tag{4.7}$$

The definition of w and L are illustrated in the Fig. 25c. The height of the pyramidal tip is negligible compared with the length of the bullet, so its effect is not considered. Three branches of the rosette are

assumed to be on the same plane with a 120^0 angle between each other. The other two branches are assumed to be perpendicular to the plane. Consequently, the maximum dimension of bullet rosettes as described above is $2L$ and the aspect ratio is about 1.

The range of the particle size considered in this paper is from 0.03mm (30μm) to 2mm in terms of the maximum dimension. Particles smaller than 30μm are unlikely to demonstrate any geometrical information at 94GHz and the particles larger than 2mm are rarely observed.[1,15,106] As shown in Fig. 27, to specify the orientation of a particle, a fixed right handed coordinate system, xyz, is introduced. For hexagonal plates and columns, two orientation models are considered in this work. The first one is random orientation model (hereafter referred to as '3D orientation'), in which particles can freely rotate about all three axes. The other one is the horizontal orientation model (hereafter referred to as '2D orientation'), in which the broad hexagonal face of plates is on a horizontal plane and plates can freely rotate about the z axis, whereas the long symmetric axis of columns is on a horizontal plane and columns can freely rotate about the x and z axis. Such an orientation model is to simulate the falling of the ice crystals with a predominant large cross section without tumbling. Because bullet rosettes considered in this work do not possess a predominant large cross section, only 3D orientation is considered for them. In all computations, the incidence is assumed to be vertical. The refractive index for the ice is assumed to be $1.78+0.028i$ and the density of the ice used in the work is $0.9g/cm^3$.

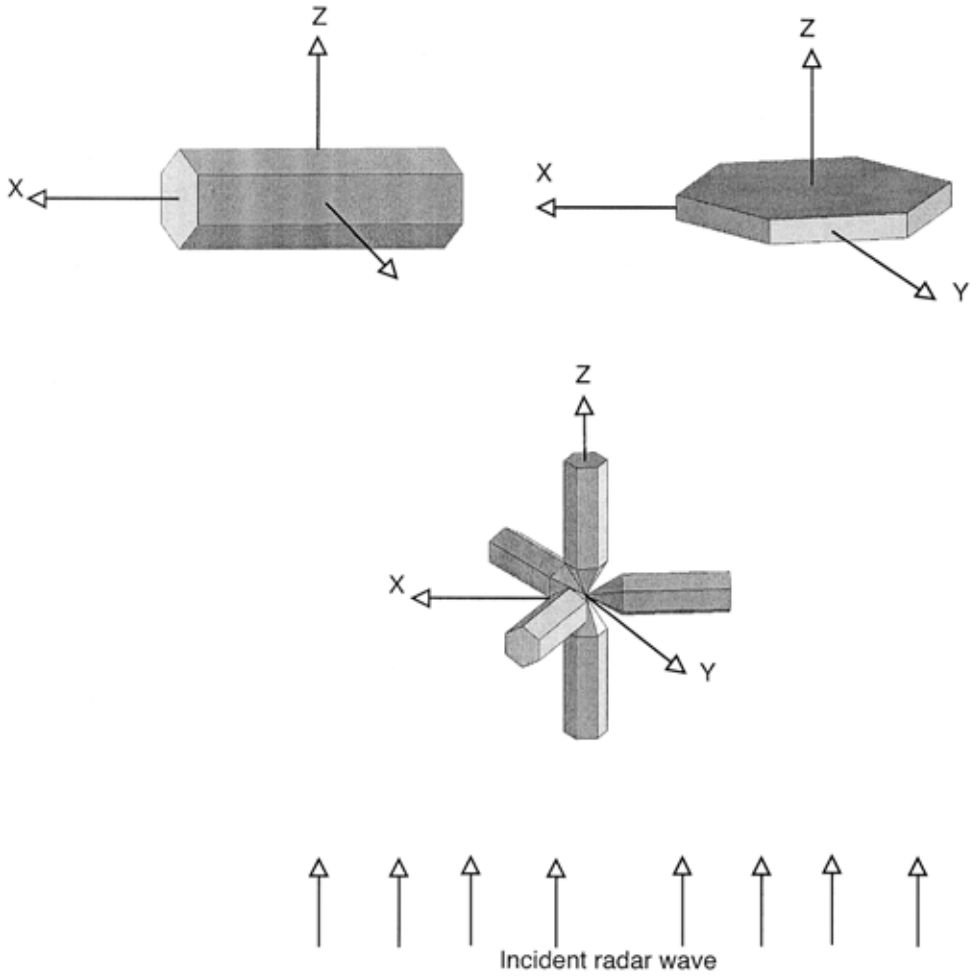

Fig. 27 Orientation models of ice crystals relative to the incident radar wave.

Backscattering Properties of Single Particles

Because all ice crystals considered in this study is either 3D randomly orientated or horizontally oriented on a plane with a vertical incident radar wave, there is no difference between the two polarization directions. As a result, $\langle \sigma_{HH} \rangle$ is always equal to the $\langle \sigma_{VV} \rangle$ and $\langle \sigma_{HV} \rangle$ is always equal to $\langle \sigma_{VH} \rangle$. Figure 28 shows the $\langle \sigma_{HH} \rangle$ versus the maximum dimension for hexagonal plates and columns and bullet rosettes with the 3D orientation, as well as ice spheres. It is evident that approximating the nonspherical ice crystals with ice spheres may induce great errors (-30dB~5dB), especially for those needle-like columns, flake-like plates and bullet rosette. Errors of the approximation in dB unit, defined as $10\log\left(\langle \sigma_{HH} \rangle / \langle \sigma_{HH} \rangle_{Mie}\right)$, are also plotted in Fig 28. The inspection of Fig. 28 also suggests that $\langle \sigma_{HH} \rangle$ has a strong dependence on particle aspect ratios when the maximum dimension is fixed. The value of $\langle \sigma_{HH} \rangle$ for hexagonal plates with aspect ratio 0.25 is about 10dB larger than that of those with aspect ratio 0.l. For the hexagonal columns, the value of $\langle \sigma_{HH} \rangle$ for those with an aspect ratio 2 keeps to be about 20dB larger than those with aspect ratio 10. It seems that ice crystals with an aspect ratio close to unity always have larger backscattering cross sections than those with an aspect ratio either much larger or smaller than 1. However, this doesn't hold in the case of bullet rosette. The backscattering cross sections of bullet rosettes should be the largest as its aspect ratio is about 1, but it is only bigger than those of columns with aspect ratio 10 as shown in Fig. 28. Other than the aspect ratio, we prefer another parameter δ as the most important factor controlling the backscattering cross sections of nonspherical ice crystals. δ is defined as the ratio of r_{eq} to the maximum dimension of the particle:

$$\delta = 2r_{eq} / D, \tag{4.8}$$

where r_{eq} is the radius of the sphere with the same volume with the particle. For hexagonal plates and columns δ can be expressed as the function of the aspect ratio:

$$\delta = 2kx^{1/3} \quad x<1 \text{ (plate)}, \tag{4.9a}$$

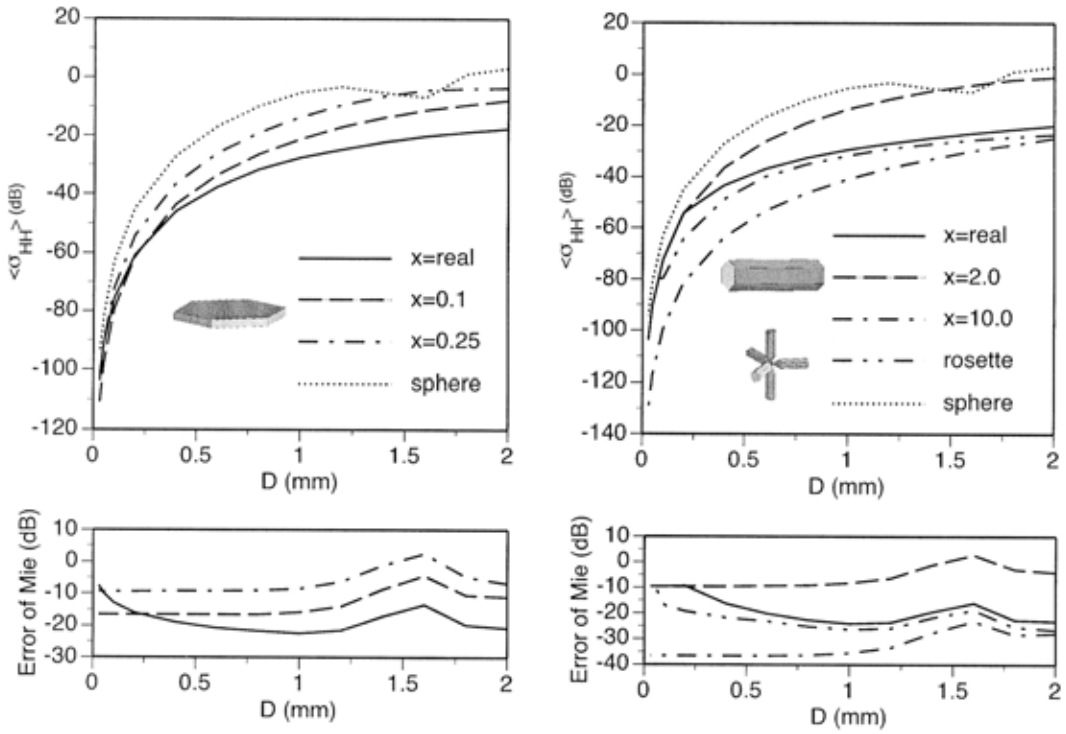

Fig.28 Backscattering cross sections of various ice crystals with the 3D orientation and the error of the Lorenz-Mie approximation.

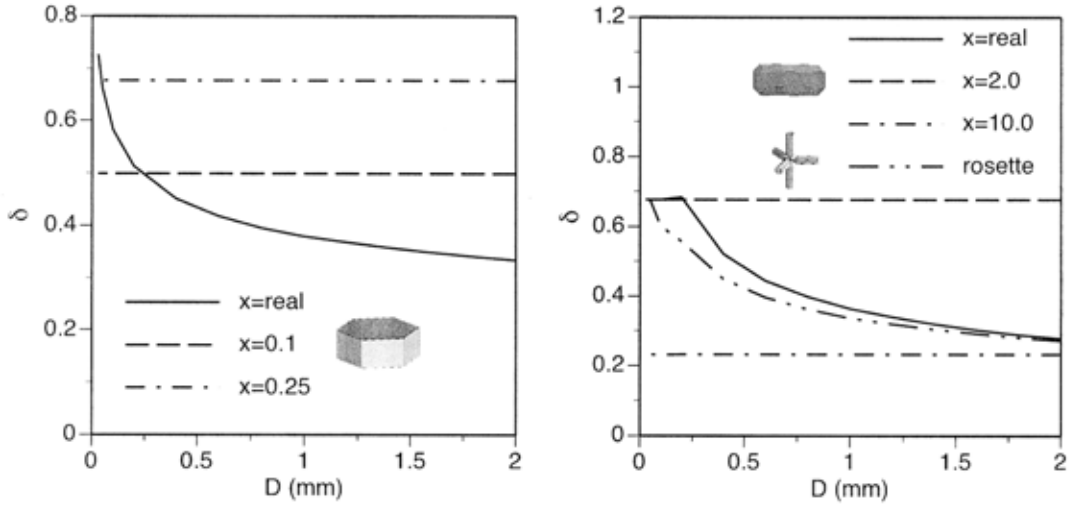

Fig. 29 δ of various ice crystals as the function of maximum dimension.

$$\delta = 2kx^{-2/3} \quad x>1 \quad \text{(column)}, \tag{4.9b}$$

where $k = (9\sqrt{3}/32/\pi)^{1/3}$. For bullet rosettes with the geometry defined in the last section,

$$\delta = 0.37D^{0.688}. \tag{4.10}$$

Fig. 29 shows δ as a function of maximum dimension D for hexagonal particles and bullet rosettes. A comparison between Fig. 28 and Fig.29 makes it quite clear that the backscattering cross sections of hexagonal particles and bullet rosettes in the D space depends primarily on the value of δ.

The orientation of ice crystals relative to the incidence radar wave also has significant impact on the backscattering cross sections. To obtain a better understanding of this impact, a parameter is defined as the ratio of $\langle \sigma_{HH} \rangle$ between ice crystals with the 2D orientation and the 3D orientation:

$$R = \frac{\langle \sigma_{HH} \rangle_{2D}}{\langle \sigma_{HH} \rangle_{3D}}. \tag{4.11}$$

The ratio R in dB unit for various particles is plotted in Fig. 30**.** Obviously, R is greater than 1 (dB >0) for both plates and columns. It is because the 2D orientated particles are always facing the vertical incidence

with the largest cross section. It is also the reason for the needle-like columns and flake-like plates having bigger R than compact particles. The difference between the $\langle\sigma_{HH}\rangle_{2D}$ to $\langle\sigma_{HH}\rangle_{3D}$ is up to 10dB (1000%), which indicates that the orientation effects for the vertical pointed 94GHz radar can not be ignored.

Besides the backscattering cross sections, the linear depolarization ratio (LDR) is also an important parameter for the radar signal. Fig. 31 shows the LDR for 3D orientated particles as the function of the maximum dimension D. It is obvious that the relationship between the LDR and D for hexagonal plates is much different from that for hexagonal columns. The LDR for plates varies slowly over the size range 0~1.5mm and suddenly decreases, while the LDR for the columns all increases with the maximum dimension D.

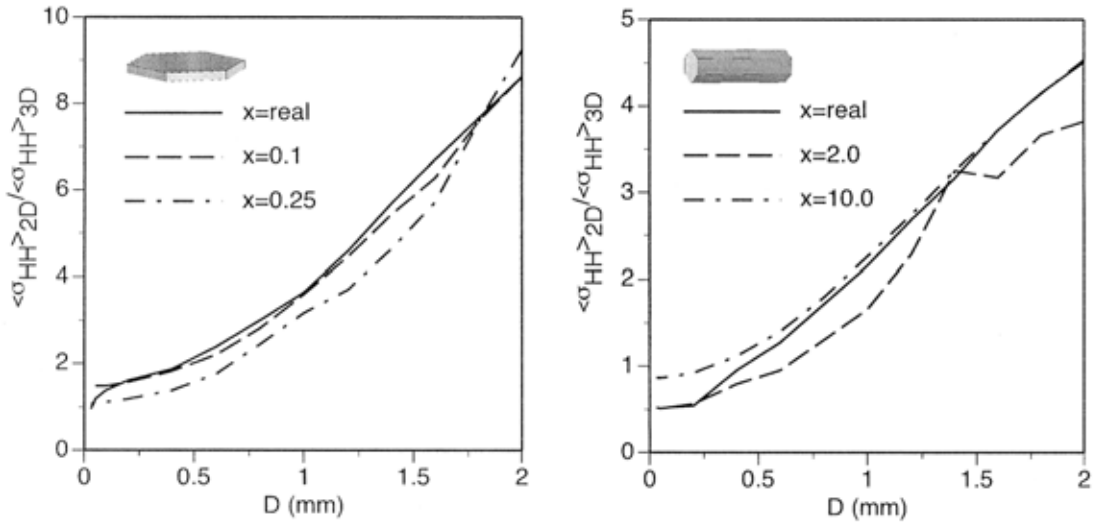

Fig. 30 Difference of backscattering cross sections between the ice crystals with 2D orientation and 3D orientation.

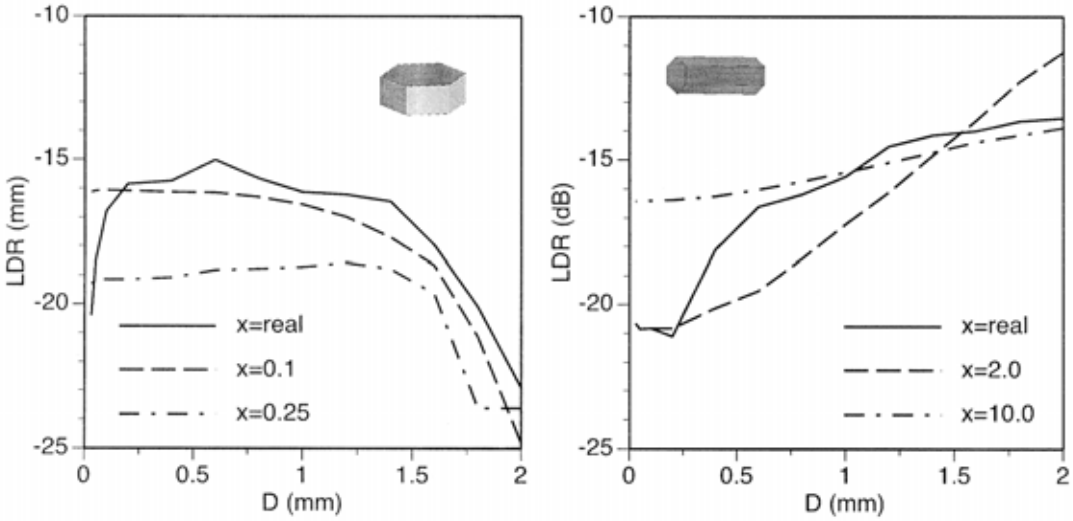

Fig.31 LDR of hexagonal plates and columns with various aspect ratios.

The Relationship between Ice Water Content and Radar Reflectivity Factor

In practice, the radar reflectivity factor (Z_e) is one of the most important radar signals. Actually, it is the only signal for many single-parameter radars. In preceding sections, the effects of size, aspect ratio and orientation on the backscattering properties of nonspherical ice crystals are discussed. In this section, size distribution will be taken into account to explore the relationship between the ice water content (IWC) and radar reflectivity factor of 94 GHz radar. This relationship has long been found to follow the power law, but the reasons are still not clear. The primary objective of this section is to reveal the physical meaning behind the power law relationship between IWC and Z_e. For now, ice crystals considered are assumed to be randomly orientated. Backscattering cross sections of ice crystals with 3D orientation are parameterized as the function of maximum dimensions as follows:

$$\langle \sigma_{HH} \rangle = aD^b \quad (mm^2) \tag{4.12a}$$

or

$$\langle \sigma_{HH} \rangle = 10\log a + b \cdot 10\log D \quad (\text{dB}\, mm^2) \tag{4.12b}$$

where a and b are two parameters. Values of a and b for different particles are given in the Table 2. Because of the average over orientations, the $\langle \sigma_{HH} \rangle$ is equal to the $\langle \sigma_{VV} \rangle$. For the sake of simplicity, we will discard subscripts H and V .The backscattering cross section will be denoted as $\langle \sigma \rangle$.

For the particle size distribution (PSD) model of cloud particles, a modified gamma function has been widely used:[101,107-109]

$$N(D) = N_0 D^{\alpha} \exp(-\beta D), \tag{4.13}$$

where $N(D)$(in $mm^{-1}m^{-3}$ unit) is the concentration of particles with the maximum dimension from D to $D + dD$. The character of the PSD is controlled by free parameters N_0(in $mm^{-1-\mu}m^{-3}$ unit), α and β(in mm^{-1} unit). The effect of N_0 on the PSD is linear. It changes only the magnitude of the concentration at each size bin. Dispersion α and slope β together shape the PSD. A PSD defined in Eq. (4.13) has a peak at $D_m = \alpha / \beta$. The ensemble average of a variable over the PSD is given by:

$$\langle X \rangle = \int_{D^l}^{D^u} X(D)N(D)dD = \int_{D^l}^{D^u} X(D)N_0 D^{\alpha} \exp(-\beta D)dD, \tag{4.14}$$

Table 2 Values of a and b in the parameterization $<\sigma>= aD^b$ for various ice crystals

Ice crystal types	a	b
Plate x = real	1.2930e-003	4.6931
Plate x =0.1	5.9439e-003	5.7232
Plate x =0.25	2.8264e-002	5.6668
Column x =real	3.1804e-002 $D \le 0.2mm$ 1.0337e-003 $D > 0.2mm$	5.7456 $D \le 0.2mm$ 3.4827 $D > 0.2mm$
Column x =2.0	3.1804e-002	5.7456
Column x =10.0	7.4016e-005	5.8326

where D^l and D^u are lower and upper end of the PSD. The value of α varies between 0 and 2 .(e.g., Kosarev and Mazin[109]). Based on observations, the peak of the PSD D_m usually falls in the range of 0.01mm-1mm. (e.g., Heymsfield and Iaqunita[1], Heymsfield and Miloshevich[106]). One special case deserves some more discussions. If the variable $X(D)$ is in the form $X(D) = AD^B$, its ensemble average over the PSD can be expressed as the function of A and B :

$$\langle X \rangle = f(A,B) = \int_{D^l}^{D^u} AD^B N_0 D^\alpha \exp(-\beta D) dD$$

$$= AN_0(\beta)^{-(B+\alpha+1)}\left[\gamma\left(B+\alpha+1,\beta D^u\right) - \gamma\left(B+\alpha+1,\beta D^l\right)\right], \tag{4.15}$$

where $\gamma(a,x) = \int_0^x t^{a-1}e^{-t}dt$ is the incomplete gamma function.

Noting that the backscattering cross sections of nonspherical ice crystals with 3D orientation has been parameterized as $\sigma = aD^b$ in Eq. (4.13), then Z_e defined in the Eq. (4.3) becomes:

$$Z_e = Cf(a,b), \tag{4.16}$$

where $C = \frac{\lambda^4}{(\pi^5 |K|^2)}$. Obviously, α and β represent the effect of the PSD on the reflectivity, while a and b represent the effect of particle shapes.

The ice water content (IWC) is defined as:

$$IWC = \rho \langle V(D) \rangle, \tag{4.17}$$

where ρ is the density of ice and $V(D)$ is the volume of ice crystals with the maximum dimension D. $V(D)$ can be always expressed as follows:

$$V(D) = A_V D^{B_V}, \tag{4.18}$$

where A_V and B_V are two parameters and their values for different ice crystals can be found in Table 3. Substituting the Eq. (4.18) into Eq. (4.17), the IWC becomes:

$$IWC = \rho f(A_V, B_V). \tag{4.19}$$

Dividing Eq. (4.19) by Eq. (4.16), an analytical expression for $IWC - Z_e$ can be immediately obtained:

$$\frac{IWC}{Z_e} = \frac{\rho f(A_V, B_V)}{C f(a,b)} = \frac{\rho A_V}{Ca} (\beta)^{(b-B_V)} K_\gamma \tag{4.20}$$

where $K_\gamma = \frac{\gamma(B_V + \alpha + 1, \beta D^u) - \gamma(B_V + \alpha + 1, \beta D^l)}{\gamma(b + \alpha + 1, \beta D^u) - \gamma(b + \alpha + 1, \beta D^l)}$. A glance at Eq. (4.20) may lead to the impression that $IWC - Z_e$ relation is linear. This is true only when all parameters at the right hand of the equation do not change with the IWC or Z_e. Under such circumstance, the only active parameter is N_0 that equally magnifies the IWC and Z_e. It is evident that both the shape and the PSD of ice crystals in the cloud have an impact on the $IWC - Z_e$ relationship. Consequently, two sensitivity studies are carried out. In the first one, the PSD is fixed to see how $IWC - Z_e$ relationship varies with particle shapes. For the PSD, α and β are set to be 1.0 and 5.0, respectively. The value of N_0 is obtained from the specified values of the total ice crystals concentration which is assumed to vary from $10^3\ m^{-3}$ to $10^5\ m^{-3}$. Fig. 32 shows $IWC - Z_e$ relationships for hexagonal plates and columns. In the other sensitivity study, nine size distributions are

Table 3 Values of A_V and B_V in the parameterization $V(D) = A_V D^{B_V}$ for various ice crystals

Ice crystal types	A_V	B_V
Plate x = real	0.0291	2.449
Plate x =0.1	0.0650	3
Plate x =0.25	0.162	3
Column x =real	0.162 $D \le 0.2mm$ 0.0252 $D > 0.2mm$	3 $D \le 0.2mm$ 1.828 $D > 0.2mm$
Column x =2.0	0.162	3
Column x =10.0	0.00650	3

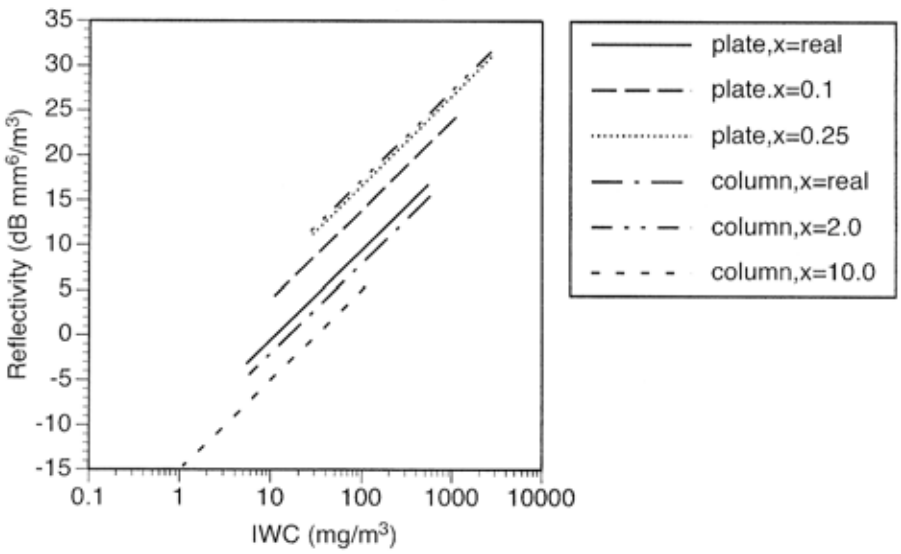

Fig. 32 $IWC - Z_e$ relationships for various hexagonal plate and column ensembles with fixed PSD configuration.

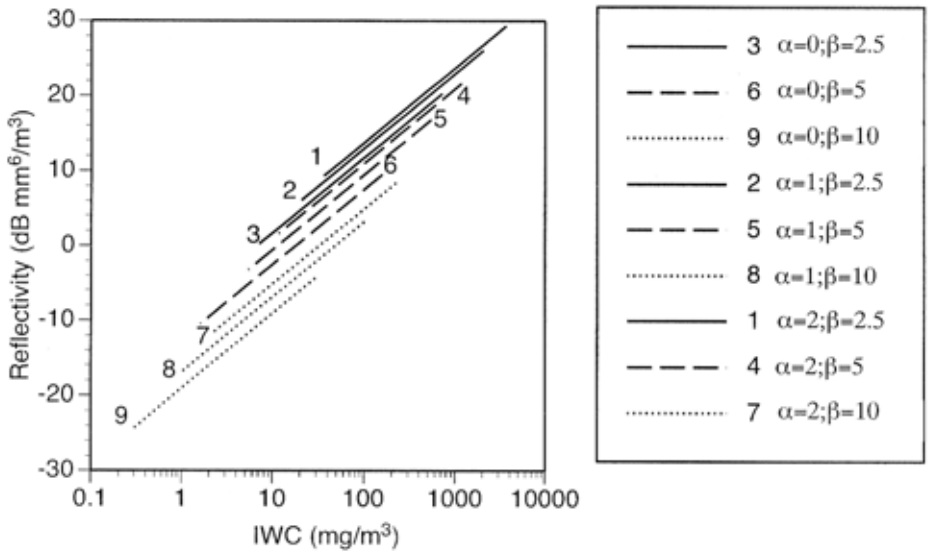

Fig. 33 $IWC - Z_e$ relationships for ensembles of hexagonal plates with the "real aspect ratio", the PSD configuration of each ensemble is different.

constructed using three values of α and β. For each distribution, the $IWC - Z_e$ relationship of the hexagonal plates with the "real aspect ratios" defined in the Eq. (4.6) is plotted in Fig. 33. It is apparent that the reflectivity variation in Fig. 33 is more sensitive to changes in β, as suggested by the term $(\beta)^{(b-B_V)}$ in the Eq. (4.20).

As discussed above, the $IWC - Z_e$ relationship given by Eq. (4.20) suggests that a change to PSD magnitude without any changes on the PSD characters or particle habits leads only to a linear $IWC - Z_e$ relationship. However, if some of the parameters at RHS of Eq. (4.20) are functions of the IWC, Eq. (4.20) may become nonlinear and complicated. As an example, the β is assumed to be related to the IWC as the power law:

$$\beta = Y \cdot IWC^{-\mu}, \tag{4.21}$$

where $Y > 0$ and $\mu > 0$ are two free parameters. Such a relationship between β and IWC indicates the

character of the PSD varies with the IWC. When α is fixed, Eq. (4.21) indicates that the increasing of the IWC may induce a position shift of the peak of the PSD in favor of the larger particles. The physical basis of this assumption has been discussed by Schneider and Stephens.[101] As they pointed out, the value of the Y and μ must be determined from the observations, otherwise significant errors may be introduced. Because no observations are involved, the aim of this work is not

to seek the proper values of Y and μ but to investigate the effects of this assumption on the $IWC - Z_e$ relationship. Substituting β defined in the Eq. (4.21), the $IWC - Z_e$ relationship in Eq. (4.20) becomes

$$IWC = \left(\frac{\rho A_V Y^{(b-B_V)}}{Ca} K_\gamma \right)^{\frac{1}{1+\mu(b-B_V)}} Z_e^{\frac{1}{1+\mu(b-B_V)}} \tag{4.22}$$

Because the variability of the coefficient K_r is small with the restriction that IWC is in the range 1-1000 mg/m^3, its effects is neglected. Consequently, Eq. (4.22) reduces to the well-known power law relationship of IWC and Z_e:

$$IWC = A_Z Z_e^{B_z}, \tag{4.23}$$

Where $A_Z = \left(\frac{\rho A_V Y^{(b-B_V)}}{Ca} K_\gamma \right)^{\frac{1}{1+\mu(b-B_V)}}$, $B_Z = \frac{1}{1+\mu(b-B_V)}$. Clearly, the exponent B_z in the $IWC - Z_e$ relation ship is affected the by the peak deviation of PSD through the factor μ as well as the particle habits through the factor $b - B_v$. As shown in the Table 2 and Table 3, the values of the $b - B_v$ for particles with fixed aspect ratio are always closed to 3, while significant deviation is found for the particles whose aspect ratio changes with its size. Therefore, the effects of particle size on the aspect ratio must be considered. Because both $b - B_V$ and μ are positive, the value of the B_Z is always smaller than 1. The most important parameter to the term A_z is $Y^{(b-B_V)}$, which is also modulated by both the PSD and the particle habits. As revealed by the Eqs. (4.22) and (4.23), as well as in Fig. 32 and Fig. 33, there are great uncertainties in the $IWC - Z_e$ relationship. Nonetheless, $IWC - Z_e$ relationship in Eqs. (4.22) and (4.23) can help to reduce ambiguities and may serve as a crude means of estimating the IWC from the radar reflectivity. As an example, Fig. 34 shows the $IWC - Z_e$ relationship for hexagonal plates with the "real aspect ratio" and the assumption $\beta = 10IWC^{-0.3}$. The corresponding values of A_z and B_z are 35.6 and 0.663, respectively. Several

$IWC - Z_e$ relationships proposed by several previous works are also plotted.[101,110,111]

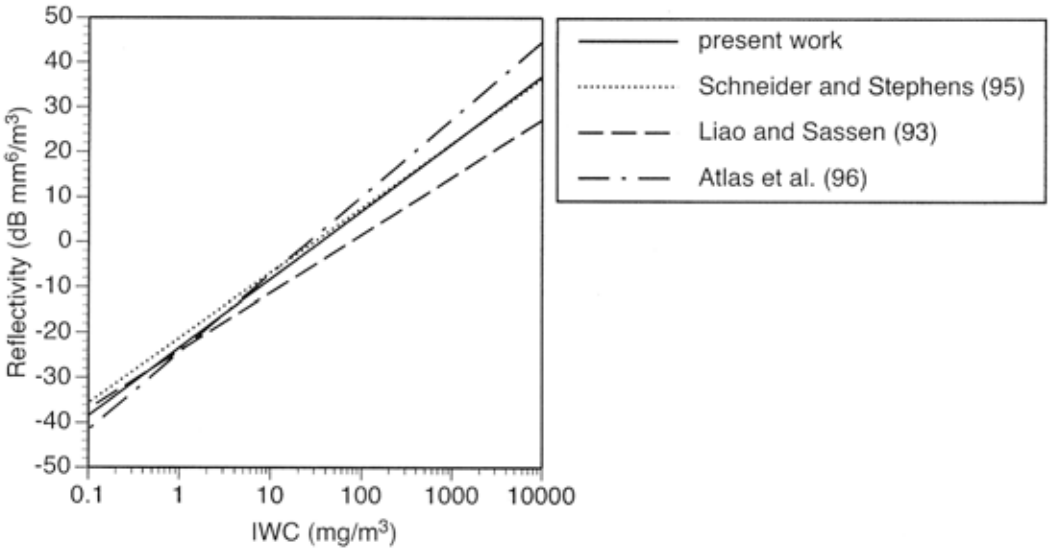

Fig. 34 $IWC - Z_e$ reported by various researchers.

Summary and Conclusions

Because the wavelength of 94GHz radar is comparable to the size of ice crystals in clouds, the effects of nonsphericity on the backscattering properties of these ice crystals must be studied by using rigorous scattering models. In this study, backscattering properties of hexagonal plates and hexagonal columns and bullet rosettes are investigated by using the Finite-Difference Time Domain method (FDTD). Both horizontal orientation and random orientation are considered. The most important factor controlling the backscattering cross section of random oriented particles is found to be the ratio of the volume-equivalent radius to the maximum dimension. Significant difference (up to 10dB) of backscattering cross sections is found between the horizontal and the random orientation. Moreover, this difference for the planar particles is larger than columnar particles. The linear depolarization ratio (LDR) shows a strong dependence on the particle habits and aspect ratios. With the parameterization of backscattering cross section as the function of the particle size, an analytical expression of the relationship between radar reflectivity (Z_e) and ice water content (IWC) is derived. It is shown that a change to the concentration of ice crystals without any changes on the size distribution or particle habits leads only to a linear $IWC - Z_e$ relationship. The famous power law $IWC - Z_e$ relationship is the result of the shift of the peak of particle size distribution.

CHAPTER V

CONCLUSIONS

The phase function of the droxtals at the visible wavelength (0.66 μm) displays maxima at scattering angles smaller than 22 . The maxima may be explained by consideration of multiple scattering within the particle resulting from the pyramidal faces. Because of the hexagonal structure of the crystal facets, all elements of scattering matrix show similarities to the properties that have been observed in those of hexagonal ice crystals. At 11 μm, where absorption of the incident radiation within the particle becomes dominant, the phase functions of the 18-faced and 20-faced droxtals are essentially featureless. A comparison of the linear depolarization between hexagonal ice crystals and droxtal ice crystals suggests that there is a notable difference at the backscattering angles. This difference is also observed between droxtal ice crystals with different geometric configurations. Finally, we note that the average of the phase function over various geometric configurations effectively smoothes out the small oscillations, especially in the backscattering directions.

Recently, Xu et al.[85] and Xu[86] reformulated the conventional ADT by introducing the probability distribution function of the geometric paths of rays inside a scattering particle. In this study, we further enhance their formulae. A scaled projectile length is introduced in the q domain, which is independent of particle physical size as long as the particle shape remains the same The ADT solutions to the extinction and absorption cross sections can be formulated as integrations with respect to the cumulative projectile-length distribution. In this ADT formulation, the information on particle shape is essentially contained in the dimensionless scaled projectile-length specified in the q domain. We show that the present ADT algorithm is the same as the conventional ADT algorithm for spheres and nonspherical particles under specific and randomly orientation conditions. Furthermore, by assuming that the internal field inside a particle is the same as that in the conventional ADT frame, we develop a modified version of ADT that introduces two tuning factors. These tuning factors can be determined in a spherical case by the best fitting of the ADT solution to the Lorenz-Mie results. For nonspherical particles, the tuning factors obtained in a spherical case can be used as surrogates. This approach is validated in the case for circular cylinders whose optical properties can be obtained by the exact T-matrix method.

Because the wavelength of 94GHz radar is comparable to the size of ice crystals in clouds, the effects of nonsphericity on the backscattering properties of these ice crystals must be studied by using rigorous scattering models. In this study, backscattering properties of hexagonal plates and hexagonal columns and bullet rosettes are investigated by using the Finite-Difference Time Domain method (FDTD). Both horizontal orientation and random orientation are considered. The most important factor controlling the backscattering cross section of random oriented particles is found to be the ratio of the volume-equivalent radius to the maximum dimension. Significant difference (up to 10dB) of backscattering cross sections is found between the horizontal and the random orientation. Moreover, this difference for the planar particles is larger than columnar particles. The linear depolarization ratio (LDR) shows a strong dependence on the particle habits and aspect ratios. With the parameterization of backscattering cross section as the function of the particle size, an analytical expression of the relationship between radar reflectivity (Z_e) and ice water content (IWC) is derived. It is shown that a change to the concentration of ice crystals without any changes on the size distribution or particle habits leads only to a linear $IWC - Z_e$ relationship. The famous power law $IWC - Z_e$ relationship is the result of the shift of the peak of particle size distribution.

CHAPTER VI

POTENTIAL PROBLEMS AND FUTURE WORK

Although there are many challenging problems in the field of electromagnetic scattering by nonspherical particles, three of them are worth of more research efforts in the near future because of their importance in practice related to the atmospheric science.

The first one is how to enhance the accuracy of scattering property calculations for particles with a size parameter falling in the range form twenty to several hundred. Twenty is the largest size parameter that current FDTD codes can handle and several hundred is the smallest size parameter for approximation methods such as GOM can process with quantitatively reliable results. The accuracy of the calculation between these two numbers is pretty low. Unfortunately, a large amount of calculations for the scattering properties of ice crystals falls in this range. Extending the applicability range of FDTD to cover this gap seems impractical at least for now. Therefore, some special or new methods need to be developed.

Secondly, the great variability of shapes and compositions of atmospheric aerosols (ice crystal, soot, dust) has been well recognized. However, shape models for atmospheric aerosols considered in current research related to the radiative transfer modeling, parameterization of radiative properties of clouds in climate modeling and interpretation of remote sensing measurements seems far from realistic. Statistical methods must be adopted to investigate the impact of this variability on the scattering properties of atmospheric aerosols, or at least scattering properties should be given together with statistical properties such as the reliability and variability to avoid misleading.

The third is related to the parameterization of scattering properties. Currently, scattering properties are usually parameterized in terms of effective sizes, maximum dimensions volume-equivalent radiuses. However, climate modeling usually needs the parameterization in terms of the temperature, or wind velocity. Filling up this gap requires the cooperation between the members of various disciplines.

REFERENCES

1. A. J. Heymsfield and J. Iaqunita, "Cirrus crystal terminal velocities," J. Atmos. Sci., **57**, 916-938 (2000).

2. A. H. Auer and D. L. Veal, "The dimension of ice crystals in natural clouds," J. Atmos. Sci., **27**, 919-926 (1970).

3. H. C. van de Hulst, *Light scattering by small particles* (Wiley, New York, 1957).

4. M. Kerker, *The scattering of light and other electromagnetic radiation* (Academic Press, San Diego, 1969).

5. G. F. Bohren and D. R. Huffman, *Absorption and scattering of light by small particles* (John Wiley and Sons, New York, 1983).

6. M. I. Mishchenko, J. W. Hovenier, and L. D. Travis, *Light scattering by nonspherical particles* (Academic Press, San Diego, 2000).

7. F. M. Kahnert, "Numerical methods in electromagnetic scattering theory," J. Quant. Spectros. Rad. Transfer, **79**, 755-824 (2003).

8. P. Minnis, K. N. Liou and Y. Takano, "Inference of cirrus cloud properties using satellite-observed visible and infrared radiances. Part I: Parameterization of radiance fields," J. Atmos. Sci., **50**, 1279–1304 (1993).

9. P. Minnis, D. P. Garber, D. F. Young, R. F. Arduini, and Y. Takano, "Parameterizations of reflectance and effective emittance for satellite remote sensing of cloud properties," J. Atmos. Sci., **55**, 3313–3339 (1998).

10. A. J. Baran, P. N. Francis, and P. Yang, "A process study of the dependence of ice crystal absorption on particle geometry: Application to aircraft radiometric measurements of cirrus cloud in the terrestrial window region," J. Atmos. Sci., **60**, 417-427 (2003).

11. J. Reichardt, S. Reichardt, P. Yang and T. J. McGee, "Retrieval of polar stratospheric cloud microphysical properties from lidar measurements: Dependence on particle shape assumptions," J. Geophys. Res., **107**, 8282, doi:10.1029/2001JD001021 (2002).

12. H. Okamoto, "Information content of the 95-GHz cloud radar signals: Theoretical assessment of effects of nonsphericity and error evaluation of the discrete dipole approximation," J. Geophys. Res., **107,** 4628, doi:10.1029/2001JD001386 (2002).

13. A. J. Baran, J. S. Foot and D. L. Mitchell, "Ice crystal absorption: A comparison between theory and implications for remote sensing," Appl Opt., **37**, 2207-2215 (1998).

14. C. J. Stubenrauch, R. Holz, A. Chedin, D. L. Mitchell, A. J. Baran, "Retrieval of cirrus ice crystal sizes from 8.3 and 11.1 μm emissivities determined by the improved initialization inversion of TIROS-N Operational Vertical Sounder observations," J. Geophys. Res., **104**, 31793-31808 (1999).

15. M. I. Mishchenko, and K. Sassen, "Depolarization of lidar returns by small ice crystals: An application to contrails," Geophys. Res. Lett., **25**, 309-312 (1998).

16. A. Kouzoubov, M. J. Brennan, J. C. Thomas and R. H. Abbot, "Monte Carlo simulations of the influence of particle nonsphericity on remote sensing of ocean water," J. Geophys. Res., **104**, 31731-31737 (1999).

17. K. Aydin, and C. Tang, "Millimeter wave radar scattering from model ice crystals distributions," *IEEE Trans. Geosci. Remote Sens*., **35**, 140–146 (1997).

18. C. E. Dungey and C. F. Bohren, "Backscattering by nonspherical hydrometeors as calculated by the coupled-dipole method: An application in radar meteorology," J. Atmos. Oceanic Technol., **10**, 526–532 (1993).

19. H. Okamoto, A. Macke, M. Quante, and E. Raschke, "Modeling of backscattering by non-spherical ice particles for the interpretation of cloud radar signals at 94GHZ. An error analysis," Contrib. Atmos. Phys., **68**, 319–334 (1995).

20. T. Nousiainen, K. Muinonen, and P. Räisänen, "Scattering of light by large Saharan dust particles in a modified ray optics approximation," J. Geophys. Res., **108**, 4025, doi:10.1029/2001JD001277 (2003).

21. P. Yang, K. N. Liou, M. I. Mishchenko and B. C. Gao, "An efficient finite difference time domain scheme for light scattering by dielectric particles: Application to aerosols," Appl. Opt., **39**, 3727-3737(2000).

22. V. A. Babenko, "Improved algorithm for T-matrix computations of light scattering by aerosol spheroidal particles," J. of Aerosol Sci., **28,** S203-S204 (1997).

23. K. N. Liou, Y. Takano, and P. Yang, "Radiative transfer in cirrus cloud: Light scatting and spectral information," in *Cirrus*, Eds. D. K. Lynch, K. Sassen, D. O. Starr and G. Stephens, (Oxford University Press, New York, 2002).

24. K. Okada, A. Kobayashi, Y. Iwasaka, H. Naruse, T. Tanaka, and O. Nemoto, "Features of individual Asian dust-storm particles collected at Nagoya, Japan," J. Meteorol. Soc. Jpn., **65**, 515– 521 (1987).

25. T. Wriedt, "A Review of Elastic Light Scattering Theories," Part. Syst. Charact., **15**, 67-74 (1998).

26. T. Wriedt, and U. Comberg, "Comparison of computational scattering method," J. Quant. Spectros. Rad. Transfer, **60**, 3411-3423 (1998).

27. B. T. Draine and P. J. Flatau, "Discrete-dipole approximation for scattering calculations," J. Opt. Soc. Am. A, **11,** 1491–1499 (1994).

28. M. I. Mishchenko, L. D. Travis, and D. W. Mackowski, "T-matrix computations of light scattering by nonspherical particles: A review," J. Quant. Spectros. Rad. Transfer, **55**, 535-575 (1996).

29. M. I. Mishchenko and L. D. Travis, "Capabilities and limitations of a current FORTRAN implementation of the T-matrix method for randomly oriented, rotationally symmetric scatterers," J. Quant. Spectros. Rad. Transfer, **60**, 309-324 (1998).

30. D. J. Wielaard, M. I. Mishchenko, A. Macke and B. E. Carlson, "Improved T-matrix computations for large, nonabsorbing and weakly absorbing nonspherical particles and comparison with geometric optics approximation," Appl. Opt., **36**, 4305-4313 (1997).

31. P. Yang, K. N. Liou, K. Wyser and D. Mitchell, "Parameterization of the scattering and absorption properties of individual ice crystals," J. Geophys. Res., **105**, 4699-4718 (2000).

32. P. Yang, B. A. Baum, A. J. Heymsfield, Y. X. Hu, H.-L. Huang, S.-Chee Tsay, and S. Ackerman,

"Single-scattering properties of droxtals," J. Quant. Spectros. Rad. Transfer, **79-80**, 1159-1180, (2003).

33. Z. Zhang, P. Yang, G. W. Kattawar, S.-C. Tsay. B. A. Baum, H.-L. Huang, Y. X. Hu, A. J. Heymsfield, and J. Reichardt, "Geometric optics solution to light scattering by droxtal ice crystals," Appl. Opt., **43**, 2490-2499 (2004).

34. P. Yang and K. N. Liou, "Light scattering by hexagonal ice crystals: Solution by ray-by-ray integration algorithm," J. Opt. Soc. Amer. A, **14**, 2278-2289 (1997).

35. J. Zhao and Y. Hu, "Bridging technique for calculating the extinction efficiency of arbitrary shaped particles," Appl. Opt., **42**, 4937-4945 (2003).

36. D. L Mitchell, "Parameterization of the Mie extinction and absorption coefficients for water clouds," J. Atmos. Sci., **57**, 1311-1326 (2000).

37. K. N. Liou., "Influence of cirrus clouds on weather and climate processes: A global perspective," Mon. Wea. Rev., **114**, 1167-1199 (1986).

38. G Stephens, "Cirrus, climate and global change," in *Cirrus*, Eds. D. K. Lynch, K. Sassen, D. O. Starr and G. Stephens, (Oxford University Press, New York, 2002).

39. P. Wendling, R. Wendling and H. K. Weikman, "Scattering of solar radiation by hexagonal ice crystals," Appl. Opt., **18**, 2663-2671 (1979).

40. Q. M. Cai and K. N. Liou, "Theory of polarized light scattering by hexagonal ice crystals," Appl. Opt., **21**, 3569-3580 (1982).

41. Y. Takano and K. Jayaweera, "Scattering phase matrix for hexagonal ice crystals computed from ray tracing," Appl. Opt., **24**, 3254-3263 (1985).

42. Y. Takano and K. N. Liou, "Solar radiative transfer in cirrus clouds. Part I. Single-scattering and optical properties of hexagonal ice crystals," J. Atmos. Sci., **46**, 3-19 (1989).

43. A. Macke, "Scattering of light by polyhedral ice crystals," Appl. Opt., **32,** 2780-2788 (1993).

44. A. Macke, J. Mueller and E. Raschke, "Single scattering properties of atmospheric ice crystals," J. Atmos. Sci., **53**, 2813-2825 (1996).

45. K. Muinonen "Scattering of light by crystals: A modified Kirchhof approximation," Appl. Opt., **28**, 3044-3050 (1989).

46. M. Hess, R.B.A. Koelemeijer, and P. Stammes, "Scattering matrices of imperfect hexagonal crystals," J. Quant. Spectros. Rad. Transfer, **60**, 301-308 (1998).

47. P. Yang and K. N. Liou, "Single-scattering properties of complex ice crystals in terrestrial atmosphere," Contr. Atmos. Phys., **71**, 223-248 (1998).

48. M. I. Mishchenko, W. B. Rossow, A. Macke, and A. A. Lacis, "Sensitivity of cirrus cloud albedo, bidirectional reflectance, and optical thickness retrieval to ice-particle shape," J. Geophys. Res., **101**, 16973-16985 (1996).

49. K. N. Liou, Y. Takano, and P. Yang, Light scattering and radiative transfer by ice crystal clouds: Applications to climate research. in "*Light scattering by nonspherical particles: Theory, measurements, and geophysical applications*", Eds. M. I. Mishchenko, J. W. Hovenier, and L. D.

Travis, (Academic Press, New York,2000),174-220

50. P. R. Lawson, B. A. Baker, C. G. Schmitt, and T. J. Jensen, "An overview of microphysical properties of Arctic clouds observed in May and July 1998 during FIRE ACE," J. Geophys. Res., **106**, 14989-15014 (2001).

51. E. J. Jensen, O. B. Toon, H. B. Selkirk, J. D. Spinhirne, and M. R. Schoeberl, "On the formation and persistence of subvisible cirrus clouds near the tropical tropopause," J. Geophys. Res., **101**, 21361-21375 (1996).

52. P. Yang, B.-C. Gao, B. A. Baum, W. Wiscombe, Y. Hu, S. L. Nasiri, A. Heymsfield, G. McFarquhar, and L. Miloshevich, "Sensitivity of cirrus bidirectional reflectance in MODIS bands to vertical inhomogeneity of ice crystal habits and size distributions," J. Geophys. Res., **106**, 17267-17291 (2001).

53. G. M. McFarquhar, P. Yang, A. Macke, and A. J. Baran, "A new parameterization of single-scattering solar radiative properties for tropical anvils using observed ice crystal size and shape distributions," J. Atmos. Sci., **59**, 2458-2478 (2002).

54. M. I. Mishchenko, "Light scattering by size-shape distributions of randomly oriented axially symmetric particles of a size comparable to wavelength," Appl. Opt., **32**, 623-625 (1993).

55. J. Reichardt, S. Reichardt, P. Yang, and T. J. McGee, "Retrieval of polar stratospheric cloud microphysical properties from lidar measurements: Dependence on particle shape assumptions," J. Geophys. Res. **107**(D20), 8282, doi:10.1029/2001JD001021 (2002).

56. L. Liu and M. I. Mishchenko, "Constraints on PSC particle microphysics derived from lidar observations" J. Quant. Spectros. Rad. Transfer, **70**, 817-831 (2001).

57. W. C. Thuman and E. Robinson, "Studies of Alaskan ice-fog particles," J. Meteor. **11,** 151-156 (1954).

58. T. Ohtake, "Unusual crystal in ice fog," J. Atmos. Sci., **27**, 509-511 (1970).

59. W. Sun and Q. Fu, "Finite-difference time-domain solution of light scattering by dielectric particles with large complex refractive indices," Appl. Opt. **39**, 5569-5578 (1999).

60. M. I. Mishchenko and A. Macke, "How big should hexagonal ice crystals be to produce halos?" Appl. Opt. **38**, 1626-1629 (1999).

61. S. Havemann, A. J. Baran, and J. M. Edwards, "Implementation of the T-matrix method on a massively parallel machine: A comparison of hexagonal ice cylinder single-scattering properties using the T-matrix and improved geometric optics methods" J. Quant. Spectros. Rad. Transfer, **79-80**, 707-720 (2003).

62. P. Yang, and K. N. Liou, "Light scattering by hexagonal ice crystals: Comparison of finite-difference time domain and geometric optics methods," J. Opt. Soc. Amer. A, **12**, 162-176. (1995).

63. P. Yang and K. N. Liou, "Finite-difference time domain method for light scattering by small ice crystals in three-dimensional space," J. Opt. Soc. Amer. A, **13**, 2072-2085 (1996)

64. P. Yang and K. N. Liou, "Geometric-optics-integral-equation method for light scattering by nonspherical ice crystals," Appl. Opt., 35, 6568-6584 (1996)

65. A. J. Heymsfield and L. M. Miloshevich, "Homogeneous ice nucleationand supercooled liquid water in orographic wave clouds," J. Atmos. Sci., **50**, 2335-2353 (1993)

66. D. Rosenfeld and W. L. Woodley, “Deep convective clouds with sustained supercooled liquid water down to -37.5 degrees,” Nature, **405**, 440-442 (2000)

67. R. Greenler, *Rainbows, halos and glories* (Cambridge University Press, Cambridge, 1980)

68. S. G. Warren, “Optical constants of ice from the ultraviolet to the microwave,” Appl. Opt., **23**, 1206-1225 (1984).

69. J. Iaquinta, H. Isaka, and P. Personne, “Scattering phase function of bullet rosette ice crystals,” J. Atmos. Sci., **52**, 1401–1413 (1995).

70. P. Yang, B.-C. Gao, B. A. Baum, Y. X. Hu, W. J. Wiscombe, M. I. Mishchenko, D. M. Winker, and S. L. Nasiri, “Asymptotic solutions for optical properties of large particles with strong absorption,” Appl. Opt., **4**0, 1532-1547 (2001).

71. P. Chylek and J. D. Klett, “Extinction cross sections of nonspherical particles in the anomalous diffraction approximation,” J. Opt. Soc. Am. A., **8,** 274-281 (1991).

72. P. Chylek and J. D. Klett, “Absorption and scattering of electromagnetic radiation by prismatic columns: anomalous diffraction approximation,” J. Opt. Soc. Am. A, **8,** 1713-1720 (1991).

73. S. A. Ackerman and G. L. Stephens, “The absorption of solar radiation by cloud droplets: An application of anomalous diffraction theory,” J. Atmos. Sci., **44**, 1574–1588 (1987).

74. G. R. Fournier and B.T. E. Evans, “Approximation to extinction efficiency for randomly oriented spheroids,” Appl. Opt., **30**, 2041-2048 (1991).

75. D. A. Cross and P. Latimer, “General solutions for the extinction and absorption efficiencies of arbitrarily oriented cylinders by anomalous-diffraction methods, J. Opt. Soc. Am. A., **60**, 904-907 (1970).

76. G. L. Stephens, “Scattering of plane waves by soft obstacles: Anomalous diffraction theory for circular cylinder,” Appl. Opt., **23**, 954-959 (1984)

77. Y. Liu, W. P. Arnott and J. Hallet, “Anomalous diffraction theory for arbitrarily orientated finite circular cylinders and comparison with exact T-matrix result,” Appl. Opt. **37**, 5019-5030 (1998)

78. D. H. Napper, “A Diffraction theory approach to the total scattering by cubes,” Kolloid-Z. u. Z. Polymere, **195**, 41-46 (1966).

79. A. Maslowska, P. J. Flatau and G. L. Stephens, “On the validity of the anomalous diffraction theory to light scattering by cubes,” Opt. Commun., **107**, 35-40 (1994).

80. W. B. Sun and Q. Fu, “Anomalous diffraction theory for arbitrarily oriented hexagonal crystals,” J. Quant. Spectros. Rad. Transfer, **63**, 727–737 (1999)

81. W. B. Sun and Q. Fu, “Anomalous diffraction theory for randomly oriented nonspherical particles: a comparison between original and simplified solutions,” J. Quant. Spectros. Rad. Transfer, **70**, 737-747 (2001).

82. D. S. Jones, “Approximate methods in high-frequency scattering,” Proc. R. Soc. London Ser. A, **239**,338-348 (1957)

83. D. S. Jones, “High-frequency scattering of electromagnetic waves,” Proc. R. Soc. London Ser. A, **240**, 206-213 (1957)

84. H. M. Nussenzveig and W. J. Wiscombe, “Efficiency factors in Mie scattering.” Phys. Review Lett., **45**, 1490-1494 (1980)

85. M. Xu, M. Lax M and R. R. Alfano, “Light anomalous diffraction using geometrical path statistics of rays and Gaussian ray approximation,” Opt. Lett., **28**, 179-181 (2003)

86. M. Xu, “Light Extinction and Absorption by Arbitrarily Oriented Finite Circular Cylinders by Use of Geometrical Path Statistics of Rays,” Appl. Opt., **42**, 6710-6723 (2003).

87. R. M.Goody and Y. L. Yung, *Atmospheric radiation. Theoretical basis. 2nd ed* (Oxford University Press, New York, 1989).

88. K. N. Liou, *An introduction to atmospheric radiation. 2nd ed.* (Academic Press, San Diego, 2002)

89. M. D. Chou and L. Kouvaris, “Monochromatic calculations of atmospheric radiative transfer due to molecular line absorption,” J. Geophys. Res., **91**, 4047-4055 (1986).

90. A. A. Lacis and V. Oinas “A description of the correlated k distributed method for modeling nongray gaseous absorption, thermal emission, and multiple scattering in vertically inhomogeneous atmospheres,” J. Geophys. Res., **96**, 9027-9063 (1991).

91. Q. Fu and K. N. Liou, “On the correlated k-distribution method for radiative transfer in nonhomogeneous atmospheres,” J. Atmos. Sci., **49**, 2139-2156 (1992).

92. D. P. Kratz and R. D. Cess, “Infrared radiation models for atmospheric ozone,” J. Geophys. Res., **93**, 7047-7054 (1988).

93. A. J. Heymsfield and R. G. Knollenberg, “Properties of cirrus generating cells,” J. Atmos. Sci., **29,** 1358–1366 (1972).

94. V. Vouk, “Projected area of convex bodies,” Nature, **162**, 330-331 (1948).

95. F. D. Bryant and P. Latimer, “Optical efficiencies of large particles of arbitrary shape and orientation,” J. Colloid Interface Sci., **30**, 291-304 (1969)

96. M. I. Mishchenko, L. D. Travis and A. A. Lacis, *Scattering , absorption and emission of light by small particles* (Cambridge University Press, Cambridge, 2002.)

97. R. Lhermitte, “A 94-GHz Doppler radar for cloud observations,” J. Atmos. Oceanic Technol., **4**, 36–48 (1987).

98. E. E. Clothiaux, M. A. Miller, B. A. Albrecht, T. P. Ackerman, J. Verlinde, D. M. Babb, R. M. Peters and W. J. Syrett, “An evaluation of a 94-GHz radar for remote sensing of cloud properties, J. Atmos. Oceanic Technol., **12**, 201–229 (1995)

99. S. D. Miller and G. L. Stephens, “CloudSat instrument requirements as determined from ECMWF forecasts of global cloudiness,” J. Geophys. Res., **106**, 713-733 (2001)

100. K. F. Evans and J. Vivekanandan, “Multiparameter radar and microwave radiativetransfer modeling of nonspherical atmospheric ice particles,” IEEE Trans. Geosci. Remote Sensing, **28**, 423–437 (1990).

101. T. L. Schneider and G. L. Stephens, Theoretical aspects of modeling backscattering by circus cloud

particles at millimeter radar wavelength," J. Atmos. Sci., **52**, 4367-4385 (1995).

102. L. J. Battan, *Radar observation of the atmosphere* (University of Chicago Press, Chicago, 1973)

103. A. Taflove, *Computational Electrodynamics: The finite-difference time-domain method*, (Artech House, Boston, 1995)

104. K. S. Kunz and R. J. Luebbers, *The finite difference time domain method for electromagnetics* (CRC Press, Boca Raton, FL, 1993)

105. A. Taflove, *Advances in computational electrodynamics: The finite-difference time-domain method* (Artech House, Boston, 1998)

106. A. J. Heymsfield and L. J. Miloshevich, "Parameterizations for the cross-sectional area and extinction of cirrus and stratiform ice cloud particles," J. Atmos. Sci., **60**, 936–956 (2003)

107. D. R. Dowling, and L. F. Radke, "A summary of physical properties of cirrus clouds," J. Appl. Meteor*.,* **29,** 970–978 (1990).

108. A. J. Heymsfield, K. M. Miller, and J. D. Spinhirne, "The 27–28 October 1986 FIRE IFO cirrus case study: Cloud microstructure," Mon. Wea. Rev.*,* **118,** 2313–2328 (1990).

109. A. L. Kosarev and I. P. Mazin, "An empirical model of the physical structure of upper layer clouds," Atmos. Res*.,* **26,** 213–228 (1991).

110. L. Liao and K. Sassen, "Investigation of relationships between K_a-band radar reflectivity and liquid water content," Atmos. Res., **34,** 231-248 (1993)

111. D. Atlas, S. Y. Matrosov, A. J. Heymsfield, M. D. Chou and D. B. Wolff, "Radar and radiation properties of ice clouds," J. Appl. Meteor., **34,** 2329–2345 (1995).

VITA

Zhibo Zhang was born in Jilin, Jilin province, China, on January 15, 1979. He enrolled at Nanjing University with a major in atmospheric science and received a Bachelor of Science degree in July of 2001. He enrolled as a graduate student in the Texas A&M University Department of Atmospheric Sciences in September of 2002. His permanent address is Department of Atmospheric Sciences, Texas A&M University, 3150 TAMU, College Station, TX 77840.